OECD/MCCI-2005-TR05

OECD MCCI Project
2-D Core Concrete Interaction (CCI) Tests:
Final Report

February 28, 2006

by:

M. T. Farmer, S. Lomperski, D. J. Kilsdonk, and R. W. Aeschlimann
Nuclear Engineering Division
Argonne National Laboratory
9700 S. Cass Avenue
Argonne, IL 60439 USA

S. Basu
Project Manager
U.S. Nuclear Regulatory Commission

Table of Contents

Page

0.0 EXECUTIVE SUMMARY viii
1.0 INTRODUCTION 1
1.1 Background 1
1.2 Objectives 2
1.3 Approach 2
2.0 FACILITY DESCRIPTION 4
2.1 Test Apparatus 4
2.2 Water Supply System 9
2.3 Quench System 11
2.4 Test Section Pressure Relief System 12
2.5 Off Gas System 13
2.6 Cover Gas System 13
2.7 Power Supply 14
2.8 Concrete Compositions 14
2.9 Corium Compositions 15
2.10 Instrumentation and Data Acquisition 17
2.11 Test Procedures 22
Pretest Operations 22
Test Operations 25
Posttest Operations 25
3.0 RESULTS AND DISCUSSION 27
3.1 CCI-1 Test Results 27
Thermalhydraulic Results 27
Posttest Examination Results 33
3.2 CCI-2 Test Results 42
Thermalhydraulic Results 42
Posttest Examination Results 48
3.3 CCI-3 Test Results 56
Thermalhydraulic Results 56
Posttest Examination Results 62
3.4 Discussion 69
4.0 APPLICATION OF RESULTS TO PLANT SCALE 79
5.0 SUMMARY AND CONCLUSIONS 81
6.0 REFERENCES 85

List of Figures

Figure		Page
2-1	Key Elements of the CCI Test Apparatus	5
2-2	Overview of the Facility	5
2-3	Details of the Test Section	6
2-4	Top View of Lower Test Section	6
2-5	Side View of Lower Section Showing Inert MgO Sidewalls	7
2-6	Side View of Lower Section Showing Concrete Sidewalls	7
2-7	Sidewall Components after Fabrication	8
2-8	Thermite Powder Loading Scheme	8
2-9	Lower Section Prior to Placement of MgO Sidewalls	8
2-10	Details of the Top Test Section	9
2-11	Crust Lance Assembly	9
2-12	Test Section Mounted on the Platform	10
2-13	Test Section Water Supply System	10
2-14	Quench and Overflow Tanks	11
2-15	Spray Tank	11
2-16	Test Section Pressure Relief System	12
2-17	Off Gas System	13
2-18	Cover Gas System	13
2-19	DAS Setup for the CCI Tests	17
2-20	Plan View of Basemat Instrumentation	19
2-21	Elevation View of Basemat Type C Thermocouple Locations	19
2-22	Thermocouples Installed in the Basemat Form	20
2-23	Thermocouples Installed in the Sidewall Form	20
2-24	Test Section (a) Sidewall Thermocouple and (b) Pressure Transducer Locations	21
2-25	Electrode Current Monitoring System Layout	22
2-26	Thermite Sample Train	24

List of Figures (Contd.)

Figure **Page**

3-1 CCI-1 DEH Input Power 28
3-2 CCI-1 Basemat Heatup Near Centerline 29
3-3 CCI-1 North Wall Heatup (+10 cm) 29
3-4 CCI-1 South Wall Heatup (+10 cm) 29
3-5 CCI-1 Melt Temperatures Near Centerline 30
3-6 CCI-1 Melt Temperatures Near the North Wall (+5 cm Elevation) 30
3-7 CCI-1 Melt Temperatures Near the South Wall (+5 cm Elevation) 30
3-8 Collection of CCI-1 Melt Temperatures 31
3-9 CCI-1 Axial Ablation 31
3-10 CCI-1 North Sidewall Ablation 31
3-11 CCI-1 South Sidewall Ablation 32
3-12 CCI-1 Peak Axial and Lateral Ablation Data 32
3-13 CCI-1 Melt-Water Heat Flux 32
3-14 CCI-1 Debris Upper Surface: (a) As Found Condition, and (b) After Removal of Loose Debris 33
3-15 CCI-1 Samples of Erupted Material 34
3-16 CCI-1 Crust Lance Hole Through Crust 35
3-17 CCI-1 Core Samples From: (a) North Wall, Laterally (+10 cm Elevation) and (b) Basemat, Axially. Core-Concrete Interface is to the Right 35
3-18 View After Removal of West MgO Sidewall 36
3-19 CCI-1 Debris Over Basemat: (a) View From North (b) View From South 36
3-20 CCI-1 Debris Over Basemat: (a) View From East (b) View From West 37
3-21 CCI-1 Concrete Walls: (a) North, and (b) South 37
3-22 CCI-1 Close-Up of North Wall 38
3-23 Rendering of CCI-1 Posttest Debris Distribution 38
3-24 CCI-2 DEH Input Power 42
3-25 CCI-2 Basemat Heatup Near Centerline 44
3-26 CCI-2 North Wall Heatup (+10 cm) 44
3-27 CCI-2 South Wall Heatup (+10 cm) 44

List of Figures (Contd.)

Figure **Page**

3-28 CCI-2 Melt Temperatures Near Centerline 45
3-29 CCI-2 Melt Temperatures Near the North Wall (+5 cm Elevation)....45
3-30 CCI-2 Melt Temperatures Near the South Wall (+5 cm Elevation)....45
3-31 Collection of CCI-2 Melt Temperatures....46
3-32 CCI-2 Axial Ablation 46
3-33 CCI-2 North Sidewall Ablation....46
3-34 CCI-2 South Sidewall Ablation....47
3-35 CCI-2 Peak Axial and Lateral Ablation Data....47
3-36 CCI-2 Melt-Water Heat Flux....47
3-37 (a) Top View of Bridge CCI-2 Crust, and (b) Schematic Detailing Key Features and Elevations....48
3-38 CCI-2 Crust Mantle Adhering to East Sidewall (after removal of bridge crust)....49
3-39 Rendering of CCI-2 Posttest Debris (Non-Electrode Sidewall View) 49
3-40 CCI-2 View After Removal of West MgO Sidewall....50
3-41 CCI-2 Solidified Corium; Views from (a) Southeast, and (b) Northwest....50
3-42 Photograph of Core Sample Opening Through CCI-2 Crust 51
3-43 CCI-2 Axial Core Sample....51
3-44 CCI-2 Debris Over Basemat: (a) View From North (b) View From South 52
3-45 CCI-2 Solidified Corium and Concrete Sidewalls; Views from (a) Southeast, and Northwest....52
3-46 Rendering of CCI-2 Posttest Debris Configuration....53
3-47 CCI-3 DEH Input Power 56
3-48 CCI-3 Basemat Heatup Near Centerline 58
3-49 CCI-3 North Wall Heatup (+10 cm)....58
3-50 CCI-3 South Wall Heatup (+10 cm)....58
3-51 CCI-3 Melt Temperatures Near Centerline 59
3-52 CCI-3 Melt Temperatures Near the North Wall (+5 cm Elevation)....59
3-53 CCI-3 Melt Temperatures Near the South Wall (+5 cm Elevation)....59
3-54 Collection of CCI-3 Melt Temperatures....60

List of Figures (Contd.)

Figure **Page**

3-55 CCI-3 Axial Ablation 60
3-56 CCI-3 North Sidewall Ablation 60
3-57 CCI-3 South Sidewall Ablation 61
3-58 CCI-3 Axial and Lateral Ablation Data 61
3-59 CCI-3 Melt-Water Heat Flux 61
3-60 CCI-3 Debris Upper Surface in the As-Found Condition 62
3-61 Photograph of Hole Formed by Lance Through the CCI-3 Bridge Crust 63
3-62 CCI-3 Photograph of Void Pocket Over Solidified Melt in South Wall 64
3-63 Rendering of CCI-3 Posttest Debris Configuration 64
3-64 Photograph of Core Sample Opening Through CCI-3 Crust 65
3-65 CCI-3 Axial Core Sample 65
3-66 CCI-3 View After Removal of West MgO Wall 65
3-67 CCI-3 Debris Over Basemat: (a) View From North (b) View From South 66
3-68 CCI-3 Debris Over Basemat: (a) View From East (b) View From West 66
3-69 CCI-3 Concrete Walls: (a) North, and (b) South 67
3-70 Average Melt Temperatures for CCI Tests 70
3-71 Lateral Ablation for CCI Tests 70
3-72 Axial Ablation for CCI Tests 70
3-73 Debris/Water Heat Flux for CCI Tests 71
3-74 Axial Debris Morphology for Test: (a) CCI-1, (b) CCI-2, and (c) CCI-3 74

List of Tables

Table **Page**

1-1 Specifications for CCI Tests 3

2-1 Chemical Composition of Concretes 14

2-2 Concrete Densities 15

2-3 Initial Melt Compositions for CCI Tests 15

2-4 Detailed Pre- and Post-Reaction Thermite Compositions for CCI Tests 16

2-5 Summary of CCI Test Instrumentation 18

3-1 CCI-1 Event Sequence 28

3-2 Masses of Material Regions Measured During Disassembly for CCI-1 34

3-3 Summary of CCI-1 Sample Locations 39

3-4 CCI-1 Analysis Results for Samples Taken Across Radial Extent of Debris at + 10 cm Elevation 40

3-5 CCI-1 Analysis Results for Samples Taken At Two Axial Elevations Near the Test Section Centerline 41

3-6 CCI-1 Analysis Results for Samples Taken at Other Debris Locations 41

3-7 CCI-2 Event Sequence 43

3-8 Masses of Material Regions Measured During Disassembly for CCI-2 50

3-9 Summary of CCI-2 Sample Locations 54

3-10 CCI-2 Analysis Results for Samples Taken Across Lateral Extent of the Debris Near the Debris Axial Centerline 54

3-11 CCI-2 Analysis Results for Samples Taken At Three Axial Elevations Near the Test Section Centerline 55

3-12 CCI-2 Analysis Results for Samples Taken at Other Debris Locations 55

3-13 CCI-3 Event Sequence 57

3-14 Masses of Material Regions Measured During Disassembly for CCI-3 63

3-15 Summary of CCI-3 Sample Locations 68

3-16 CCI-3 Analysis Results for Samples Taken Across Lateral Extent of the Debris Near the Debris Axial Centerline 68

3-17 CCI-3 Analysis Results for Samples Taken At Three Axial Elevations Near the Test Section Centerline 69

3-18 Properties of Concretes Used in CCI Test Series 71

3-19 Lateral/Axial Ablation Rate and Power Split Estimates for CCI Tests 72

List of Tables

Table **Page**

3-20 Debris-Water Heat Fluxes for CCI Tests Averaged Over the Time Interval 15-25 Minutes after Cavity Flooding 76

3-21 Results of *In-Situ* Crust Strength Measurements for CCI Tests 78

0.0 EXECUTIVE SUMMARY

The purpose of the OECD/MCCI Program was to carry out reactor materials experiments and associated analysis to achieve the following two technical objectives: 1) resolve the ex-vessel debris coolability issue by providing both confirmatory evidence and test data for coolability mechanisms identified in previous integral effect tests, and 2) address remaining uncertainties related to long-term 2-D core-concrete interaction under both wet and dry cavity conditions. This report has summarized the results of three large scale Core-Concrete Interaction (CCI) experiments that were conducted to address the second program objective. The overall purpose of these tests was to provide information in several areas, including: i) lateral vs. axial power split during dry core-concrete interaction, ii) integral debris coolability data following late phase flooding, and iii) data regarding the nature and extent of the cooling transient following breach of the crust formed at the melt-water interface.

The experimental approach was to investigate the interaction of fully oxidized PWR core melts with specially-designed two-dimensional concrete test sections. The initial phase of the tests was conducted under dry cavity conditions. After a predetermined time interval and/or ablation depth was reached, the cavities were flooded with water to obtain data on the coolability of core melts after core-concrete interaction had progressed for some time. Two tests were conducted with siliceous concrete (CCI-1 and CCI-3), and a third test with Limestone/Common Sand (LCS) concrete (CCI-2). Test CCI-1 was conducted with a U.S.-specific siliceous concrete that had very low gas content, while CCI-3 was conducted with a European-specific siliceous concrete with gas content intermediate to that used in CCI-1 and CCI-2. The input power for the tests was selected so that the initial heat flux to the concrete surfaces and overlying structure was in the range of that expected during the early stages of an ex-vessel plant accident; i.e., 150-200 kW/m^2. On this basis, total input power for the CCI-1 was selected to yield a heat flux at the upper end of this range (viz., 150 kW), while the other two tests were conducted with an input power that yielded a flux at the lower end of the range (viz., 120 kW).

During dry cavity operations, all tests showed the overall trend of decreasing melt temperature as ablation progressed, which was due to a heat sink effect as relatively cool concrete slag was introduced into the melt, as well as the increasing heat transfer surface area as the melts expanded into the concrete crucibles. The reduction in melt temperature may have further reflected the evolution of the pool boundary freezing temperature that decreased as additional concrete was eroded into the melt over the course of the tests.

Tests CCI-1 and CCI-2 showed evidence of initial crust formation on the concrete basemat and sidewalls that resulted in an incubation period in which the ablation rates were very low and the melt temperature was relatively stable. Test CCI-3 also showed evidence of initial crust formation on the concrete basemat, but there was no evidence of initial sidewall crust formation for this test. In all cases, the surface crusts eventually failed, thereby allowing ablation to proceed. The duration of the incubation period for CCI-1 and CCI-2 appeared to be inversely proportional to concrete gas content, which suggests that crust failure may be driven in part by the mechanical forces that arise from the production of concrete decomposition gases at the core-concrete interface.

Long-term ablation behavior was found to be closely linked to concrete type. Lateral and axial ablation rates for the LCS concrete test were virtually indistinguishable; the concrete erosion rate averaged 4 cm/hr over several hours of interaction before gradually decreasing. The

corresponding surface heat flux was ~ 60 kW/m^2. Thus, the lateral/axial heat flux ratio for this concrete type was ~ 1.

The relatively uniform power split for CCI-2 can be contrasted with the results of the two tests conducted with siliceous concrete. For test CCI-1, the ablation was highly non-uniform, with most of the ablation concentrated in the North sidewall of the test apparatus. Crust stability may have played a major role in determining the ablation progression for this experiment; i.e., the data suggests that after the crust failed on the North concrete sidewall, the input power was predominately dissipated through ablation of this sidewall, while crusts continued to protect the basemat and south sidewall surfaces during the balance of the interaction.

In contrast to Test CCI-1, Test CCI-3 exhibited fairly symmetrical behavior insofar as the progression of lateral ablation is concerned. However, unlike Test CCI-2, the lateral ablation was highly pronounced in comparison to axial ablation. In this regard, the results of tests CCI-1 and CCI-3 are consistent. Lateral ablation in CCI-3 averaged 10 cm/hr over the last hour of the experiment, while the axial ablation rate was limited to 2.5 cm/hr over the same time interval. The corresponding heat fluxes in the lateral and axial directions were 97 and 25 kW/m^2, respectively. On this basis, the lateral/axial surface heat flux ratio for CCI-3 was estimated as ~ 4, which is significantly higher than the near-unity ratio deduced for test CCI-2 with LCS concrete. Between the two concrete types, possible explanations for differences in the erosion behavior are chemical composition and concrete gas content. A third possible explanation was revealed during posttest examinations. In particular, the core-concrete interface for the siliceous concrete tests consisted of a region where the core oxide had locally displaced the cement that bonded the aggregate. Conversely, the ablation front for the LCS test consisted of a powdery interface in which the core and concrete oxides were clearly separated. Variations in the interface characteristics may have influenced the ablation behavior for the two concrete types.

In terms of the chemical analysis results obtained as part of the test series, the corium in the central region of the test section was found to have a higher concentration of core oxides in comparison to that adjacent to the two ablating concrete sidewalls for all tests. Conversely, core oxides were found to be slightly concentrated near the concrete basemat in comparison to that found in the bulk of the corium. For both siliceous concrete tests, two zones appeared to be present: a heavy monolithic oxide phase immediately over the basemat that was enriched in core oxides, with a second overlying porous, light oxide phase that was enriched in concrete oxides. The overlying oxide phase was porous and appeared to have been quenched after the cavity was flooded. This well-defined phase distribution can be contrasted with the debris morphology for CCI-2. In this test, the debris was highly porous and fragmented over the entire axial extent of the material remaining over the basemat. This open structure is consistent with the high degree of debris cooling that occurred during this test after cavity flooding.

A second and equally important aspect of the test series was to investigate debris coolability under late-phase flooding conditions. In terms of phenomenology, the tests provided data on the bulk cooling, water ingression, melt eruption, and transient crust breach cooling mechanisms. In addition, Test CCI-2 provided data on water ingress at the interface between the core material and concrete sidewalls. This mechanism had been previously identified in the COTELS reactor material test series.

The heat flux during the first 5 minutes of cavity flooding was high for all tests. For the two tests conducted with siliceous concrete, the initial heat fluxes were close to the Critical Heat Flux (CHF) limitation of ~ 1 MW/m^2 under saturated boiling conditions. Thus, the heat fluxes were indicative of quenching of the upper surface crust that was present as an initial condition

for both tests. However, for test CCI-2, the upper surface was essentially devoid of a surface crust at the time of cavity flooding. Thus, water was able to directly contact the melt, resulting in a bulk cooling transient in which the initial cooling rate approached 3 MW/m^2. The heat flux eventually fell below 1 MW/m^2 after ~ 5 minutes. At this time, a stable crust most likely formed at the melt-water interface, thereby terminating the bulk cooling transient.

The tests did not generally exhibit a pronounced decrease in overall melt temperature after cavity flooding. This is despite the fact that the heat flux and power supply responses both indicated substantial debris cooling. This type of behavior can be rationalized by a latent heat transfer process in which a quench front develops at the melt/water interface, as opposed to a sensible heat transfer process in which the entire melt mass is cooled by convective heat transfer with the heat dissipated to the overlying water by conduction across a thin crust at the melt/water interface. The posttest debris morphologies were also consistent with development of quenched debris zones, as opposed to bulk cooldown of the entire melt mass by conduction-limited cooling across a thin crust at the interface.

After the initial transient, the debris/water heat fluxes ranged from 250 to 650 kW/m^2. Heat fluxes for both siliceous concrete tests were lower than the test conducted with LCS concrete. In general, the data seemed to indicate that the heat flux increases with concrete gas content. The heat fluxes realized in the tests were up to an order of magnitude higher than that predicted by the SSWICS water ingression correlation. Thus, the data suggests that the degree of interconnected cracks/fissures/porosity that form the pathway for water to ingress into solidifying core material is increased by the presence of gas sparging, particularly for the case in which the melt contains a high concrete fraction.

Aside from the water ingression mechanism, the tests also provided data on the melt eruption cooling mechanism. Significant eruptions were observed for Test CCI-2. However, no spontaneous eruptions were observed after cavity flooding for the two tests conducted with siliceous concrete. The reduced gas content for this concrete type may have contributed to the lack of eruptions for these two tests. Test occurrences may have also played a role in the lack of eruptions (i.e., input power for Test CCI-1 was terminated 10 minutes after cavity flooding, and for Test CCI-3, a partially anchored bridge crust formed during the test sequence that could have adversely affected the eruption process). The melt entrainment coefficient for CCI-2 was ~ 0.11 %, which is in the range of that required to stabilize a core-concrete interaction over a fairly significant range of melt depths.

In terms of the crust breach cooling mechanism, both siliceous concrete tests provided data on *in-situ* crust strength, while Test CCI-1 also provided data on the extent of cooling after crust breach. The crust strength data indicates that crust material formed during quench is very weak. This finding is consistent with the SSWICS test series crust strength measurements. However, the CCI strength measurements are significant because they were carried out under prototypic temperature boundary conditions before the material had cooled to room temperature.

Aside from the crust strength measurements, the crust breach event in CCI-3 caused a significant transient increase in the debris cooling rate. In particular, a large melt eruption occurred, resulting in a transient cooling event in which the peak heat flux exceeded 3 MW/m^2. After the breach, the heat flux from the debris upper surface steadily declined over the next five minutes to a plateau in the range of 250-300 kW/m^2, which is similar to the plateau observed prior to the breach event. In general, the data obtained from this procedure indicates that breach events may lead to significant transient increases in the debris cooling at plant scale.

In terms of the applicability to plant conditions, these tests have provided information that will contribute to the database for reducing modeling uncertainties related to two-dimensional molten core-concrete interaction under both wet and dry cavity conditions. Furthermore, the tests have provided additional confirmatory evidence and test data for coolability mechanisms identified in earlier integral effect tests. Data from this and other test series thus forms the technical basis for developing and validating models of the various cavity erosion and debris cooling mechanisms. These models can then be deployed in integral codes that are able to link the interrelated phenomenological effects, thereby forming the technical basis for extrapolating the results to plant conditions.

Note that the tests carried out as part of this particular program have examined core-concrete interaction and debris coolability for the case of fully oxidized core melts. As a whole, the results of the two-dimensional CCI tests have indicated trends in the ablation front progression that cannot be explained on the basis of our current understanding of the phenomenology involved with this type of physical process. These trends need to be understood before the results can be extrapolated to plant scale. Furthermore, in real plant accident sequences, a significant melt metal fraction could be present that may result in a stratified pool configuration. This type of pool structure was not evaluated in the program. Thus, additional analysis and testing may be required with melts containing a significant metal fraction to further reduce phenomenological uncertainties related to core-concrete interaction, and to evaluate the effects of melt metal content on debris coolability.

.

1.0 INTRODUCTION

1.1 Background

Although extensive research has been conducted over the last several years in the areas of Core-Concrete Interaction (CCI) and debris coolability, two important issues warrant further investigation. The first issue concerns the effectiveness of water in terminating a CCI by flooding the interacting masses from above, thereby quenching the molten core debris and rendering it permanently coolable. This safety issue was investigated in the EPRI-sponsored Melt Attack and Coolability Experiments (MACE) program.[1,2] The approach was to conduct large scale, integral-type reactor materials experiments with core melt masses ranging up to two metric tons. These experiments provided unique, and for the most part repeatable, indications of heat transfer mechanism(s) that could provide long term debris cooling.[2] However, the results did not demonstrate definitively that a melt would always be completely quenched. This was due to the fact that the crust anchored to the test section sidewalls in every test, which led to melt/crust separation, even at the largest test section lateral span of 1.20 m. This decoupling is not expected for a typical reactor cavity, which has a span of 5-6 m. Even though the crust may mechanically bond to the reactor cavity walls, the weight of the coolant and the crust itself is expected to periodically fracture the crust and restore contact with the melt. Although crust fracturing does not ensure that coolability will be achieved, it nonetheless provides a pathway for water to recontact the underlying melt, thereby allowing other debris cooling mechanisms (e.g., water ingression[3] and melt eruptions[4]; see Farmer *et al.*[2]) to proceed. A related task of the current program, which is not addressed in this particular report, is to measure crust strength to check the hypothesis that a corium crust would not be strong enough to sustain melt/crust separation in a plant accident.[5]

The second important issue concerns long-term, two-dimensional concrete ablation by a prototypic core oxide melt. As discussed by Foit,[6] the existing reactor material database for dry cavity conditions is solely one-dimensional (e.g., see Copus *et al.*,[7] Thompson *et al.*,[8-9] and Fink *et al.*[10]). Although the MACE Scoping Test was carried out with a two-dimensional concrete cavity, the interaction was flooded soon after ablation was initiated to investigate debris coolability.[1] Moreover, due to the scoping nature of this test, the apparatus was minimally instrumented and therefore the results are of limited value from the code validation viewpoint. Aside from the MACE program, the COTELS test series also investigated 2-D CCI under flooded cavity conditions. However, the input power density for these tests was quite high relative to the prototypic case (Nagasaka *et al.*[11]). Finally, the BETA test series provided valuable data on 2-D core concrete interaction under dry cavity conditions, but these tests focused on investigating the interaction of the metallic (steel) phase with concrete (Alsmeyer[12]). Due to these limitations, there is significant uncertainty in the partition of energy dissipated for the ablation of concrete in the lateral and axial directions under dry cavity conditions for the case of a core oxide melt (Foit[6]). Accurate knowledge of this "power split" is important in the evaluation of the consequences of an ex-vessel severe accident; e.g., lateral erosion can undermine containment structures, while axial erosion can penetrate the basemat, leading to ground contamination and/or possible containment bypass. As a result of this uncertainty, there are still substantial differences among computer codes in the prediction of 2-D cavity erosion behavior under both wet and dry cavity conditions (Foit[6]).

1.2 Objectives

In light of the above issues, the OECD-sponsored Melt Coolability and Concrete Interaction (MCCI) program was initiated at Argonne National Laboratory. The project conducted reactor materials experiments and associated analysis to achieve the following technical objectives:

1. resolve the ex-vessel debris coolability issue through a program that focused on providing both confirmatory evidence and test data for the coolability mechanisms identified in MACE integral effects tests, and

2. address remaining uncertainties related to long-term 2-D core-concrete interactions under both wet and dry cavity conditions.

Data from the various tests conducted as part of the program are being used to develop and validate models and codes that are used to extrapolate the experimental findings to plant conditions. Achievement of these technical objectives will demonstrate the efficacy of severe accident management guidelines for existing plants, and provide the technical basis for better containment designs of future plants.

The project completed three large scale CCI experiments to address the second technical objective defined above. Specifications for the three tests are provided in Table 1-1. The overall purpose of the test series was to provide information in several areas, including: i) lateral vs. axial power split during dry core-concrete interaction, ii) integral debris coolability data following late phase flooding, and iii) data regarding the nature and extent of the cooling transient following breach of the crust formed at the melt-water interface.

1.3 Approach

The experimental approach for the CCI test series was to investigate the interaction of Pressurized Water Reactor (PWR) core melts with specially-designed 2-D concrete test sections. The initial phase of the tests was conducted under dry cavity conditions. After a predetermined time interval and/or ablation depth was reached, the cavities were flooded with water to obtain data on the coolability of core melts after core-concrete interaction had progressed for some time. The initial melt compositions were predominately oxidic. A significant metal phase was not involved, but may be present during an accident. Based on the initial melt density of ~6500 kg/m^3, the steel may be layered below the oxide phase. Thus, data from this test series may not be directly applicable to reactor accident sequences, but the results are nonetheless useful for code validation purposes. The input power levels of 120-150 kW used in the tests were selected so that the heat fluxes from the melt to concrete surfaces and the upper atmosphere were initially in the range of that expected early in the accident sequence (i.e., 150-200 kW/m^2).

This final report provides a summary of the results from all three tests. The report begins by providing an overview description of the facility, followed by a summary of the thermal-hydraulic and posttest examination results for each individual test. The report then concludes with a discussion focused on comparing and contrasting the results from all three tests. Additional information regarding the apparatus,[13] procedures, and results are provided in detailed data reports that were prepared for each test,[14-16] as well as various conference proceedings.[17-20]

Table 1-1. Specifications for CCI Tests.

Parameter	Specification for Test:		
	CCI-1	**CCI-2**	**CCI-3**
Corium	PWR + 8 wt% SIL	PWR + 8 wt% LCS	PWR + 15 wt% SIL
Concrete type[a]	SIL (U.S.-type)	LCS	SIL (EU-type)
Basemat cross-section	50 cm x 50 cm	50 cm x 50 cm	50 cm x 50 cm
Initial melt mass (depth)	400 kg (25 cm)	400 kg (25 cm)	375 kg (25 cm)
Test section sidewall construction	Nonelectrode walls: concrete Electrode walls: Inert	Nonelectrode walls: concrete Electrode walls: Inert	Nonelectrode walls: concrete Electrode walls: Inert
Lateral/Axial ablation limit	35/35 cm	35/35 cm	35/35 cm
System pressure	Atmospheric	Atmospheric	Atmospheric
Melt formation tech.	Chemical reaction (~30 s)	Chemical reaction (~30 s)	Chemical reaction (~30 s)
Initial melt temperature	1950 ºC	1880 ºC	1950 ºC
Melt heating technique	DEH	DEH	DEH
Power supply operation prior to water addition	Constant @ 150 kW	Constant @ 120 kW	Constant @ 120 kW
Criteria for water addition	1) 5.5 hours of operation with DEH input, or 2) lateral/axial ablation reaches 30 cm	1) 5.5 hours of operation with DEH input, or 2) lateral/axial ablation reaches 30 cm	1) 5.5 hours of operation with DEH input, or 2) lateral/axial ablation reaches 30 cm
Inlet water flowrate/temp.	2 lps/20 ºC	2 lps/20 ºC	2 lps/20 ºC
Water depth over melt	50 ± 5 cm	50 ± 5 cm	50 ± 5 cm
Power supply operation after water addition	Constant voltage	Constant voltage	Constant voltage
Test termination criteria	1) Melt temperature falls below concrete solidus, 2) ablation is arrested, or 3) 35 cm ablation limit is reached.	1) Melt temperature falls below concrete solidus, 2) ablation is arrested, or 3) 35 cm ablation limit is reached.	1) Melt temperature falls below concrete solidus, 2) ablation is arrested, or 3) 35 cm ablation limit is reached.
Operational Summary	Successful: non-symmetrical ablation behavior	Successful: symmetrical ablation behavior	Successful: symmetrical ablation behavior

[a]SIL denotes siliceous concrete, LCS denotes Limestone/Common Sand concrete.

2.0 FACILITY DESCRIPTION

With the exception of a few minor instrumentation upgrades that were made as the experiment series progressed, the CCI facility was essentially identical for all three tests. Thus, a generic description of the facility is provided below, with the minor differences in instrumentation described within the subsection that is devoted to that particular topic.

Principal elements of the facility consisted of the test apparatus, a power supply for Direct Electrical Heating (DEH) of the corium, a water supply system, two steam condensation (quench) tanks, an off gas system to filter and vent the off-gases, and a Data Acquisition System (DAS). A schematic illustration of the facility is provided in Figure 2-1, while an overview photograph showing key elements of the facility is provided in Figure 2-2. The specifications for the individual tests conducted as part of the CCI test series were previously summarized in Table 1-1. With the exception of the DAS, the entire system was housed in an explosion-rated containment cell. All operational features of the tests, including DEH input power, water supply, and gas flows, were remotely controlled from the experimenter's console located outside the containment. The various elements of the facility are described in sequence below.

2.1 Test Apparatus

The apparatus for containment of the core melt consisted of a test section that was 3.4 m tall with a square internal cross-section which initially measured 50 cm x 50 cm. The principal components of the apparatus, shown in Figure 2-3, consisted of a bottom support plate, three sidewall sections, and an upper enclosure lid. The lower sidewall section contained the corium melt and structural concrete components that were intended to undergo ablation. A top view of the lower section is shown in Figure 2-4, while cross-sectional views of the electrode and non-electrode sidewalls are provided in Figures 2-5 and 2-6, respectively. The concrete basemat was initially 55 cm deep, so that up to 35 cm of axial ablation could safely be accommodated prior to terminating the experiment.

As shown in Figure 2-4, the electrode sidewalls of the lower section were fabricated from a castable MgO refractory, while the non-electrode sidewalls were fabricated from the particular concrete composition specified for each test (see Table 1-1). A photograph showing typical components after fabrication is provided in Figure 2-7. The middle sidewall section was fabricated from a specially designed refractory concrete rated for service at up to 1400 °C. The upper section and lid were made from locally obtained limestone-common sand concrete. The detailed chemical compositions of the lower section concrete sidewalls and basemat are provided later in this section. The concrete and MgO were contained within flanged 11 gauge steel forms that secured the lower section to the balance of the existing test section components with an aluminum transition plate. The lower section was constructed with vertical, flanged casting seams between the MgO and concrete so that the sidewalls could be disassembled to reveal the solidified corium following each test. The MgO sections were reused, while the concrete sidewall remnants were disposed of as radioactive waste.

A layer of crushed UO_2 pellets was used to protect the interior surface of the MgO sidewalls against thermo-chemical attack by the corium. In the event that the UO_2 layer did not provide adequate protection, 3.2 mm thick tungsten back-up plates were embedded in these sidewalls as a final barrier to terminate sidewall attack. The plates were instrumented to provide an indication of corium contact with either of these two surfaces during the test. As illustrated in

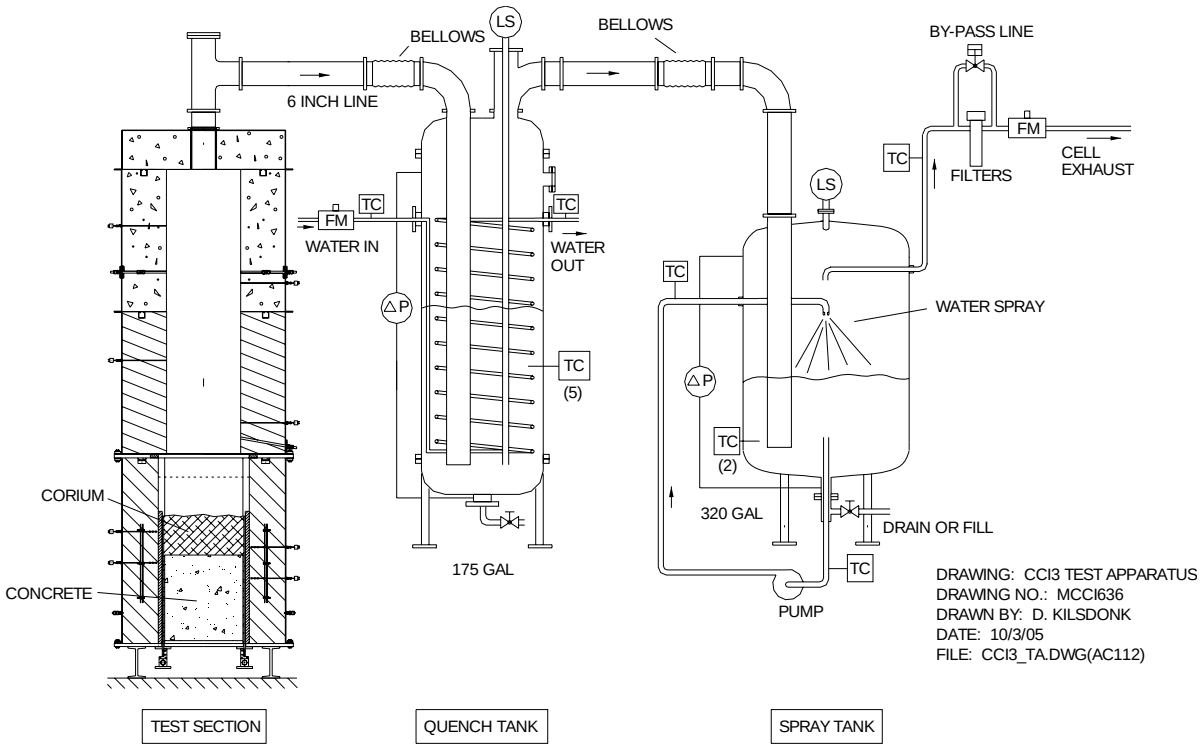

Figure 2-1. Key Elements of the CCI Test Apparatus.

Figure 2-5, multi-junction Type C thermocouple assemblies were also cast within the MgO sidewalls. These thermocouples allowed the time-dependent heat loss from the melt to be estimated from the local temperature gradient and the thermal conductivity of the MgO through standard inverse heat conduction techniques.

Melt pool generation in these tests was achieved through an exothermic "thermite" chemical reaction that produced the target initial melt mass over a timescale of ~ 30 seconds. A depiction of the powder loading scheme is provided in Figure 2-8. As is evident from the figure, two iron/alumina sparklers, wrapped with nichrome starter wire, were positioned a few centimeters below the top of the corium charge near the centerline of the test section. One of these sparklers was used to initiate the thermite reaction by heating the neighboring powder to the ignition

Figure 2-2. Overview of the Facility.

point. (The thermite compositions are described in detail later in this section). The second sparkler was provided as a backup in case the first failed to ignite the material.

After the chemical reaction, DEH was supplied to the melt to simulate decay heat through two banks of tungsten electrodes that lined the interior surfaces of the opposing MgO sidewalls. As illustrated in Figures 2-5 and 2-6, the copper electrode clamps were attached to a 2.5 cm thick aluminum bottom support plate that formed the foundation for the apparatus. A total of sixty three 91 cm long, 0.95 cm diameter tungsten electrodes were attached to each electrode clamp at a pitch of 1.9 cm. A photograph showing the electrodes after installation in the clamps but prior to placement of the lower section MgO sidewalls is provided in Figure 2-9. The clamps were attached with water-cooled bus bars to a 560 kW AC power supply. As shown in Figure 2-4, each electrode bank was vertically restrained by a horizontally mounted, 0.95 cm diameter tungsten rod which was recessed into the concrete sidewalls near the tops of the electrodes. These restraints were provided to prevent slumping of the electrodes away from the sidewalls due to the weight of the crust that formed at the melt/water interface after cavity flooding, as occurred in the MACE Scoping Test.[21]

As illustrated in Figure 2-4, the electrodes spanned a total width of 120 cm on each sidewall of the lower section. At the start of the experiment, the electrical current was drawn through the center 50 cm

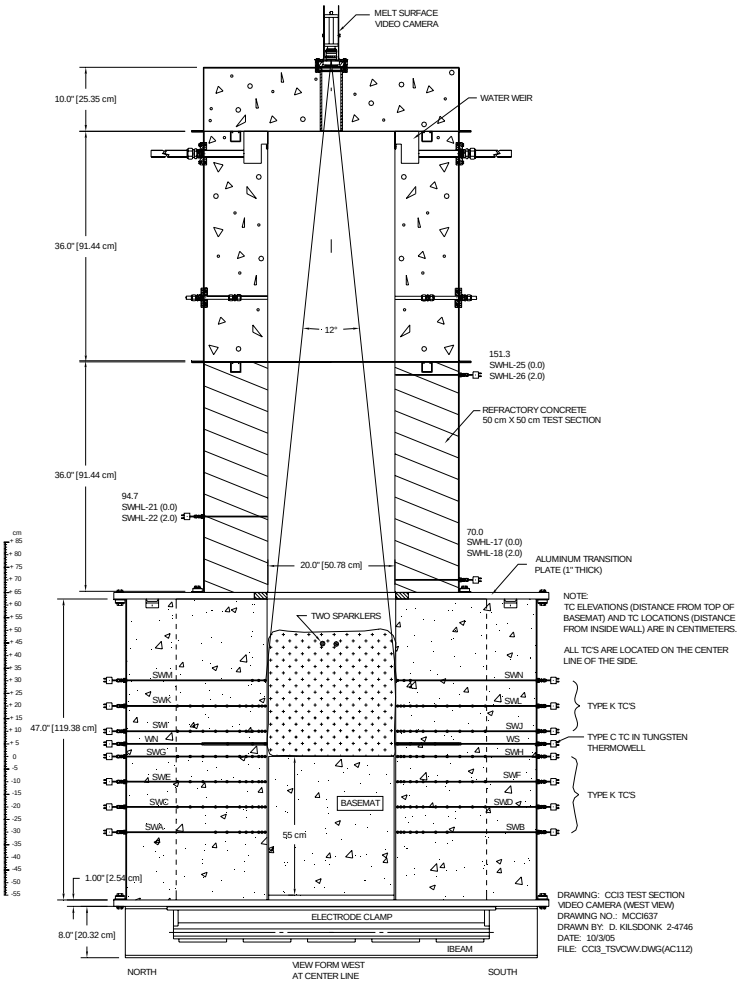

Figure 2-3. Details of the Test Section.

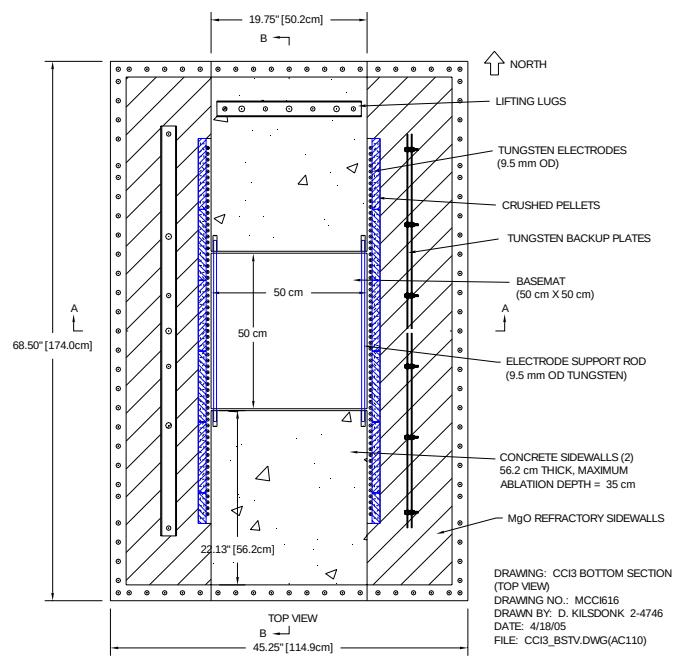

Figure 2-4. Top View of Lower Test Section.

lateral span of electrodes that were in direct contact with the melt. As the test progressed and the concrete sidewalls eroded, additional electrodes were exposed to the corium. Electrical current was drawn through these newly exposed heating elements, thereby maintaining a uniform heating pattern in the melt over the course of the experiment. Given the overall electrode span of 120 cm, then up to 35 cm of lateral ablation could be accommodated in this design while maintaining uniform heat input. As shown in Figure 2-4, the concrete sidewalls were 56 cm thick, which provided 21 cm of remaining sidewall thickness once the 35 cm lateral ablation limit had been reached.

Water was introduced into the test section through two weirs located in the upper sidewall section just beneath the lid of the apparatus. The layout of the weirs is shown in Figure 2-10. A total of nine penetrations were cast into the upper lid of the test section. Of these penetrations, six were utilized for the CCI tests: one stationary lid video camera view port, a port for an insertable water level depth probe, a 15 cm main steam line to the quench system, two light ports, and a port for an insertable crust lance. An illustration of the lid camera installed in the test section is shown in Figure 2-3.

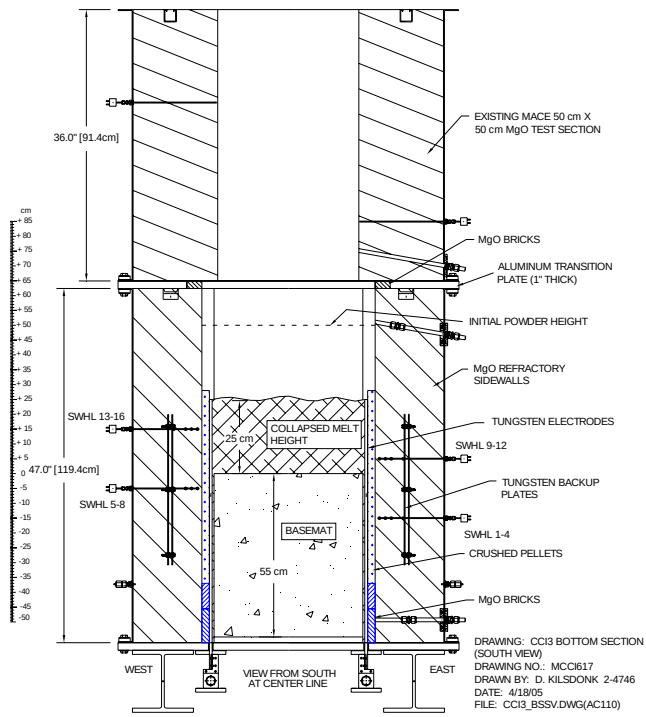

Figure 2-5. Side View of Lower Section Showing Inert MgO Sidewalls.

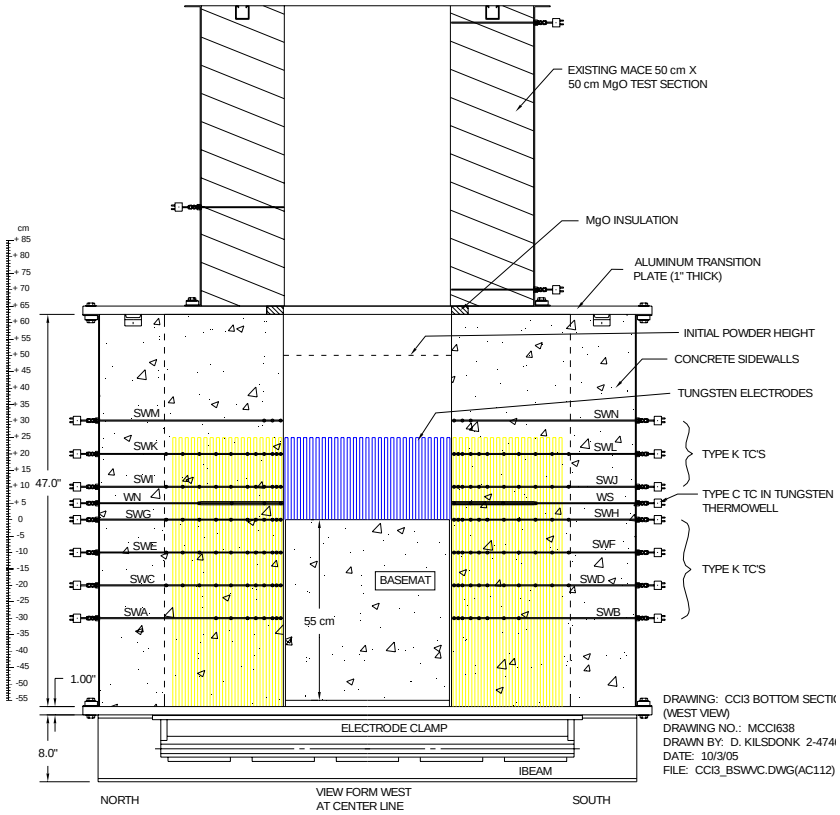

Figure 2-6. Side View of Lower Section Showing Concrete Sidewalls.

The insertable crust lance was designed to fail the crust at the melt/water interface to obtain data on the *in-situ* crust strength and the transient crust breach cooling mechanism. An illustration of the crust lance installed in the test section is shown in Figure 2-11. The lance was made from 2.54 cm diameter, 304 stainless steel rod with a pointed tip. The lance was equipped with an electrical isolation hub so that there was no need to terminate DEH power input during the crust loading procedure. As shown in Figure 2-11, the driving force for the lance was simply a 450 kg dead weight that was remotely lowered with the crane during the test. The lance assembly was equipped with a load cell and displacement transducer to record load vs. position data as the force was applied to the crust. Data from these instruments, as well as the crust thickness determined as part of the posttest examinations, provided the information needed to evaluate the crust strength.

The test section components were bolted together on an elevated steel bed within the test cell using zirconia felt and silicon gasket material to seal the flanges. An illustration is provided in Figure 2-12. Additional reinforcement of each test section component

Figure 2-7. Sidewall Components after Fabrication.

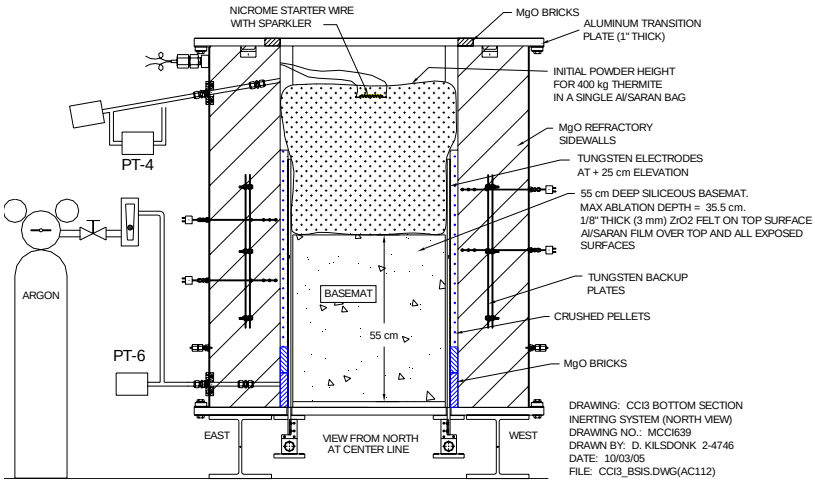

Figure 2-8. Thermite Powder Loading Scheme.

Figure 2-9. Lower Section Prior to Placement of MgO Sidewalls.

was provided by clamping bars installed horizontally in both the North-South and East-West directions. Details of the clamping bar installation are provided elsewhere.[14-16]

2.2 Water Supply System

The water supply system consisted of a 1900 l capacity tank connected to the flooding weirs in the north and south sidewalls of the top test section through a valve-controlled supply line that provided water to the test section at a specified flow rate. A schematic illustration of the supply system is provided in Figure 2-13; details of the flooding weirs were shown previously in Figure 2-10. The supply system flowmeter, pressure transducer, level sensor, and thermocouple instrumentation locations are also shown in Figure 2-15.

Water flow through the system was driven by an 80 kPa differential pressure in the supply tank at a nominal flow rate of 120 lpm (2 l/s). This inlet water flow rate corresponded to a melt/water heat flux of approximately 20 MW/m^2 based on a specific enthalpy of 2.6 MJ/kg for saturated steam at atmospheric pressure, assuming heat transfer occurs through boiling of the overlying coolant. The water flow rate was monitored with a paddlewheel flowmeter. Both the initial water inventory (125 l) and makeup were provided through pneumatic ball valve RV-1, which was opened as needed at the control console to maintain the water volume inside the test section constant at a target level of 125 ± 13 l (50 ± 5 cm). A redundant supply line, activated by pneumatic ball valve RV-2, was provided in case RV-1 failed to open during the test. A third pneumatic valve, RV-3, was provided in case RV-1 or RV-2 failed in the open position. The tests were initiated with valve RV-3 in the open position.

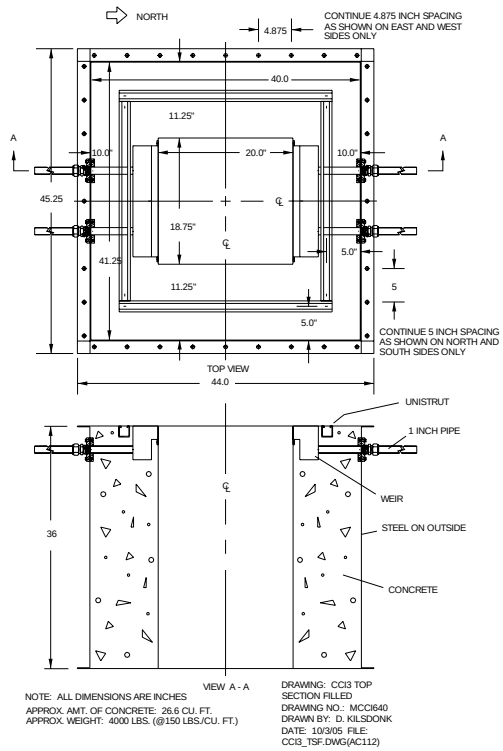

Figure 2-10. Details of the Top Test Section.

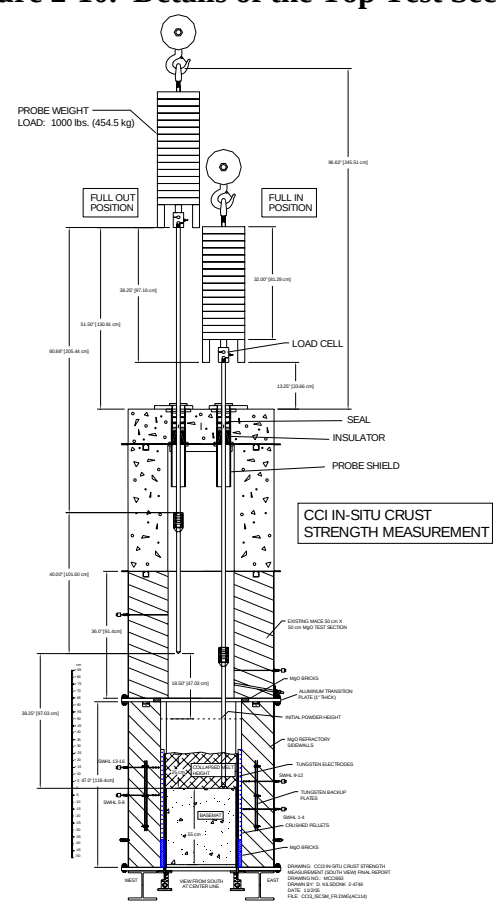

Figure 2-11. Crust Lance Assembly.

Note from Figure 2-13 that the supply line to the test section contained a manual bypass valve downstream of water injection valves RV-1 and RV-2. This valve was vented to a catch pan equipped with an alarmed water detector. During pretest procedures, this valve was left in the open position to divert any water leakage away from the test section. The alarm was intended to notify personnel that a leak was present so that corrective action could be taken. This valve was closed as one of the final steps of pretest operations just prior to evacuation of the cell.

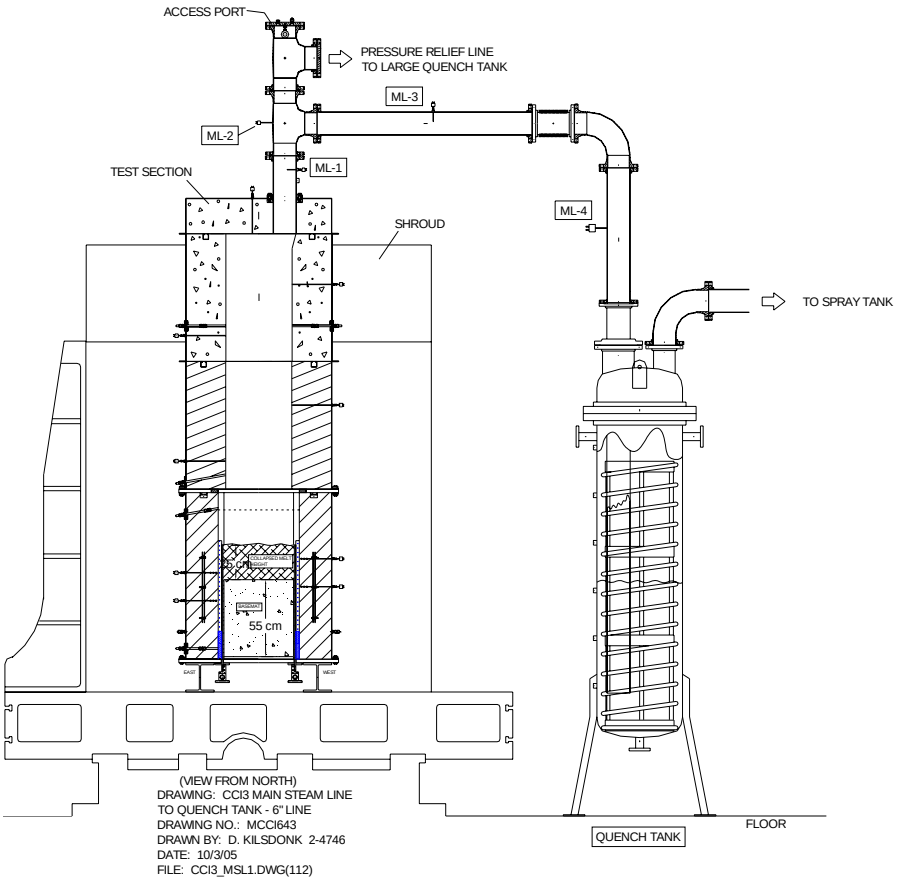

Figure 2-12. Test Section Mounted on the Platform.

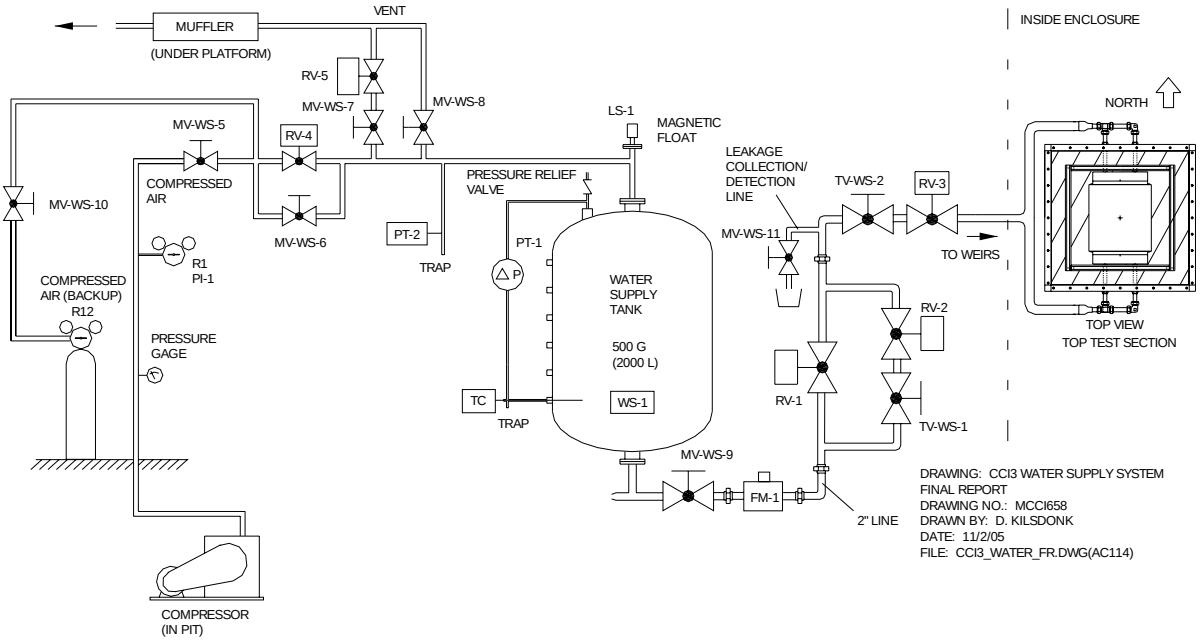

Figure 2-13. Test Section Water Supply System.

2.3 Quench System

The quench system, shown in Figures 2-14 and 2-15, consisted of a primary quench tank, a secondary spray tank, and a condensate overflow tank. The quench system flowmeter, pressure transducer, level sensor, and thermocouple instrumentation locations are also shown in these two figures.

Steam and concrete decomposition gases passed from the test section through a 16.1 cm ID stainless steel pipe into the 680 l capacity, 60 cm ID primary quench tank. This tank contained an initial water inventory of 250 l. With this amount of water, a pool void fraction of ~ 60% could initially be accommodated before the voided water height reached the top of the tank. The quench tank was equipped with a 1.9 cm diameter cooling coil to remove heat from steam condensation, thereby maintaining a subcooled state. The coil water flow was drawn from the building supply system. The coil water flow rate was throttled to nominally 38 lpm, which corresponded to a heat sink of 210 kW assuming a water heat capacity of 4200 J/kg•K and a temperature rise of 80 °C across the coil. If the condensate level in the tank rose to a level of 560 l, spillover into the adjacent 930 l overflow tank occurred through a 2.5 cm ID pipe. The quench tank, and the interconnecting piping between the test section and quench tank, were insulated to minimize heat losses.

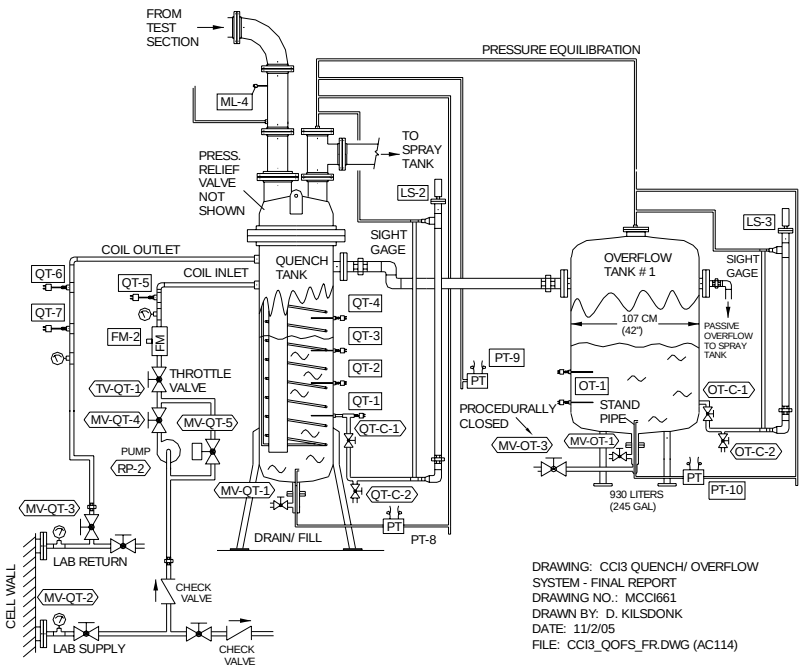

Figure 2-14. Quench and Overflow Tanks.

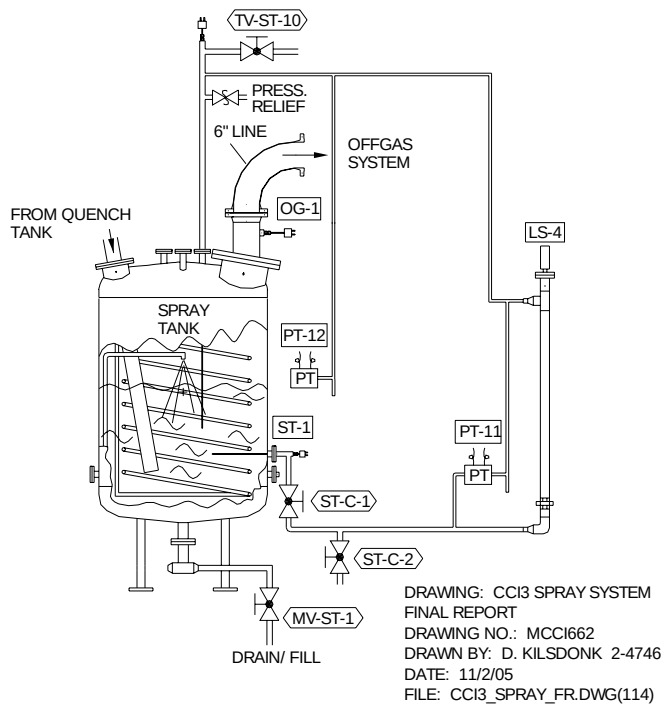

Figure 2-15. Spray Tank.

The secondary 1230 l capacity spray tank was connected to the quench tank by a 16.1 cm ID stainless steel pipe. In situations where the steam generation rate overwhelmed the primary quench tank, the secondary spray tank served to condense the remaining steam. This tank

contained an initial water inventory of nominally 380 l. With this amount of water, a pool void fraction in excess of 60% could be accommodated before the voided water height reached the top of the tank. The spray tank and interconnecting piping between the spray and quench tank were also insulated to minimize heat losses.

2.4 Test Section Pressure Relief System

A pressure relief system was provided to prevent over-pressurization and possible failure of the test section. A schematic illustration of the system is shown in Figure 2-16. The system consisted of a 16.1 cm vent line from the test section to an auxiliary tank containing a nominal initial water inventory of 400 l. The auxiliary tank had an inside diameter of 1.22 m and a capacity of 4100 l. The tank was open to the atmosphere. The pressure relief line to the tank was equipped with a passive, counter-weighted check valve set to open at a differential pressure of nominally 68 kPa. A rupture diaphragm (68 ± 13.4 kPad failure pressure) upstream from the check valve prevented any flow through the line unless the pressure in the test section exceeded the design value of 68 kPad. As shown in Figure 2-16, the relief line was also equipped with a 7.5 cm vacuum breaker valve. This valve was provided to prevent water hammer from occurring due to steam condensation should the pressure relief valve open and then reseat after water had been introduced into the test section.

The initial water inventory in the auxiliary tank was provided to cool gases from the test section and to remove aerosols before noncondensables present in the gas stream passed into the cell atmosphere. The tank was instrumented with a Type K thermocouple to measure water temperature, as well as a differential pressure transducer to measure water depth. The instrumentation locations are shown in Figure 2-16. The instruments were provided so that the steam condensation rate could be determined should the pressure relief valve open during the test. In this manner, there would be no loss of data should the pressure relief system activate.

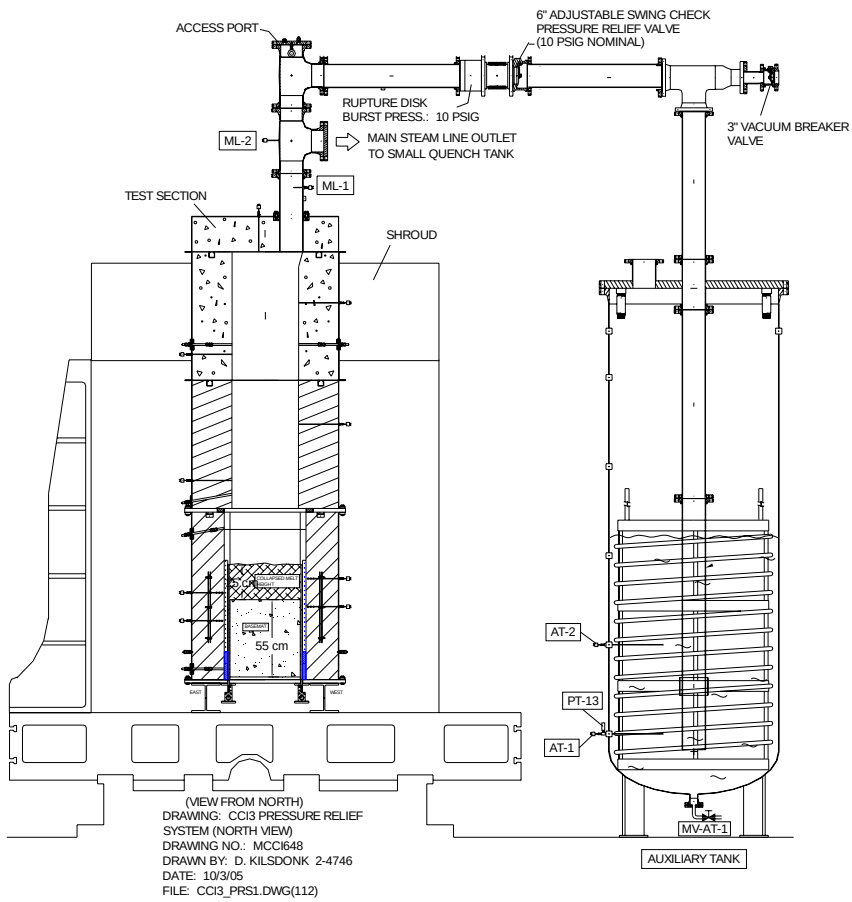

Figure 2-16. Test Section Pressure Relief System.

2.5 Off Gas System

An illustration of the off gas system is provided in Figure 2-17. Thermocouple and flowmeter instrumentation locations are also shown in this figure. This system filtered and exhausted the noncondensable concrete decomposition gases, as well as the test section covergas, to the cell exhaust. The decomposition gases (H_2, CO, CO_2) and cover gas exited the spray tank and passed through a flow separator. The cleanup efficiency of this separator was 99% of all entrained solid and liquid when the particle size exceeded 10 microns. After passing through the flow separator, the flow was vented through a 10 cm diameter line to a filter bank to remove any remaining particulate. The flow then passed through the final off gas flowmeter to the cell atmosphere. The filters were equipped with a passive counter-weighted check valve set to open at a nominal differential pressure of 7 kPa. The bypass valve was provided to ensure that a vent path for the test section was always available in the event that the filters become plugged during the experiment.

2.6 Cover Gas System

During the test a uniform flow rate of helium was fed into the test section to suppress burning of combustible concrete decomposition gases (H_2 and CO) and to protect test section internals. An illustration of the cover gas system is shown in Figure 2-18. Cover gas flow was modulated by a total of three Hastings Flow Controllers (FC's). One 0-200 slpm FC provided cover gas to the lid camera and light port penetrations, while a second 0-350 slpm FC provided dedicated cover gas flow to the lid camera to prevent aerosol deposition on the camera quartz window through which the melt upper surface was viewed. A third 0-100 slpm FC was used to inert the apparatus on the evening prior to the test.

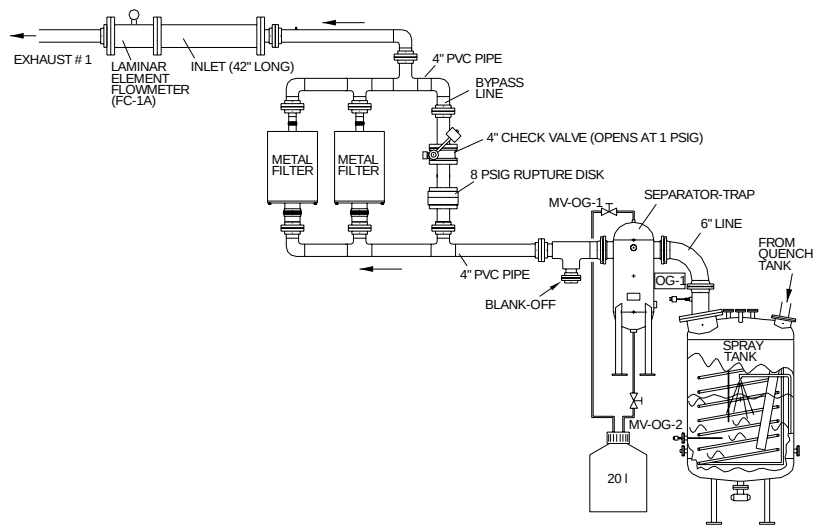

Figure 2-17. Off Gas System.

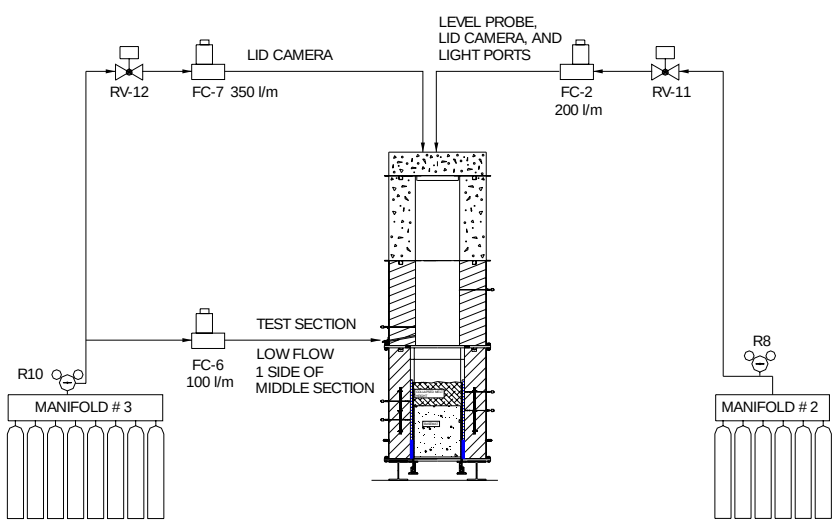

Figure 2-18. Cover Gas System.

2.7 Power Supply

The power for Direct Electrical Heating (DEH) of the corium was provided by a 0.56 MW single phase AC power supply manufactured by NWL Transformers. Output of the power supply was voltage or current controlled. The supply had four voltage/current ranges: 56.4 V/10 kA, 113 V/5 kA, 169 V/3.3 kA, and 226 V/2.5 kA. The power supply was connected to the two arrays of tungsten electrodes in the test section through water cooled copper pipes. The total voltage drop through the water cooled pipes and tungsten electrodes at operational temperature and maximum current was calculated to be less than 0.5 V. The leakage current through the overlying water pool after the cavity was flooded was estimated to be less than 1% of the total current.

2.8 Concrete Compositions

As shown in Table 1-1, concrete type was the key parametric variation among the three tests conducted as part of the experimental series. Both tests CCI-1 and CCI-3 were conducted with siliceous concrete, but the raw materials were of different geographic origin, while test CCI-2 was conducted with Limestone-Common Sand (LCS) concrete. The chemical compositions of the three concrete types are shown in Table 2-1. The reader is referred to the individual data reports[14-16] for additional information regarding the engineering compositions (i.e., mix ratios) and aggregate size distributions for each concrete type. The compositions shown in Table 2-1 were determined through chemical analysis of samples taken from concrete archives that were prepared while fabricating the basemat and sidewall components for each test. The chemical analysis was performed by the Analytical Chemistry Laboratory (ACL) at Argonne;[22] the reported measurement uncertainty is ± 5% of the value shown in the table for each constituent.

To prevent downward migration and possible escape of concrete decomposition gases during the course of the experiments, the electrode penetrations through the bottom support plate were sealed using O-rings. As a part of normal pretest operations, the test sections were leak checked at a differential pressure of 83 kPa and found to have very low leak rates. On this basis, essentially all concrete decomposition gases migrated upwards through the melt pool during the experiments, as opposed to partial loss through the bottom support plate of the apparatus. Reinforcing rod was eliminated so that it did not mask or delay the attainment of a fully oxidized melt. To prevent thermal shock of the concrete basemat and sidewalls during the initial chemical reaction, the concrete surfaces were protected by a thin (3

Table 2-1. Chemical Composition of Concretes.

Oxide	CCI-1 Wt%	CCI-2 Wt%	CCI-3 Wt%
Al_2O_3	0.77	2.49	3.53
CaO	8.54	25.88	16.79
Fe_2O_3	0.79	1.39	1.49
MgO	0.60	11.47	0.85
MnO	0.00	0.03	0.04
K_20	0.12	0.55	0.81
SiO_2	82.48	21.61	59.91
Na_2O	0.00	0.31	0.66
SrO	0.00	0.00	0.04
TiO_2	0.051	0.135	0.155
SO_3	0.514	0.505	0.434
CO_2	0.901	29.71	9.80
H_2O, Free	1.808	3.255	2.293
H_2O, Bound	1.92	1.11	1.40
Total	98.48	98.47	98.19

mm thick) layer of low density (~ 480 kg/m^3) ZrO_2 felt. After the exothermic reaction was complete, the felt dissolved into the melt.

The densities of the concretes used in the tests are shown in Table 2-2. These densities were calculated on the basis of the measured mass and volumes of the archive samples for each test. Instrumentation locations within the sidewalls and basemat are described later in this section.

Table 2-2. Concrete Densities.

Test	Concrete Density (kg/m^3)
CCI-1	2300
CCI-2	2330
CCI-3	2270

2.9 Corium Compositions

As shown in Table 1-1, the initial corium compositions for all three tests were typical of a fully oxidized PWR core melt containing various proportions of calcined concrete as an initial constituent. The compositions of the concrete additives were consistent with the type of concrete used for the sidewalls and basemat for each test. Aside from lowering the melting point of the mixtures,[23] the additives were incorporated to account for concrete erosion that is expected to occur during the corium spreading phase following breach of the Reactor Pressure Vessel (RPV).[24] As part of the development work for the SSWICS test series,[3,5] specially designed exothermic chemical mixtures (or "thermites") were developed to produce the particular melt compositions shown in Table 1-1. The reader is referred to the individual data reports[14-16] for additional information regarding the details of the thermite designs.

The initial bulk melt compositions produced from these reactions are summarized in Table 2-3, while the detailed pre- and post-reaction compositions are provided in Table 2-4. Note that these compositions do not include an additional mass of crushed UO_2 pellets (typically 350 kg) that was used as a protective layer for the cast MgO sidewalls behind the two banks of tungsten electrodes (see Figures 2-4 and 2-5). This material did not participate in the initial exothermic chemical reaction. The pellets were recovered and weighed following each test. This information, as well as chemical analysis of the final melt compositions, indicated that the pellet layer remained essentially intact as an inert protective layer during test operations, with little if any of the material dissolving into the melt.

As shown in Figure 2-8, the thermite powders were packed into the test section in a large aluminized bag that was pre-installed over the basemat. The total weight of bagging material was typically 150 g, which amounted to an average contaminant level of ~ 0.04 wt% based on the charge masses shown in Table 2-4. This step was taken to minimize moisture uptake by hygroscopic chemicals in the thermite (CrO_3, CaO, and SiO_2). Excessive moisture uptake was an operational concern since the moisture reacted with metallic constituents to form hydrogen during the thermite reaction. As an additional measure to minimize moisture uptake, exposed concrete surfaces were covered with bagging material before the thermite was loaded. See Figure 2-9 for a photograph showing the film installed over the basemat and sidewalls.

Table 2-3. Initial Melt Compositions for CCI Test Series.

Constituent	CCI-1 (Wt%)	CCI-2 (Wt%)	CCI-3 (Wt%)
UO_2	60.97	60.62	56.32
ZrO_2	25.04	24.90	23.13
Calcined Concrete	8.08[a]	8.07[b]	14.14[a]
Cr	5.91	6.41	6.41

[a]Calcined siliceous concrete: 79.0/0.9/15.6/4.5 wt% SiO_2/MgO/CaO/Al_2O
[b]Calcined LCS concrete: 42.0/14.1/38.8/5.1 wt% SiO_2/MgO/CaO/Al_2O_3

Table 2-4. Detailed Pre- and Post-Reaction Thermite Compositions for CCI Tests.

Chemical	CCI-1				CCI-2				CCI-3			
	Reactant		Product		Reactant		Product		Reactant		Product	
	Wt%	Mass (kg)	Wt%	Mass (kg)	Wt %	Mass (kg)	Wt %	Mass (kg)	Wt %	Mass (kg)	Wt %	Mass (kg)
U_3O_8	63.38	253.52	-	-	63.01	252.04	-	-	58.70	220.34	-	-
UO_2	-	-	60.97	243.88	-	-	60.62	242.48	-	-	56.32	211.41
Zr	18.53	74.12	-	-	18.42	73.68	-	-	17.16	64.41	-	-
ZrO_2	-		25.04	100.16	-	-	24.90	99.60	-	-	23.13	86.82
Si	1.00	4.00	-	-	1.03	4.12	-	-	1.57	5.89	-	-
SiO_2	4.23	16.92	6.38	25.52	1.18	4.72	3.39	13.56	7.84	29.42	11.17	41.92
Mg	0.04	0.16	-	-	0.69	2.76	-	-	0.07	0.26	-	-
MgO	-	-	0.07	0.28	-	-	1.14	4.56	-	-	0.12	0.45
Al	0.20	0.80	-	-	0.22	0.88	-	-	0.09	0.34	-	-
Al_2O_3	-	-	0.38	1.52	-	-	0.41	1.64	-	-	0.64	2.40
CaO	1.25	5.00	1.25	5.00	3.13	12.52	3.13	12.52	2.21	8.31	2.21	8.31
CrO_3	11.37	45.48	-	-	12.32	49.28	-	-	12.36	46.40	-	-
Cr	-	-	5.91	23.64	-	-	6.41	25.64	-	-	6.41	24.06
Total	100.00	400.00	100.00	400.00	100.00	400.00	100.00	400.00	100.00	375.37	100.00	375.37

2.10 Instrumentation and Data Acquisition

The CCI facility was instrumented to monitor and guide experimental operation and to log data for subsequent evaluation. Principal parameters which were monitored during the course of the test included the power supply voltage, current, and gross input power to the melt; melt temperature and temperatures within the concrete basemat and sidewalls; crust lance position and applied load; supply water flow rate; water volume and temperature within the test apparatus, and water volume and temperature within the quench system tanks. Other key data recorded by the DAS included temperatures within test section structural sidewalls, off gas temperature and flow rate, and pressures at various locations within the system. An overview of the instrumentation for the CCI test series is provided in Table 2-5; complete instrument lists are provided in the individual data reports for each test. [14-16]

All data acquisition and process control tasks were managed by a PC executing LabVIEW 6.i under Windows XP. Sensor output terminals were connected inside the test cell to model HP E1345A 16-channel multiplexers, which were integrated into a mainframe chassis in groups of eight. An illustration of the DAS setup is provided in Figure 2-19. The multiplexers directed signals to an HP E1326B 5 ½ digit multimeter incorporated into each chassis. Three independent 128 channel systems were used for a total capacity of 384 channels.

Signal noise was reduced by the digitizer through integration over a single power line cycle (16.7 ms). The digitized sensor readings were routed from the test cell to the PC in the control room via two HP-IB extenders. The extenders allowed the ASCII data from the HP to be sent through the cell wall over a BNC cable. The extender within the control room then communicated with a GPIB card within the PC. This configuration also permitted remote control of the multimeter through LabVIEW.

Integration of the signal over the period of a power line cycle limited the speed with which the multiplexer could scan the channel list. The theoretical minimum scan time was ~1.7 s (i.e., 16.7 ms • 100 channels per chassis). Though the three systems operated independently, implying the ability to update all 300 channels in ~ 2 seconds, the actual time required for the update was about 5.5 seconds.

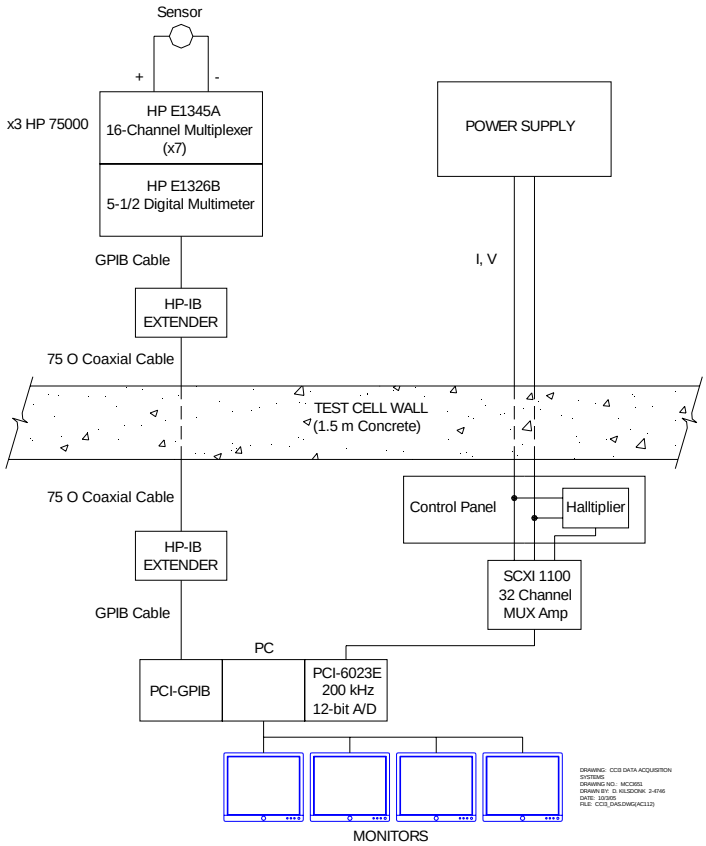

Figure 2-19. DAS Setup for CCI Tests.

Table 2-5. Summary of CCI Test Instrumentation.

Parameter	Number of Sensors	Type of Sensor
Concrete Basemat (67)		
Temperature (axial ablation front location)	47	Type K thermocouple
Temperature (axial melt distribution)	20	Type C thermocouple
Concrete Sidewalls, Lower Test Section (63 for each sidewall)		
Temperature (lateral ablation front location)	55	Type K thermocouple
Temperature (lateral melt distribution)	8	Type C thermocouple
Inert MgO Sidewalls, Lower Section (20)		
Temperature (heat loss to walls)	16	Type C thermocouple
Voltage potential (tungsten back-up plates)	4	Direct*
Upper Sidewalls & Lid (10)		
Temperature (heat loss to walls)	10	Type K thermocouple
Test Section/Main Steamline Internal (14)		
Temperature	7	Type K thermocouple
Pressure/water head	4	Strain gage pressure sensor
Gas flow	3	Mass flowcontroller/flowmeter
Water Supply, Quench, and Pressure Relief Systems (25)		
Temperature	11	Type K thermocouple
Pressure/water head	8	Strain gage pressure sensor
Water level	4	Magnetic level float
Water flowrate	2	Paddlewheel flowmeter
Power Supply (5)		
Voltage	1	Direct*
Current	2	Current transformer
Power	2	Hall-effect Wattmeter
Offgas System (2)		
Temperature	1	Type K thermocouple
Flowrate	1	Mass flowmeter
Crust Lance (2)		
Position	1	Potentiometer
Applied Load	1	Strain gage force sensor
Electrode Current Monitors (32)		
Voltage	32	Direct*

*Digital voltmeter/multiplexer

As shown in Table 2-5, instrumentation was selected to provide the necessary measurements to determine the time-dependent 2-D concrete ablation profile and the melt temperature distributions. Plan and elevation views of a typical basemat thermocouple layout are provided in Figures 2-20 and 2-21, respectively, while typical concrete sidewall instrument locations are shown in Figures 2-3 and 2-6.[d] The thermocouple elevations shown in these figures are all taken with respect to the original height of the basemat surface (Z=0).

Both the concrete sidewalls and basemat were instrumented with multi-junction Type K thermocouple assemblies to determine the 2-D ablation profile as a function of time. In addition, Type C thermocouple assemblies in 9.5 mm diameter long-body tungsten thermowells protruded upwards from the basemat and laterally inwards from the concrete sidewalls in several locations. The purpose of these instruments was to provide data on the axial and lateral melt temperature distributions as a function of time. A total of five four-junction (basemat) and two eight-junction (sidewalls) Type C arrays (36 junctions total) in tungsten thermowells were used in most tests. Photographs showing the thermocouple assemblies installed in the basemat and sidewall forms prior to placement of the concrete are provided in Figure 2-22 and 2-23, respectively.

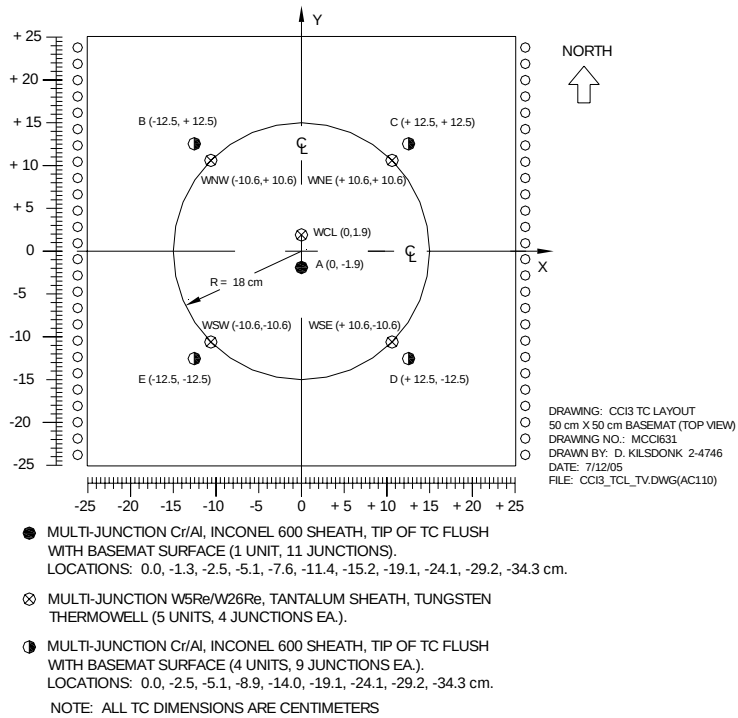

Figure 2-20. Plan View of Basemat Instrumentation.

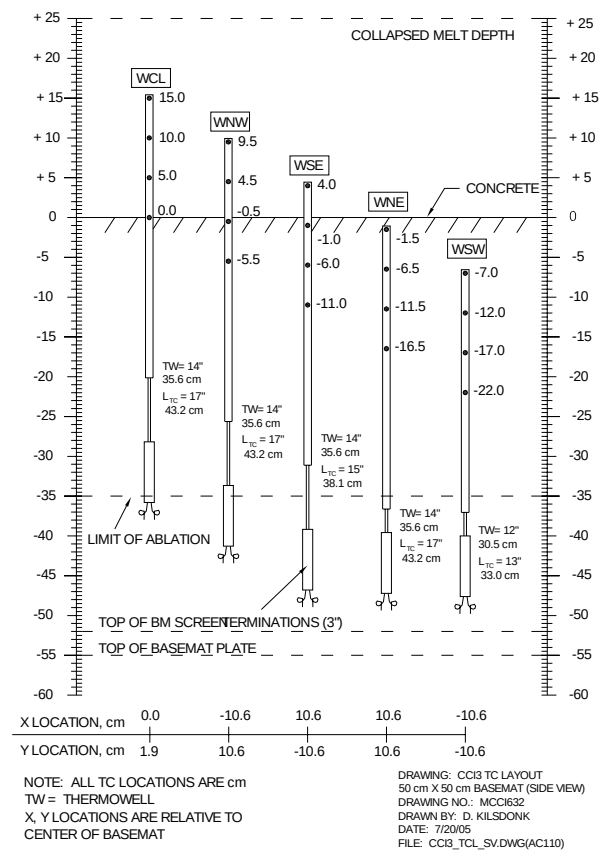

Figure 2-21. Elevation View of Basemat Type C Thermocouple Locations.

[d]The number and location of basemat and sidewall instruments varied slightly from test-to-test. Consult the individual data reports[14-16] for detailed descriptions of the actual instrument locations and nomenclature.

The MgO sidewalls of the lower test section, as well as the upper sidewall sections, were instrumented with a total of 26 Type K and Type C thermocouples to measure the sidewall heat up prior to water addition, and also to measure the sidewall cooling rate above the melt surface after water was added. Illustrations of these thermocouple locations are provided in Figure 2-3 and 2-24.

Several methods were provided for monitoring water level in the test section. One method consisted of a differential level probe which was inserted through a sealed penetration in the lid. The probe was maintained in a retracted position during dry cavity operations, up until water was added to the test section. After water was added, the probe was inserted to a distance of ~ 50 cm from the initial basemat surface (25 cm from the initial collapsed melt surface). The probe tip was also instrumented with two Type K thermocouples that monitored the plenum gas temperature prior to water addition; thereafter, these thermocouples measured the water temperature over the melt surface. The probe tip location above the melt surface after insertion is shown in Figure 2-24.

Figure 2-22. Thermocouples Installed in Basemat Form.

Figure 2-23. Thermocouples Installed in Sidewall Form.

Aside from the insertable water level probe, two additional methods were provided to monitor the water volume in the test section. The first was a static water level port located in the North sidewall 55 cm from the initial basemat surface (30 cm from the initial collapsed melt surface). The port location is shown in Figure 2-24. The second redundant method was provided by an on-line calculation of the water volume in the test section based on conservation of mass for the water volume in the system, which was fixed at the start of the test.

Water levels in the water supply and quench system tanks were monitored with magnetic floats. As a redundant level measurement technique, all tanks were equipped with differential pressure transducers to monitor water heads. Water flow rate to the test section from the supply tank, in addition to the water flow rate through the primary quench tank cooling coil, were

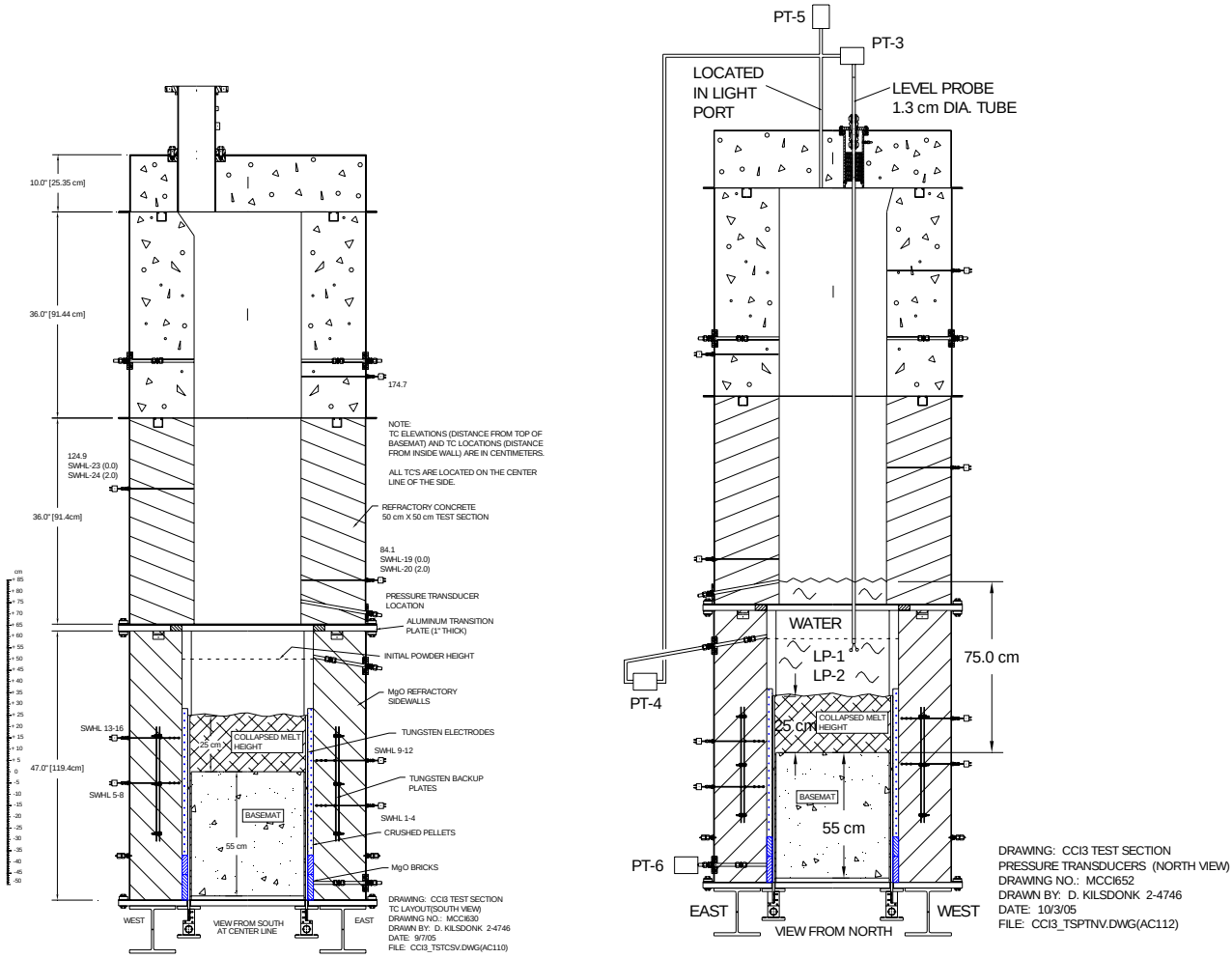

(a) **(b)**

Figure 2-24. Test Section (a) Sidewall Thermocouple and (b) Pressure Transducer Locations.

monitored with paddlewheel flow meters. Transient water temperatures in all tanks, as well as the temperature differential across the quench tank cooling coil, were monitored using Type K thermocouples. The main steamline between the test section and quench tank was also instrumented with Type K thermocouples to measure the local gas and structure temperatures. The outlet noncondensable gas flow rate from the spray tank was monitored by a Hastings mass flow transducer. The locations of these instruments are shown in Figures 2-12 through 2-17.

Key system pressures were monitored with strain-gauge type pressure transducers. As shown in Figures 2-15 through 2-17 and 2-24, the pressure in all system tanks was monitored, and also the test section plenum pressure. An additional transducer was located in the lower test section to monitor the pressure beneath the melt upper surface. This transducer was mounted on the east sidewall of the test section at an elevation of 45 cm beneath the initial concrete surface. As described earlier, the gap between the MgO sidewalls and the electrodes was packed with crushed UO_2 pellets during corium loading. Thus, this transducer recorded the pressure beneath the melt surface as long as the gap remained unplugged during the test.

In terms of the power supply operating parameters, voltage drop across the tungsten electrode bank is monitored with the DAS voltmeter, while current input is monitored with two parallel 5000:1 current transformers. Power input to the melt was monitored with two Hall Effect meters. For tests CCI-2 and CCI-3, additional instrumentation was installed in an attempt to monitor current through selected tungsten electrodes to determine if non-uniformities in the

DEH power input occurred during the test. Due to space limitations, this system was limited to monitoring the voltage drop across the lower 15 cm of selected electrodes using lacquer-insulated 14 gauge wires that were passed through potted seals into the test section along the bottom support plate and clamped at the 15 cm elevation. Given the resistivity of tungsten, then a voltage drop of ~ 20 mV should develop over the 15 cm length for every 200 Amps of current drawn. Figure 2-25 shows the electrodes that were wired for current monitoring in tests CCI-2 and CCI-3. This system was marginally successful insofar as providing useful data. The reader is referred to the test data reports[15-16] for additional information regarding the test results.

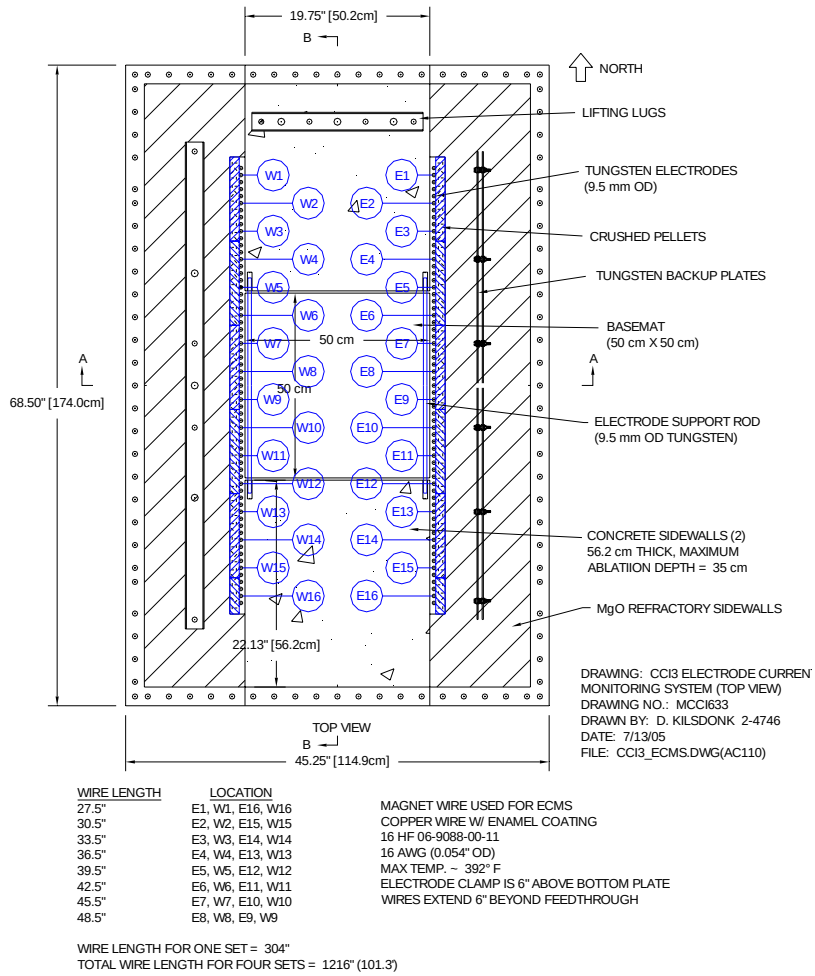

Figure 2-25. Electrode Current Monitoring System Layout.

In addition to the above instrumentation, visual information regarding the core-concrete interaction and melt quenching behavior was provided by a video camera mounted on the upper lid of the apparatus. The camera location and field of view are shown in Figure 2-3. Five area video monitors were also used to monitor for leaks, and to record any disruptive events should one occur. Finally, the crust lance was equipped with load and displacement transducers to provide data on the crust load vs. time during the crust failure sequence.

2.11 Test Procedures

Pretest Operations

Assembly of the apparatus began by installing the tungsten electrodes (126 total; 63 per side) into machined copper electrode clamps. The electrode clamps were then attached to the bottom of the 2.54 cm thick aluminum support plate which served as the foundation for the entire apparatus. With the electrode clamps installed, the support plate was moved into position on the steel platform that supported the apparatus. The concrete basemat was then placed atop the

support plate. The top surface of the basemat was insulated with a 3 mm thick layer of low density ZrO_2 felt. The basemat was then completely covered with a continuous sheet of 1.7 mil aluminized Saran film to prevent moisture contamination of the thermite powders from the basemat once the powders were loaded into the test section. The lower test section concrete and MgO sidewalls were then set in place. The concrete sidewalls were also covered with ZrO_2 felt and aluminized Saran before placement to prevent moisture contamination of the thermite from these components. The lower section flange bolts and clamping bars were then installed and torqued according to an approved procedure.

In parallel with test section assembly, the thermite powders were mixed in preparation for corium loading. As a precursor for initiating mixing, a gas sample test[a] was conducted to verify that the initial level of volatile impurities in a sample prepared from the thermite constituents to be used for a given test was sufficiently low to preclude excessive gas release during the burn. Upon successful completion of this test, mixing was initiated.

Once the lower section was assembled, preparations for loading of the corium charge began. A single, large 1.7 mil aluminized Saran bag was preinstalled over the basemat. During loading, the nominally 400 kg thermite charge was placed within this bag in order to reduce the amount of bagging material present in the thermite. As the powders were placed in the test section, the basemat melt temperature thermocouples were monitored to detect any localized heating in the corium powders. If heating was observed, the cell was to be immediately evacuated. As the thermite was placed, the gap between the tungsten electrodes and MgO sidewalls was filled with crushed UO_2 pellets. The crushed pellets served as a protective layer against excessive chemical/thermal attack by the corium during the test. Once loading was completed, two sparkler igniters were placed a few centimeters below the top of the powders near the center of the test section, and then the bag was folded and sealed. An illustration of the loading scheme is provided in Figure 2-8. As described in Section 2.9, the use of the single large bag for containment of the thermite resulted in a low bagging material contaminant level of nominally 0.04 wt % present in the charge at the time of ignition.

Once loading was completed, a removable train containing a 1.0 kg bagged sample of thermite was installed over the powder bed; an illustration is provided in Figure 2-26. The sample train was removed weekly and the sample weighed to monitor the moisture pickup by the thermite during the period between loading and test initiation. Note from Figure 2-26 that the top portion of the train also contained a 4.5 kg canister of desiccant. The desiccant was provided to maintain the plenum gas as dry as possible during pretest operations. As an additional measure to prevent moisture accumulation in the powder bed, the lower test section was continuously purged with argon (2 slpm) from the time loading was completed until the test was initiated.

After installation of the sample train, the remainder of the test apparatus was assembled. This included installation of the transition plate, two upper sidewall sections, and finally the enclosure lid. Peripheral instrumentation was then installed on the lid and sidewalls of the test section. The main steamline run from the test section to the primary quench tank was completed, as well as the pressure relief line from the test section to the auxiliary tank. (The main steamline

[a] The gas sample test procedure consists of igniting a representative sample of the thermite in a closed vessel. The amount of noncondensable gas produced is determined from the ideal gas law; the composition of the evolved gases is determined using gas mass spectroscopy.

was closed off from the test section using an insertable blank-off plate throughout pretest operations to preclude moisture migration from the quench tank into the test section).

After assembly was completed, extensive system checkout procedures were performed to ensure that the facility was in proper working order. This included a proof test of the test section at 83 kPad, which is 20 % in excess of the pressure relief system activation pressure of 69 kPad. The pressurization gas for this test was argon. An insertable blind flange was installed upstream of the rupture disk in the pressure relief line to isolate this system. During the test, the apparatus was gradually pressurized to the proof pressure of 83 kPad. After a 1 minute hold at this pressure, the system was isolated to determine the leak rate. The leak rate of all the assembled CCI test sections was found to be $\leq$ 4.6 kPa/min (20 slpm) at a nominal pressure of 55 kPad, which was significantly below the acceptance criterion (i.e., < 2 % of the expected peak gas/vapor generation rate during the tests).

Pretest preparations culminated with a final full system checkout that involved remotely running all equipment with the power supply in operation across a water cooled dummy load. Once the full system check was completed, final system preparations were carried out. These efforts included: (i) hookup of the power supply to the tungsten electrodes through water cooled buss bars, (ii) installation of the final piping connection between the water supply tank and the test section, and (iii) removal of the sample train from the test section. Following connection of the power supply to the electrode clamps, the key for the power supply lockout located in the cell, as well as the key for the interlock located on the control room console, were assigned to a custodian who kept the keys in their possession until the test was initiated. This step was taken to preclude inadvertent activation of the power supply.

Over the several weeks spanning pretest operations, the thermites within the test sections gradually absorbed moisture. Peak moisture pick up for the test series was limited to 0.19 wt%, which was well below the maximum permissible level of 0.3 wt %. This was the last criterion that needed to be satisfied before final approval was granted to proceed with test operations.

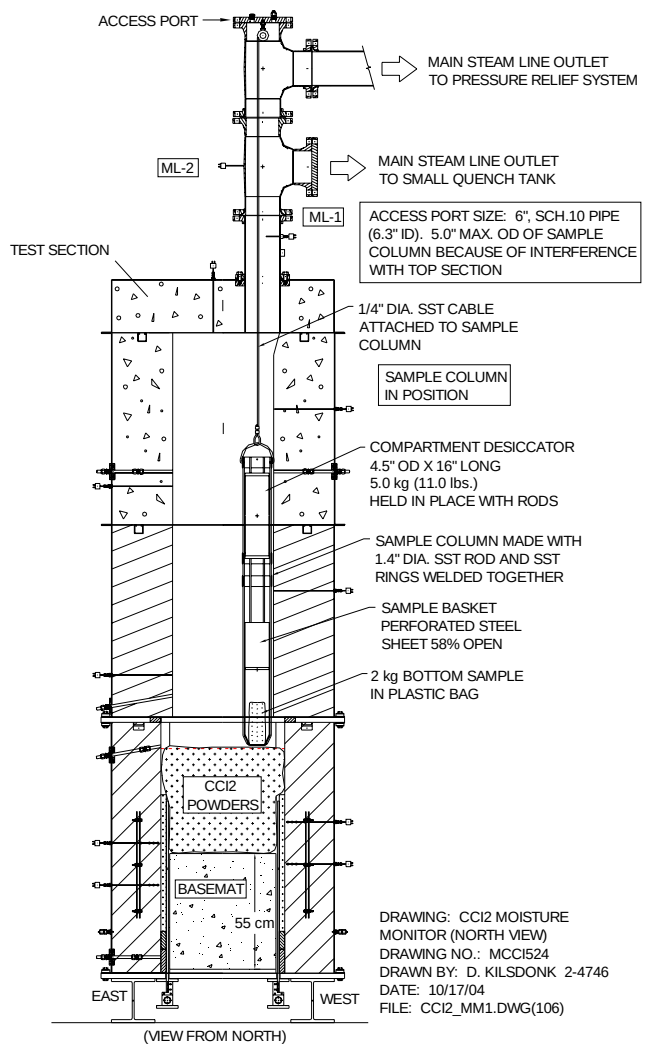

Figure 2-26. Thermite Sample Train.

Test Operations

The planned operating procedure was essentially the same for all three tests. This procedure is described below. The actual test event sequences are summarized in the next Chapter as part of the presentation of the test results.

On the evening prior to the experiment, the apparatus was inerted with a slow bleed of helium into the test section. On the day of the experiment, the apparatus was brought up to operating conditions, a final walk through inspection was performed by operating personnel, the thermite igniter was hooked up, and finally the power supply was energized before the containment was evacuated and sealed. Data acquisition was initiated, and the Video Camera Recorders (VCRs) were started. Coolant and cover gas flows were brought up to design conditions, and the cell ventilation system was closed and sealed. After verifying that operating personnel were at their assigned positions, power was applied to the nichrome wire/sparkler located at the top of the powder charge. Thermite ignition was clearly evident on the lid video camera that viewed the top of the powder bed (see Figure 2-3); based on this information, ignition was announced and logged in the control room. Based on readings from thermocouples located near the bottom of the charge, completion of the burn was also announced and logged. (Thermite burn times ranged from 32-40 seconds for all three tests).

At completion of the burn, the power supply operator initiated a current ramp at a rate of ~ 3000 Amps/minute up to target power. As shown in Table 1-1, target power was 150 kW for CCI-1, while target power was reduced to 120 kW for CCI-2 and CCI-3. After target power was reached, the input power would be held constant at target power for 5.5 hours of dry core-concrete interaction, or until a 30 cm ablation depth was reached in either the lateral or axial direction. After one of these two criteria was met, the cavity would then be flooded. However, if a crust was present at the melt upper surface, the crust lance would be used to fail the crust prior to flooding so that the water would be able to contact the underlying melt. Following water addition, the power supply operation would be switched from constant power at the target level to a constant voltage operating mode. This approach would keep the specific power density in the remaining melt zone approximately constant should a solidification (quench) front develop during the interaction (recall that the DEH technique does not appreciably heat solidified corium). Forty five minutes after water addition, or after the debris cooling rate had been reduced to a relatively low level, the crust would be failed with the lance to obtain data on the transient crust breach cooling mechanism. After breach, power supply operations would continue for an additional 45 minutes, yielding a total operating period of 90 minutes with water present in the cavity, or until the ablation limit of 35 cm was reached in either the lateral or axial directions. At this point, the input power would be turned off and the test was terminated. The primary datasets from the experiment were then backed up, and the DAS was restarted in a slow recording mode (1 scan per minute) to record additional information during the long term cooldown. The system was then left unattended overnight.

Posttest Operations

On the day after the experiment, a Health Physics Technician made the initial reentry into the containment cell and performed a survey to determine if any radioactive material had escaped from the apparatus during the test. In all cases, this survey turned up negative. On this basis, personnel reentered the cell and began the normal disassembly process.

Instrument cabling on the apparatus was disconnected and rolled back to terminal boxes in the cell. Peripheral instruments and equipment (i.e., video cameras, pressure transducers, lance load assembly, water level insertion probe drive) were then removed, cleaned, and stored. The test section reinforcing bars and flange bolts were then removed, cleaned, and stored.

At this point, physical disassembly of the test section was initiated. This phase of the work was carried out in anti-contamination suites and full face respirators according to an approved Radiation Work Permit (RWP). The test section main steamline and pressure relief line were removed from the lid, cleaned, and stored. The test section lid and top sidewall section were then removed, cleaned, and stored. At this point, photographs were taken to document the debris state in the as-found condition. Following this step, the middle sidewall section was removed, and splattered corium that had solidified on the inner surfaces of this component was collected and weighed. The middle section was then cleaned and stored.

Removal of the middle section fully revealed the lower test section that contained the solidified core material. At this point, the top surface of the solidified corium could be examined in detail and characterized. Photographs were taken, and measurements of the upper surface elevation profile were made. Sidewall crust material above the upper crust was then removed, collected, and weighed. Any suspended crust material that was present over the bulk of the solidified corium was then collected, characterized, and weighed. A second set of photographs and surface elevation profile measurements were then obtained. During this stage of disassembly, samples were collected for subsequent chemical analysis to determine elemental composition to better characterize the debris distributions.

Following these steps, a large platform drill was used to obtain an axial core sample of the solidified debris remaining over the basemat near the center of the test section. The core specimen produced by this procedure allowed additional samples to be obtained for chemical analysis to characterize the corium axial composition variation.

After the debris upper surface was characterized, the two inert MgO sidewalls that backed up the tungsten electrodes (see Figures 2-4 and 2-5) were then removed, cleaned, and stored. During this step, the remnants of the crushed UO_2 pellet liner that served as a protective layer behind the tungsten electrodes was collected and weighed. After additional photographs were taken, the North and South concrete sidewalls were removed with the cell crane and set on the platform for examination. During this step, the corium fractured vertically along a plane that roughly followed the original inner surface of the concrete walls. After the concrete walls were set out of the way, the solidified corium over the basemat was lifted from between the two banks of tungsten electrodes and placed on the platform for examination. The basemat and concrete wall remnants were then photographed, and additional measurements were taken to better characterize the overall debris distribution. Additional samples were collected for chemical analysis to provide information on the corium lateral composition variation.

Following these steps, the basemat and sidewall remnants were placed in heavy gauge sheet metal storage containers. The containers were then moved to an adjacent cell for archival storage. With the test specimens out of the way, the electrodes were removed from the clamps on the test section bottom plate. The plate and clamps were then cleaned and stored. Following these steps, the cell was decontaminated back to a shoe cover area, which completed the posttest operations phase of the experiment.

3.0 RESULTS AND DISCUSSION

This section presents the major thermalhydraulic and posttest examination results for the three CCI experiments conducted as part of the test series. A discussion that compares and contrasts key results is provided at the end of this section. Specifications for the three tests are provided in Table 1-1.

3.1 Test CCI-1 Results

As shown in Table 1-1, Test CCI-1 investigated the interaction of a fully oxidized Pressurized Water Reactor (PWR) core melt, initially containing 8 wt % siliceous concrete, with a two-dimensional siliceous concrete test section (see Section 2.1 for a design description). The siliceous concrete for this test was of the U.S. type; the composition is shown in Table 2-1. For reference, the initial melt composition is provided in Table 2-4. Target input power during dry cavity operation was specified as 150 kW. The planned test operating procedure was detailed in Section 2.11. The actual operating sequence is described below.

Thermalhydraulic Results

Test CCI-1 was performed on December 19, 2003. The event sequence is shown in Table 3-1. Test operations began by initiating the thermite reaction with the nichrome wire located at the top of the charge; the burn time was ~30 seconds. Following the reaction, DEH input to the melt was ramped up to the target power of 150 kW. The power trace for the test is shown in Figure 3-1. Time t=0 in the figures that follow corresponds to the time at which the melt made initial contact with the basemat surface (i.e., at completion of the thermite burn). Target power level was reached at 2.8 minutes, where it was essentially maintained for the balance of the test involving power supply operations.

Onset of ablation was detected at several locations of the basemat upper surface and at the midlevel of both concrete sidewalls within the first minute following melt generation. The thermal response of the basemat at the centerline is shown in Figure 3-2, while the north and south concrete wall thermal responses at the +10.0 cm elevation are shown in Figures 3-3 and 3-4, respectively (see Figures 2-6 and 2-20 for schematics showing the thermocouple array locations). The dimensions shown in the legends for these figures indicate the distance of the thermocouple junctions from the concrete inner surfaces. The sequential rise in the temperatures is indicative of the progression of the ablation front into the concrete. In general, onset of ablation at a given location corresponds to the local temperature reaching the siliceous concrete liquidus temperature of 1250 °C.[23]

At ~ 8 minutes, aerosols within the test section plenum cleared to the point that the melt surface could be seen with the lid video camera. This view revealed the presence of a stable crust at the melt upper surface. The crust was present the entire test. As the dry phase of test operations progressed, melt eruptions were periodically observed through the crust.

As described in Section 2.10, a total of seven multi-junction Type C thermocouple arrays were used to monitor melt temperatures at various axial and lateral locations. Data from the axially configured array located at the basemat centerline is shown in Figure 3-5, while data from the laterally configured arrays located in the North and South sidewalls at the +5.0 cm elevation are shown in Figures 3-6 and 3-7, respectively. Finally, data from all thermocouples that made

Table 3-1. CCI-1 Event Sequence.

Time (Minutes)	Event
-0.5	Thermite burn initiated.
0.0	Melt generation completed; initial temperature ~1950 °C. Basemat surface temperature in SW quadrant reaches siliceous concrete ablation temperature of 1250 °C.
0.4	Onset of ablation detected in NW basemat quadrant and in South sidewall at + 10.0 cm elevation.
0.46	Onset of ablation in North sidewall detected at + 10.0 cm elevation.
2.8	Target input power of 150 kW reached.
7.6-7.9	Aerosol clears in test section, revealing crusted melt upper surface. Several eruptions occur through holes near the center of the crust.
21.6	Onset of basemat ablation detected in NE quadrant.
22.4	Onset of basemat ablation detected in SE quadrant.
31.5	Onset of basemat ablation detected at centerline.
35.9	Crust remelting with eruptions evident along North concrete sidewall.
42.7	Significant aerosol production; eruptions evident in NE corner of test section.
43.8-45.0	Large eruptions and volcanic flow occurring from NE corner of test section.
47.9-49.0	More large eruptions from NE corner of test section.
59.5-60.0	Crust remelts in NE corner, leading to significant melt eruption.
65.8	Crust lance inserted to breach crust present over melt surface.
66.4	Sidewall ablation reaches 29.2 cm depth in North sidewall at +10.0 cm elevation.
67.7	Water addition initiated. Peak debris cooling rate ~ 1 MW/m^2.
78.6	DEH power input to melt terminated on the basis or reaching a 34.3 cm ablation depth in the North sidewall at +10.0 cm elevation.
78.8	Crust breached with lance (peak applied load of 1.41 kN; surface at +21.5 cm elevation). Breach initiates a large eruption; cooling transient peaks at ~ 3 MW/m^2.
119.7	Data acquisition terminated.

contact with melt at each of these three array locations are shown collectively in Figure 3-8 for comparative purposes. The dimensions in the legends again refer to junction elevations with respect to the concrete surfaces. As shown in Figure 3-5, the initial melt temperature in the bulk of the pool was ~ 1950 ºC. As the test progressed, the melt temperature underwent minor perturbations, but generally declined steadily to a final value of ~ 1750 ºC at the time that power input was terminated at 79 minutes.

The progression of the axial ablation front during the test is shown in Figure 3-9, while the analogous set of data for the north and south concrete sidewalls are provided in Figures 3-10 and 3-11, respectively. Finally, the maximum erosion rate measured on each concrete surface is shown in Figure

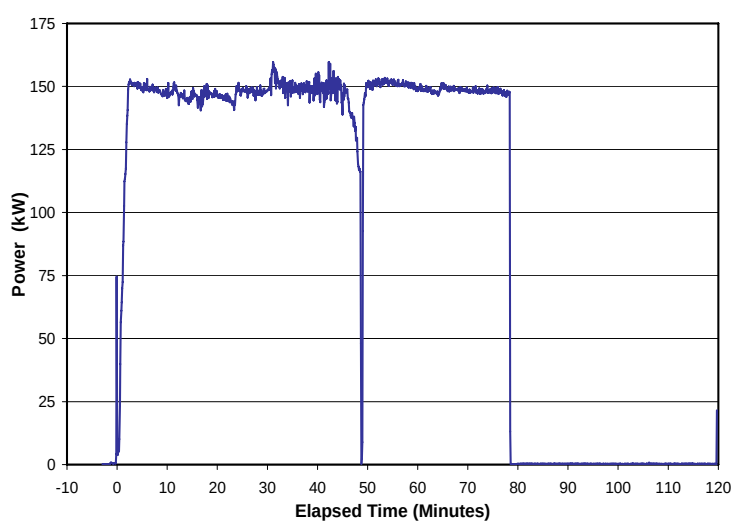

Figure 3-1. CCI-1 DEH Input Power.

3-12. Although onset of ablation was detected at several locations soon after the melt was generated, the Type K TC's located at the basemat centerline and in two of the basemat quadrants remained in the range of 1000-1240 ºC, indicating that initial ablation was non-uniform. Onset of ablation in these three remaining locations was detected over the time interval from 21-32 minutes (see Table 3-1 and Figure 3-9). Thus, during the initial phase of the interaction, the data[14] suggests that at least a portion of the basemat surface was protected by an insulating corium crust that formed upon initial melt contact with the cold concrete surface. The data further suggests that in the time interval from 21-32 minutes, the crust either remelted or mechanically failed, which allowed erosion to commence.

Similar behavior is noted at other locations. In particular, after proceeding to an ablation depth of 1.3 cm in the first minute of the interaction, ablation on the North wall slowed dramatically (see Figure 3-10). Furthermore, the melt temperature adjacent to this surface fell rapidly to near the concrete liquidus temperature of 1250 ºC, indicating the possible presence of a concrete slag layer near this surface. The surface temperature hovered in the range 1200 - 1350 ºC until ~ 45 minutes, at which point the temperature near the wall began to increase rapidly to the average bulk melt temperature (see Figures 3-6 and 3-8). As is evident from Figure 3-10, this temperature escalation was concurrent with a rapid local increase in concrete ablation on the North wall. After this apparent crust remelting and/or failure event, ablation in the North wall proceeded rapidly. In

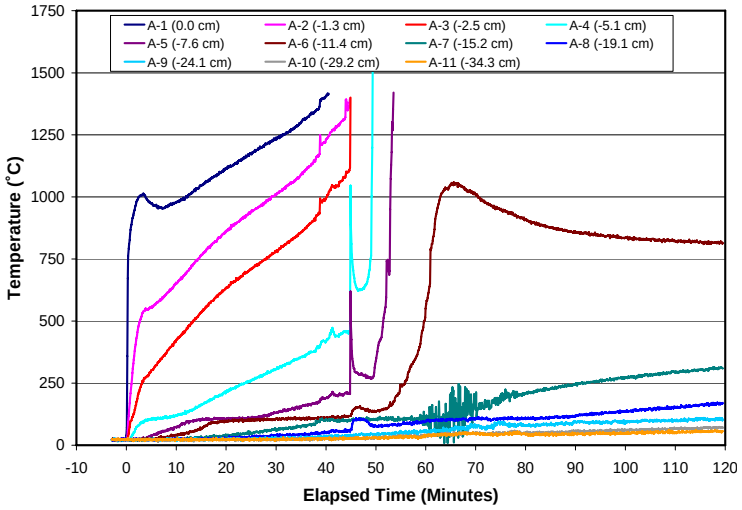

Figure 3-2. CCI-1 Basemat Heatup Near Centerline.

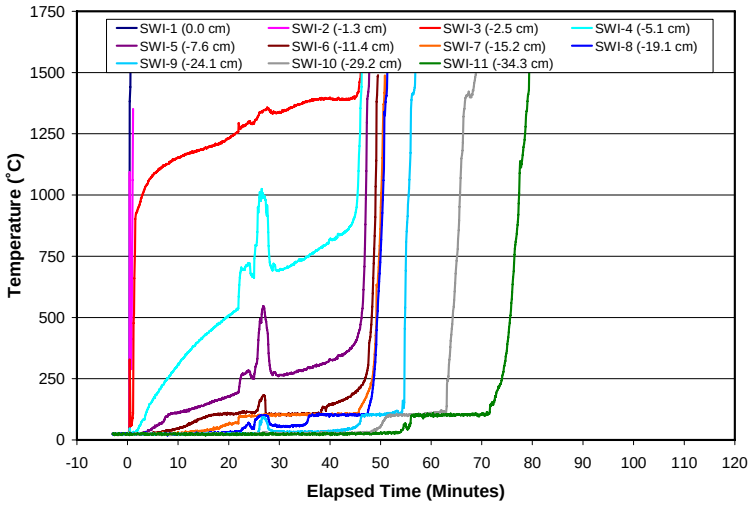

Figure 3-3. CCI-1 North Wall Heatup (+10 cm).

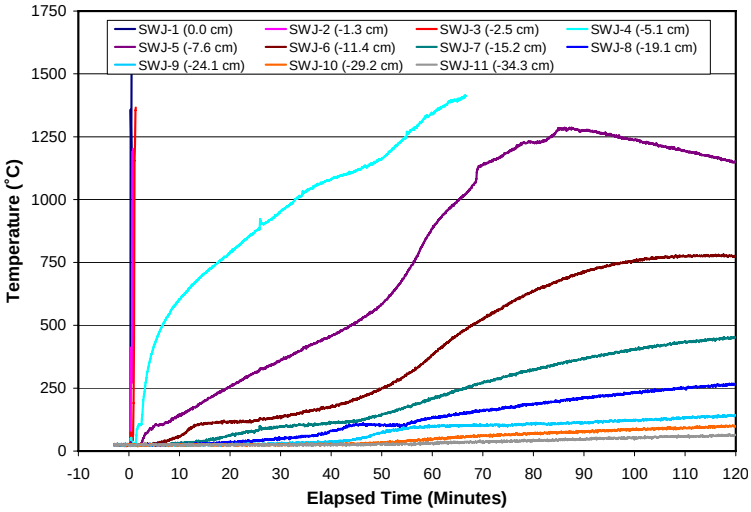

Figure 3-4. CCI-1 South Wall Heatup (+10 cm).

particular, the ablation rate averaged 1.8 cm/min over the time interval from 45.9 to 50.8 minutes as the ablation depth steadily increased from 10 to 19 cm. This behavior can be contrasted with the ablation progression on the South concrete wall. After an initial rapid period of erosion (see Figure 3-11), heatup and remelting of the crust on this wall lagged behind the north wall (see Figures 3-4 and 3-7). This behavior eventually led to a large asymmetry in the ablation profile at the end of the test.

In general, during the course of the test the erosion progression showed evidence of occasional rapid bursts of ablation in various regions of the walls and basemat. Following these phases, there were generally quiescent periods in which the ablation slowed dramatically. Video data indicated that the periods of rapid ablation generally correlated with enhanced melt convection and eruptions through the upper crust, driven by sparging concrete decomposition gases.

After 67 minutes of dry cavity operations, the criterion for flooding of the cavity was reached on the basis of reaching the 30 cm ablation depth in the North concrete wall at the + 10.0 cm elevation (see Figure 3-3). As shown in Table 3-1, the insertable lance was used to breach the crust upper surface prior to water addition, as specified in the test procedure. Immediately after the crust was breached, the cavity was flooded with ~ 125 liters of water to bring the water level over the

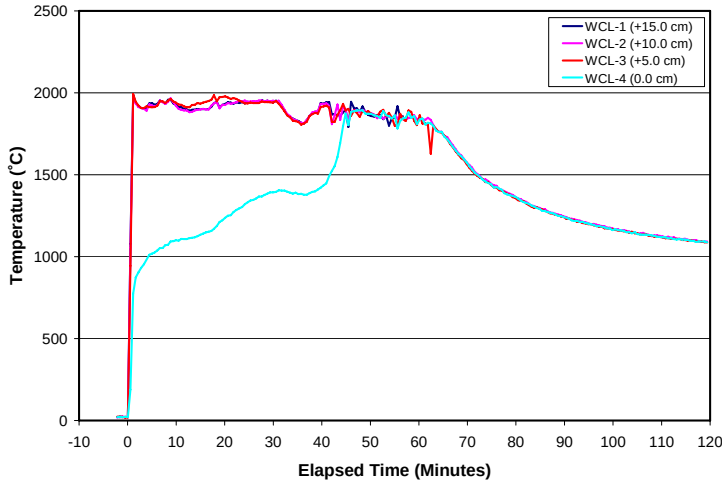

Figure 3-5. CCI-1 Melt Temperatures Near Centerline.

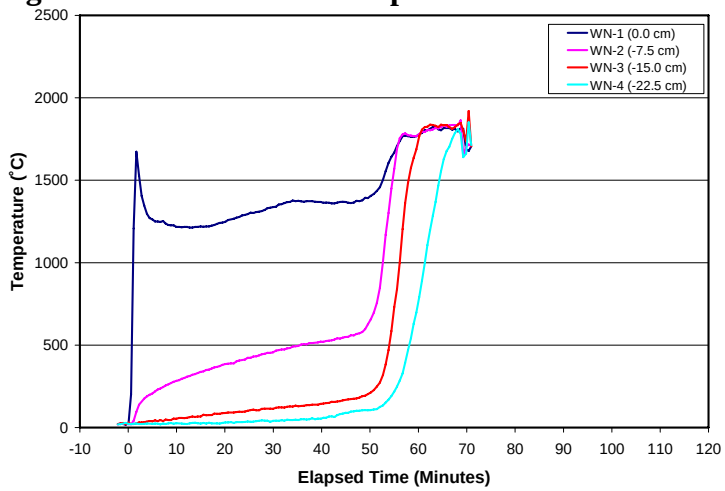

Figure 3-6. CCI-1 Melt Temperatures Near the North Wall (+5 cm Elevation).

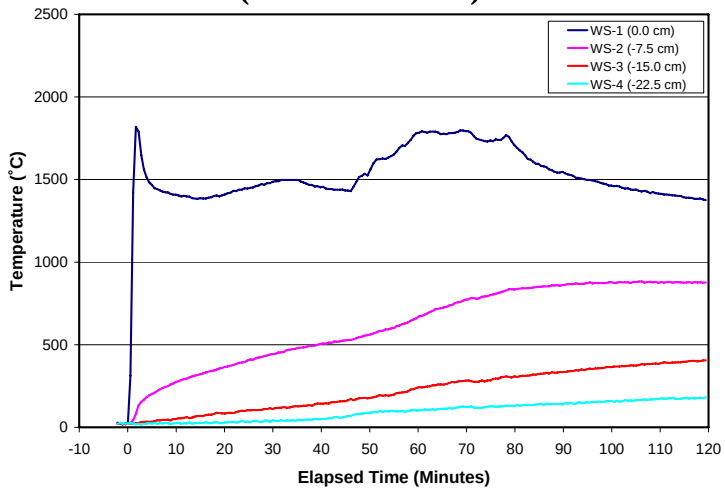

Figure 3-7. CCI-1 Melt Temperatures Near the South Wall (+5 cm Elevation).

melt to ~ 50 cm. After this time, liquid lost to evaporation was periodically replaced to maintain the water level over the melt roughly in the range of 50 ± 5 cm per the test procedure.

The debris-water heat flux, calculated on the basis of the steam formation rate normalized by the test section planar area of 0.25 m^2, is shown in Figure 3-13. As is evident, the peak debris cooling rate upon initial flooding approached the critical heat flux limitation of 1 MW/m^2 under atmospheric boiling conditions. Over the next five minutes of the interaction, the debris cooling rate steadily fell to a plateau at ~ 320 kW/m^2.

Concrete ablation in the North wall continued during the flooding phase of the test. At 79 minutes, the ablation depth reached the test termination criterion of 35 cm, and power input to the melt was halted. The crust lance was used to rupture the crust about 30 seconds after the power was switched off. The lance made initial contact with the crust at a distance of +21.5 cm from the initial basemat surface, which is slightly less than the initial collapsed pool height of ~ 25 cm. The load was steadily increased until the crust failed. As shown in Figure 3-13, crust breach caused a significant increase in the debris cooling rate. In particular, a large melt eruption occurred, resulting in a transient cooling event in which the peak heat flux exceeded 3 MW/m^2. After the breach, the heat flux from the debris upper

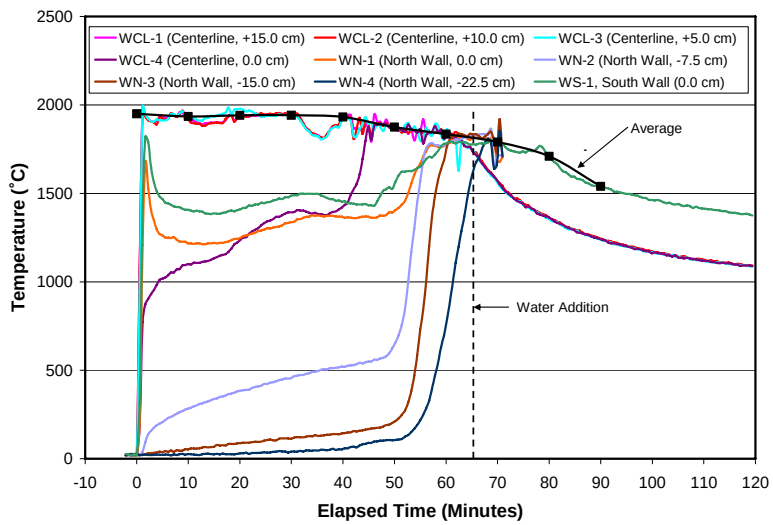

Figure 3-8. Collection of CCI-1 Melt Temperatures.

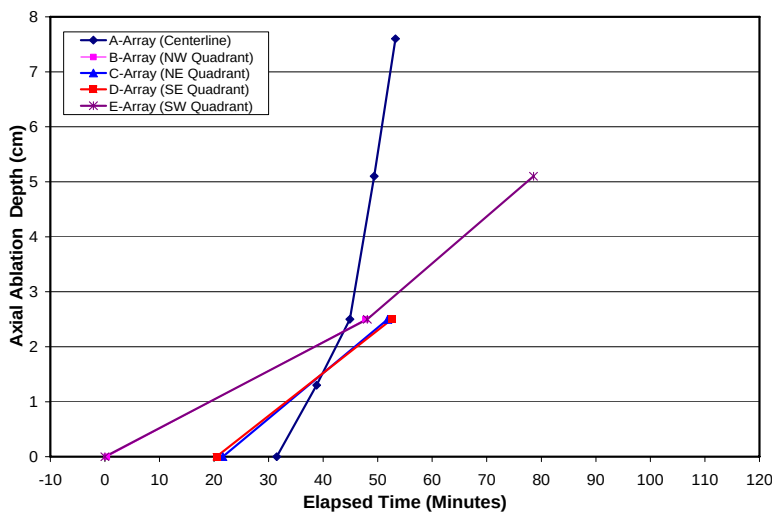

Figure 3-9. CCI-1 Axial Ablation.

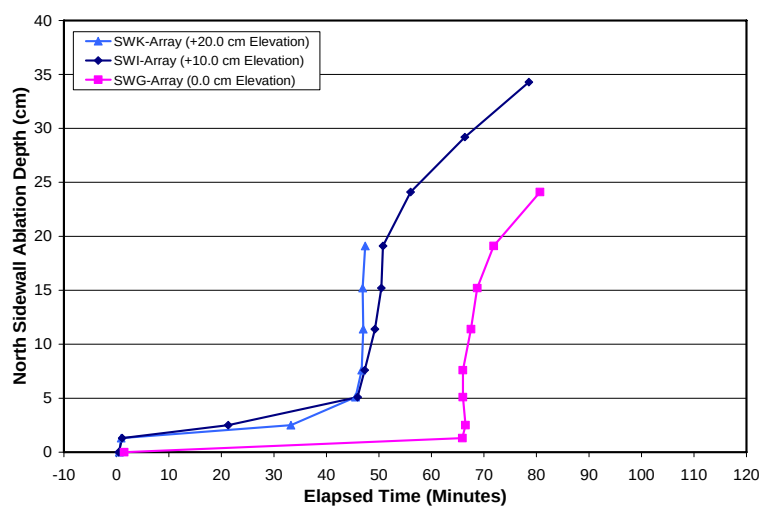

Figure 3-10. CCI-1 North Sidewall Ablation.

surface steadily declined over the next five minutes to a plateau in the range of 250-300 kW/m^2, which is similar to the plateau observed prior to the breach event. In general, the data obtained from the CCI-1 crust breach procedure indicates that these breach events may lead to significant transient increases in the debris cooling rate under plant accident conditions.

As shown in Table 3-1, the applied load on the crust at failure was 1.41 kN. Moreover, posttest examinations (described later in this section) indicate that the crust thickness at breach was in the range of 5 ± 2 cm. With this data, evaluation of the crust strength[5] from well-known analytical solutions available in the literature[25] indicates that the stress in the CCI-1 crust at failure was ~ 1.2 MPa, with an uncertainty range of 0.5 to 3.7 MPa.

Thus, this measurement supports the findings from the SSWICS test series, which indicated that crust material formed during quench is structurally quite weak. However, the CCI-1 strength measurement is significant because it was carried out under prototypic temperature boundary conditions before the material had cooled to room temperature. This can be contrasted with the SSWICS measurements that were carried out at room temperature after the specimens had been removed from the test section.

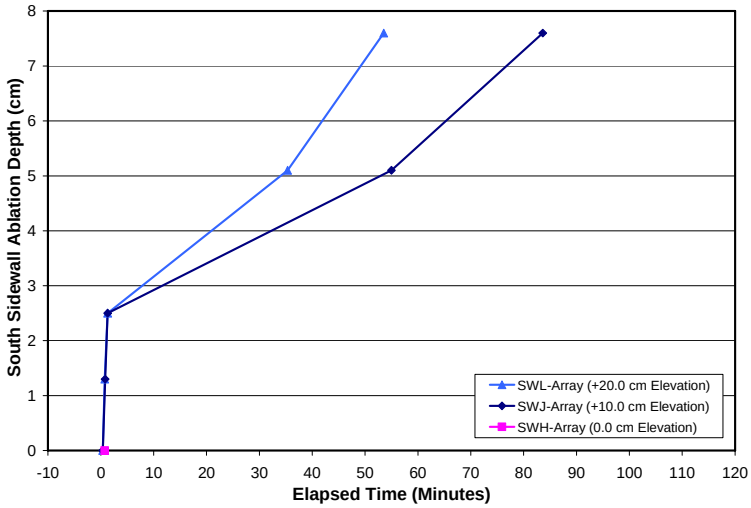

Figure 3-11. CCI-1 South Sidewall Ablation.

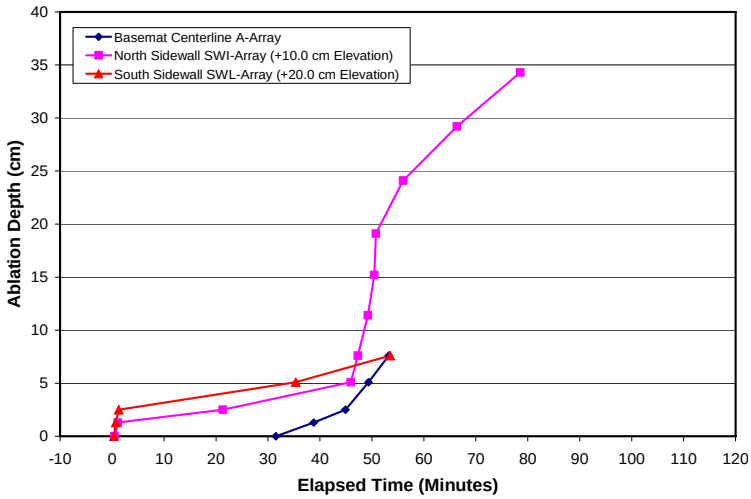

Figure 3-12. CCI-1 Peak Axial and Lateral Ablation Data.

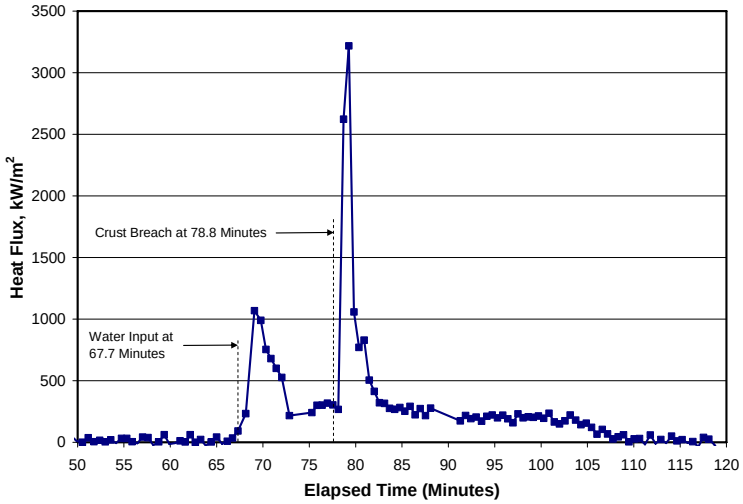

Figure 3-13. CCI-1 Melt-Water Heat Flux.

Posttest Examination Results

As described in Section 2.11, the apparatus was carefully disassembled following the test in order to characterize the posttest debris configuration. Photographs of the top surface of the debris after disassembly down to the lower test section are provided in Figure 3-14. Sidewall crust material from the thermite burn had been deposited on the walls in the lower half of the middle section. The upper surface of the corium was covered with loose debris, principally lava-type material plus particle bed, that originated from the melt eruptions that occurred during dry cavity operations, as well as the eruption that occurred after the crust was breached. Based on large color differences seen between the materials, it appeared as though several different phases were present. Photographs of two different samples of the erupted material are provided in Figure 3-15.

Once the upper surface characteristics were documented, the loose materials were removed to reveal the upper surface of the crust. For reference, the masses of various debris regions recovered during disassembly are provided in Table 3-2. As shown in the table, the amount of material present as a sidewall crust above the solidified melt amounted to 44.6 kg. In future analyses of CCI-1, this mass should be subtracted from the initial melt mass to obtain the actual mass that participated in the core-concrete interaction. Aside from the sidewall crust material, a total of 38.9 kg was present on the crust upper surface in the form of particulate and lava flows that originated from melt eruptions. The material appeared to be in two distinct zones. As shown in the table, 15.6 kg of the material appeared to originate from the melt eruption that occurred following crust breach with water present in the cavity (see Table 3-1), while the balance of the erupted mass was produced during the preceding dry cavity operational period. Removal of the loose materials fully revealed the remnants of the hole that had been produced in the upper crust during thet breach sequence. The hole is visible in Figure 3-14, while a close-up photograph of the opening is provided in Figure 3-16.

(a) **(b)**

Figure 3-14. CCI-1 Debris Upper Surface: (a) As Found Condition, and (b) After Removal of Loose Debris.

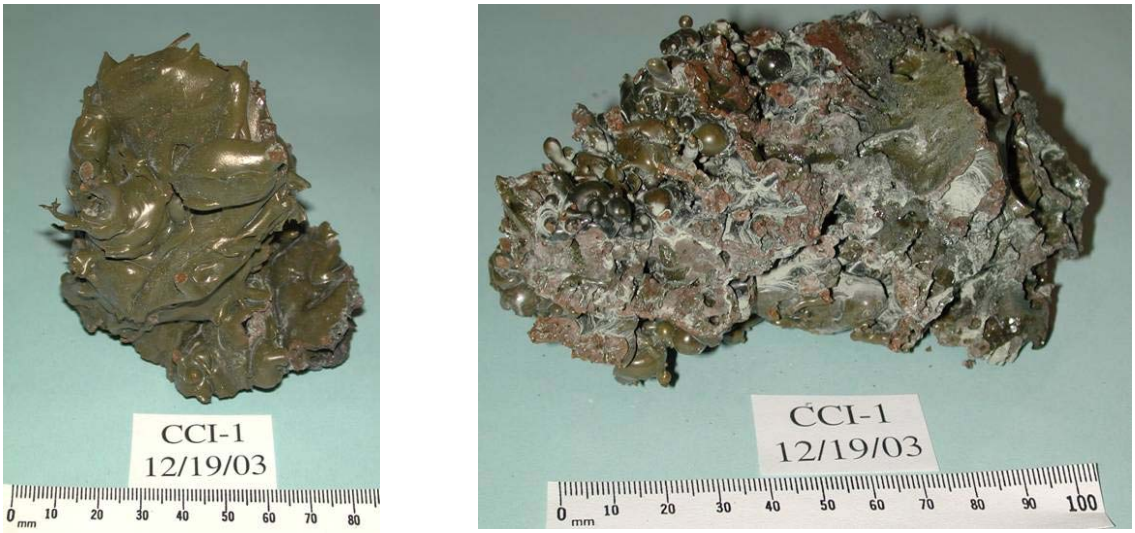

Figure 3-15. CCI-1 Samples of Erupted Material.

Table 3-2. Masses of Material Regions Measured During Disassembly for CCI-1.

Material Description	Mass (Kg)	Note(s)
Sidewall crust material above solidified corium	44.6	This mass should be subtracted from the initial melt mass to obtain actual mass that participated in core-concrete interaction.
Particulate and lava from eruption following crust breach	15.6	This data may be used to estimate corium entrainment coefficients during the various phases of the test.
Lava flows prior to cavity flooding	23.3	
Recovered UO_2 pellets	323.6	A total of 349.9 kg pellets were loaded behind the electrodes. The balance of the material (26.3 kg) was left as a sintered layer on the back of the electrodes.

Prior to initiating removal of the test section sidewalls, a platform drill was used to obtain an axial core sample near the center of the test section. A photograph showing the core sample that was recovered from this procedure is shown in Figure 3-17. The core samples were used to collect specimens for chemical analysis; this data is provided later in the section. The initial view of the axial debris structure through the core hole indicated that the upper region of the debris was composed of a semi-porous layer, while the lower region consisted of a hard, dense oxide. This general debris structure was confirmed as the debris characterization continued.

With these steps completed, the inert MgO sidewalls were removed to gain additional information regarding the debris morphology and overall shape of the cavity erosion profile. A photograph showing the bank of tungsten electrodes after removal of the west sidewall of the test section is provided in Figure 3-18. Sintering of the crushed UO_2 pellets on the electrodes is indicative of melt contact with the front side of the electrodes. On this basis, the distribution of

the sintered pellets verified that erosion of the north concrete wall was much more substantial in comparison to the south wall, as indicated by the thermocouple data provided earlier in this section. During removal of the MgO sidewalls, the remnants of the UO_2 pellet liner were collected and weighed. As shown in Table 3-2, over 92 % of the pellets were recovered during this step, with the balance of the material retained as a sintered layer on the back of the electrodes.

Figure 3-16. CCI-1 Crust Lance Hole Through Crust.

(a)

(b)

Figure 3-17. CCI-1 Core Samples From: (a) North Wall, Laterally (+10 cm Elevation), and (b) Basemat, Axially. Core-Concrete Interface is to the Right.

After the MgO sidewalls were removed, the concrete walls and basemat were lifted from between the two banks of tungsten electrodes and set on the test section platform for detailed examinations to better quantify the debris distribution. North and south (non-electrode sidewall) views of the basemat and overlying corium debris are provided in Figure 3-19, while East and West (electrode sidewall) views are shown in Figure 3-20. Conversely, face-on views of the two concrete sidewalls after removal are provided in Figure 3-21, while a closeup of the North wall that experienced the majority of the ablation during the test is provided in Figure 3-22. During this phase of operations, a second core sample was drilled laterally into the North sidewall at the +10 cm elevation to provided additional information on the debris characteristics. A photograph of the core sample recovered from this procedure is shown in Figure 3-17. The corium adjacent to the concrete interface is noted to contain an elevated level of porosity relative to that in the bulk.

Figure 3-18. CCI-1 View After Removal of West MgO Sidewall.

(a) **(b)**

Figure 3-19. CCI-1 Debris Over Basemat: (a) View From North (b) View From South.

A schematic illustration that shows the key elements of the posttest debris configuration that were deduced from the examinations is provided in Figure 3-23. As is evident from the figures, the ablation front for this test appeared to consist of a region where the core oxide had locally

(a) **(b)**

Figure 3-20. CCI-1 Debris Over Basemat: (a) View From East (b) View From West.

(a) **(b)**

Figure 3-21. CCI-1 Concrete Walls: (a) North, and (b) South.

displaced the cement that bonded the aggregate. This region is clearly evident in Figure 3-22 as a ~ 3 cm thick layer that separated the fresh concrete from the overlying oxide. The core material in contact with this ablation boundary consisted of a 10-15 cm thick layer of hard, dense, monolithic oxide that had solidified with very little porosity.

Above the heavy oxide phase was a layer that appeared to be the crust material that formed when the cavity was flooded. It is noteworthy that the crust had not separated from the underlying melt to form an intervening void. (Absence of significant void

Figure 3-22. CCI-1 Close-Up of North Wall.

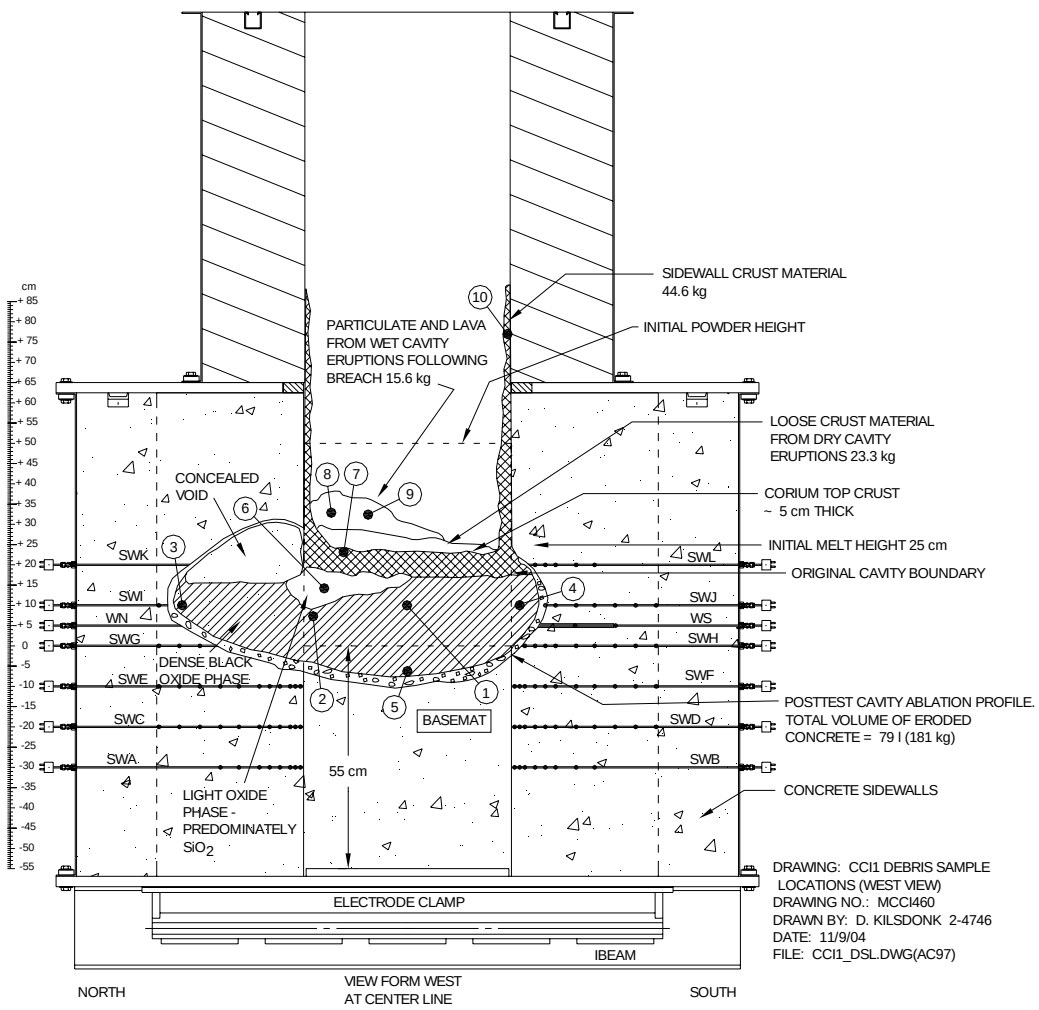

Figure 3-23. Rendering of CCI-1 Posttest Debris Distribution.

formation may have been attributable to early power termination in CCI-1). As shown in Figures 3-19 and 3-20, the crust appeared to be separated from the dense oxide phase by a seam which may have constituted the liquid/solid phase boundary at the time the test was terminated. The average crust thickness was nominally 5 cm, with a variation range of ± 2 cm across the extent of the basemat. This is consistent with crust thicknesses observed in MACE tests.[1-2]

Aside from these major features, adjacent to the North wall was found a light oxide layer that consisted predominately of SiO_2; see Figure 3-22. There was evidence of partially melted pieces of aggregate present in this light oxide layer. This embedded aggregate may have locally been displaced at the ablation interface and then floated up through the heavy oxide where it went into solution with the light oxide phase during the test.

During disassembly, samples were collected from various regions of the debris for elemental analysis by Inductively Coupled Plasma Atomic Emission Spectroscopy (ICP/AES). These analyses were performed by the Analytical Chemistry Lab (ACL) at Argonne.[22] The sample locations are shown in Figure 3-23, while sample descriptions are provided in Table 3-3. All samples were analyzed for key elements present in the initial corium charge (U, Zr, Si, Ca, Mg, Al, Cr), as well as other trace elements or potential impurities (Cu, Fe, Hf, K, Mn, Na, Ni, Sr, Ta, Ti, W, Zn). The elemental results were converted to assumed oxide forms for direct comparison with the initial corium composition. The corresponding mass balance provided a good indication of whether or not the assumed oxide forms were correct. For all samples the mass balances were quite good (100 ± 5 %), indicating that the sample stoichiometry was close to that assumed. Presence of trace elements/impurities was small (<0.1 % per element), with the exception of tungsten, which was as high as 1 wt %. Tungsten originated from dissolution of the electrodes and thermowells during the test.

Table 3-3. Summary of CCI-1 Sample Locations.

Sample	Description/Location	Note(s)
1	Black oxide at +10 cm elevation near lateral centerline of test section.	These samples provide data on the lateral composition variation across the extent of the test section at the elevation where the most lateral ablation occurred.
2	Black oxide near North concrete wall of test section.	
3*	Black oxide at + 10 cm elevation at 33 cm ablation depth into North concrete wall.	
4	Black oxide at + 10 cm elevation at 4 cm ablation depth into South concrete wall.	
5*	Black oxide at – 4 cm elevation near the axial centerline of the test section.	This sample, along with No. 1, provides data on the axial composition variation near the test section centerline.
6	Light oxide phase near North wall.	-
7	Sample from the top crust taken near the North wall.	-
8	From material erupted after crust breach, dark oxide.	-
9	From material erupted after crust breach, green oxide.	-
10	Sidewall crust in the middle test section.	Characterize initial melt composition.

*Taken from core samples recovered from core drillings at these two locations.

As is evident from Figure 3-23, the lateral composition variation across the full extent of the debris near the axial centerline of the material can be determined by comparing the analysis results for Samples 1-4. This comparison is provided in Table 3-4. The reported measurement uncertainty in this data is ± 10% of the value shown for each constituent. For reference, the initial melt composition is provided in Table 3-4, as well as the estimated average debris composition at End of Test (EOT).[a] The data indicates that the material near the center of the test section had higher core oxide content than samples taken near both the north and south concrete walls. Samples taken adjacent to the two opposing concrete walls were virtually identical.

As is evident from Figure 2-23, data regarding the axial composition variation within the heavy oxide phase is provided by comparing Samples 1 and 5; see Table 3-5. This comparison indicates that the axial composition is fairly uniform, at least near the center of the interaction. The analysis results for samples taken at other various debris locations are provided in Table 3-6. From this information, the composition of the light oxide phase near the north wall is noted to be composed of predominately of SiO_2 (i.e., 84 wt %), with the balance being core oxides. The samples taken from the material erupted after crust breach had a composition with slightly higher core oxide content in comparison to the samples taken near the north and south walls. The ejected material may thus have been a mixture of corium from the center of the test section and

Table 3-4. CCI-1 Analysis Results for Samples Taken Across Lateral Extent of Debris at + 10 cm Elevation.

Const.	Wt % Constituent at Sample Location				Initial* Comp. (Wt %)	EOT Comp. (Wt %)
	No. 3: 33 cm deep into North wall	No. 2: near North wall	No. 1: near test section centerline	No. 4: 4 cm deep into South wall		
UO_2	41.25	53.33	47.98	41.61	59.33	40.35
ZrO_2	18.68	18.83	21.01	18.61	24.37	16.58
SiO_2	30.90	20.77	22.57	30.37	6.22	32.81
MgO	0.63	0.46	0.55	0.67	0.07	0.25
Al_2O_3	0.56	0.40	0.50	0.59	0.38	0.52
CaO	4.17	3.05	3.59	4.33	1.22	3.78
Cr_2O_3	3.80	3.17	3.80	3.82	8.41	5.71

*Assumes Cr metal is fully oxidized for direct comparison with ICP/AES results.

[a]The EOT composition for CCI-1 was determined by reducing the initial 400 kg melt mass (see Table 2-4) by the sidewall crust mass of 44.6 kg measured during disassembly (see Table 3-2), and then adding in the estimated slag mass eroded into the melt over the course of the test. As shown in Figure 3-23, ~79 liters of concrete were eroded during the test, which amounts to 181 kg given the initial concrete density (Table 2-2). The slag mass of 172.6 kg was then deduced from the eroded concrete mass after removing the CO_2 and H_2O decompositions gases (4.63 wt % from Table 2-1) that were released during ablation. The slag was then proportioned into the principal oxide components (SiO_2, CaO, Al_2O_3, and MgO) according to relative ratios for this concrete type (see Table 2-2).

Table 3-5. CCI-1 Analysis Results for Samples Taken At Two Axial Elevations Near the Test Section Centerline.

Const.	Wt % Constituent at Sample Location		Initial* Comp. (Wt %)	EOT Comp. (Wt%)
	No. 1: +10 cm Elevation	No. 5: - 3 cm Elevation		
UO_2	47.98	52.11	59.33	40.35
ZrO_2	21.01	20.09	24.37	16.58
SiO_2	22.57	20.37	6.22	32.81
MgO	0.55	0.49	0.07	0.25
Al_2O_3	0.50	0.42	0.38	0.52
CaO	3.59	2.85	1.22	3.78
Cr_2O_3	3.80	3.68	8.41	5.71

*Assumes Cr metal is fully oxidized for direct comparison with ICP/AES results.

Table 3-6. CCI-1 Analysis Results for Samples Taken at Other Debris Locations.

Const.	Wt % Constituent at Sample Location					Initial* Comp. (Wt %)	EOT Comp. (Wt%)
	No. 6: Light oxide near North wall	No. 7: top crust near North wall	No. 8: Post-breach eruption, dark oxide	No. 9: Post-breach eruption, green oxide	No. 10: Middle section sidewall		
UO_2	9.69	52.13	45.12	44.25	56.84	59.33	40.35
ZrO_2	4.01	22.18	19.10	18.73	23.83	24.37	16.58
SiO_2	83.41	18.27	27.09	28.34	10.43	6.22	32.81
MgO	0.17	0.64	0.63	0.62	0.35	0.07	0.25
Al_2O_3	0.18	0.50	0.54	0.55	3.12	0.38	0.52
CaO	1.15	2.85	4.03	3.98	2.54	1.22	3.78
Cr_2O_3	1.39	3.43	3.50	3.54	2.90	8.41	5.71

*Assumes Cr metal is fully oxidized for direct comparison with ICP/AES results.

near the north wall. Finally, the sample taken from the sidewall crust material above the solidified debris is very similar to the initial melt composition, indicating that this material was deposited during the thermite burn and should be subtracted from the initial melt mass of 400 kg for future analyses of this test.

3.2 Test CCI-2 Results

As shown in Table 1-1, Test CCI-2 investigated the interaction of a fully oxidized Pressurized Water Reactor (PWR) core melt, initially containing 8 wt % Limestone/Common Sand (LCS) concrete, with a two-dimensional LCS concrete test section (see Section 2.1 for a design description). For reference, the initial melt composition is provided in Table 2-4. Target input power during dry cavity operation was specified as 120 kW. The planned test operating procedure was detailed in Section 2.11. The actual operating sequence is described below.

Thermalhydraulic Results

Test CCI-2 was performed on August 24, 2004. The event sequence is shown in Table 3-7. Test operations began by applying electrical current to the nichrome wire located near the top of the charge; the burn time was ~37 seconds. Following the reaction, DEH input to the melt was ramped up to the target power of 120 kW. The power trace for the test is shown in Figure 3-24. Time t=0 in the figures that follow again corresponds to the time at which the melt made initial contact with the basemat surface (i.e., at completion of the thermite burn). Target power level was reached at 1.6 minutes, where it was essentially maintained for the balance of the test involving dry cavity operations.

Onset of ablation was detected at all five basemat thermocouple array locations, as well as all six sidewall array locations on the North and South sidewalls initially exposed corium, within the first minute of the interaction. The thermal response of the basemat at the centerline is shown in Figure 3-25, while the north and south concrete wall thermal responses at the +10.0 cm elevation are shown in Figures 3-26 and 3-27, respectively (see Figures 2-6 and 2-20 for schematics showing the thermocouple array locations). The dimensions shown in the legends for these figures indicate the distance of the thermocouple junctions from the concrete inner surfaces. As noted earlier, the sequential rise in the temperatures is indicative of the progression of the ablation front into the concrete. In general, onset of ablation at a given location corresponds to the local temperature reaching the LCS concrete liquidus temperature of 1295 °C.[23]

Soon after the interaction began, aerosols within the test section plenum cleared to the point that the melt surface could be seen with the lid video camera. This view revealed the presence of a stable crust at the melt upper surface. As the dry phase of test operations progressed, this crust periodically melted and reformed. A total of 21 discrete melt eruptions occurred through vent holes in the crust that

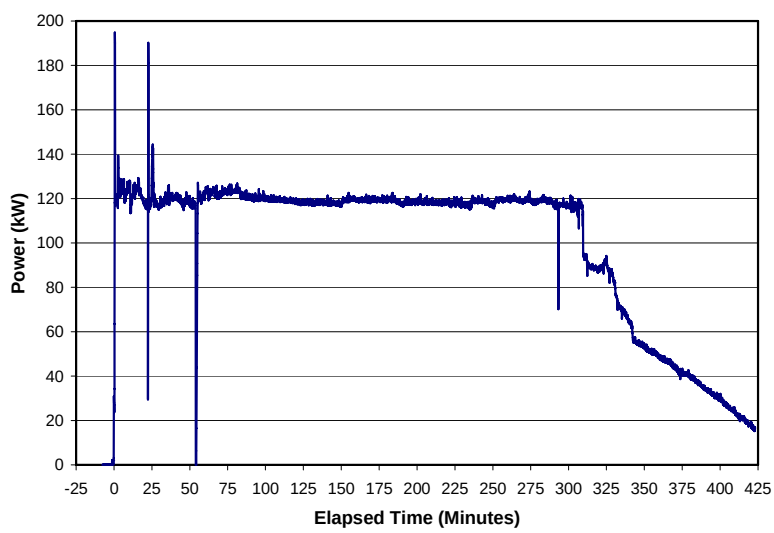

Figure 3-24. CCI-2 DEH Input Power.

Table 3-7. CCI-2 Event Sequence.

Time (Minutes)	Event
-0.6	Thermite burn initiated.
0.0	Melt generation completed; initial temperature ~1880 °C
0.4	Onset of basemat ablation detected at all thermocouple locations, and at 0.0, +10.0, and +20.0 cm elevations on both the North and South sidewalls.
1.2	Aerosol clears in test section plenum revealing crusted melt upper surface.
1.6	Target input power of 120 kW reached.
5.0-23.0	Quiescent period; melt temperature falls to ~1800 °C at 5.0 minutes before stabilizing and then gradually increasing back to ~1910 °C.
23.0-55.0	Average melt temperature peaks at the start of the period, and then steadily declines to ~1800 °C at the end of the period.
34.9 - 38.4	Melt eruption near North sidewall; aerosols gradually block view. Ablation burst detected at + 10 cm elevation on North sidewall. Local ablation depth proceeds from 2.5 to 7.6 cm; average ablation rate = 1.6 cm/min.
42.7 - 43.6	Aerosols gradually clear, melt churning is still evident. Large crust mantles evident on East and West walls. View is eventually blocked by aerosols.
42.2 - 52.8	Axial ablation picks up dramatically, proceeding from 2.5 to 7.6 cm; average ablation rate =0.5 cm/min.
62.7 - 85.7	Intermittent eruptions through holes in crust near Northeast corner.
146.8 -155.0	Eruptions through holes in crust in Southwest corner.
165.4, 169.3	Large volume, short duration lava flows occur near South wall.
177.4 - 189.3	Intermittent eruptions near south wall. Eventually a large hole develops through the crust near the centerline.
195.7 - 199.6	Minor intermittent eruptions through Southwest crust opening.
202.4 - 229.8	Intermittent eruptions through vent hole in Southwest corner. Additional hole develops near South wall centerline but this hole eventually closes.
266.8 - 278.6	Intermittent eruptions through opening that gradually grows towards centerline. At culmination, hole in crust is present in Southeast corner.
284.8 - 289.2	Intermittent eruption activity through crust opening in Southeast corner.
298.9	Crust lance probe inserted in an attempt to breach the bridge crust. Peak load of ~4.84 kN applied. Crust was not breached.
300.8	Water addition initiated on the basis of reaching the 29.2 cm depth in North sidewall at +10.0 cm elevation; melt temperature ~1540 ºC. Cooling rate reaches 2.8 MW/m^2.
325.8- 332.2	Intermittent eruptions observed below the bridge crust, as evidenced by luminescence through crust opening in the Southeast corner.
346.0	Crust lance used in an attempt to breach the bridge crust. Peak load of 3.35 kN applied. Crust was not breached.
423.1	Test terminated on the basis that concrete temperatures had stabilized. Power supply operations and data acquisition terminated

formed at various locations. Several of these eruptions were extensive, the longest of which lasted more than 10 minutes.

As described in Section 2.10, a total of seven multi-junction Type C thermocouple arrays were used to monitor melt temperatures at various axial and lateral locations. Data from two of the axially configured arrays located in the basemat are shown in Figure 3-28, while data from the laterally configured arrays located in the North and South sidewalls at the +5.0 cm elevation are shown in Figures 3-29 and 3-30, respectively. Finally, data from all melt temperature

thermocouples that contacted corium over the course of the test are shown collectively in Figure 3-31 for comparative purposes. Dimensions in the legends again refer to junction elevations with respect to the concrete surfaces. Data from the experiment[15] indicates that the initial melt temperature following the thermite reaction was ~ 1880 ºC, but the temperature fell rapidly to ~1800 °C within the first 5 minutes of the test due to heat transfer to the cold concrete surfaces.

Examination of the data in Figure 3-31 indicates that although there were fluctuations, the melt temperature was relatively constant in the range of 1800-1900 °C during the first 30 minutes of the interaction. This trend is consistent with the formation of insulating crusts on the cold concrete surfaces following initial contact with melt. After this initial phase, the data in Figure 3-31 indicates that: i) the average melt temperature declined steadily from ~1900 °C to ~1550 °C during dry cavity operations, and ii) no large lateral or axial temperature gradients developed in the melt pool during the interaction. Note that the latter observation is not applicable at the pool upper surface, where the sustained presence of the crust is indicative of a large temperature gradient at that boundary.

The progression of the axial ablation front location during the course of the test is shown in Figure 3-32, while the analogous set of data for the north and south concrete sidewalls are provided in Figures 3-33 and 3-34, respectively. Finally, the maximum erosion rate measured on each concrete surface is shown in Figure 3-35. This collection of data indicates

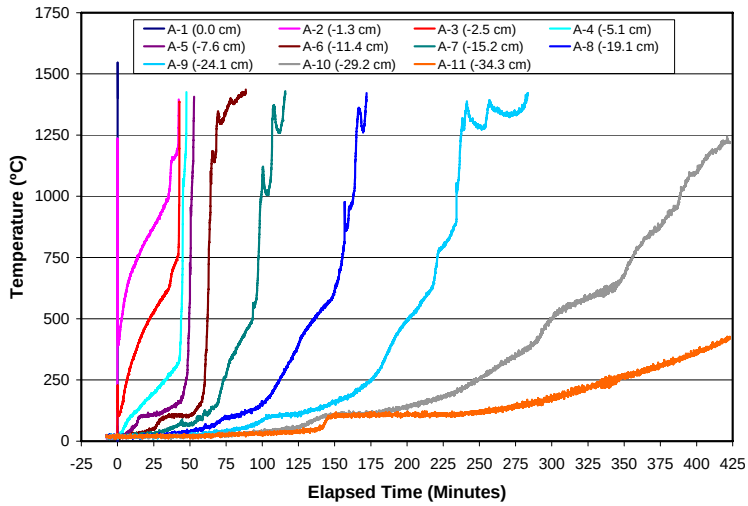

Figure 3-25. CCI-2 Basemat Heatup Near Centerline.

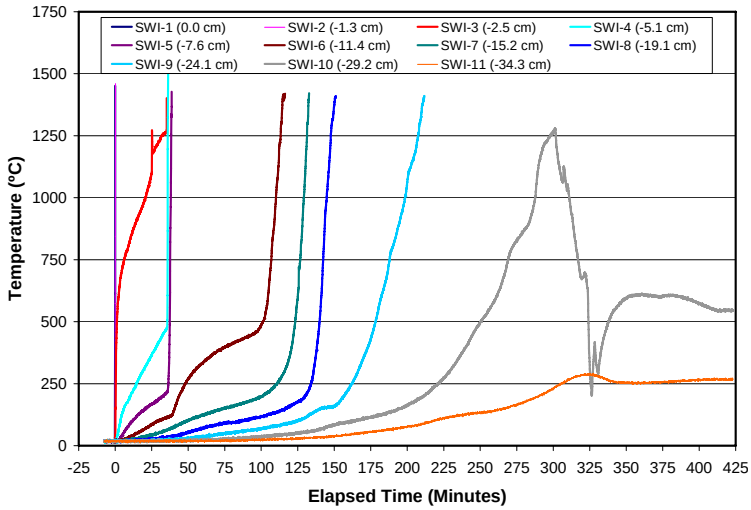

Figure 3-26. CCI-2 North Wall Heatup (+10 cm).

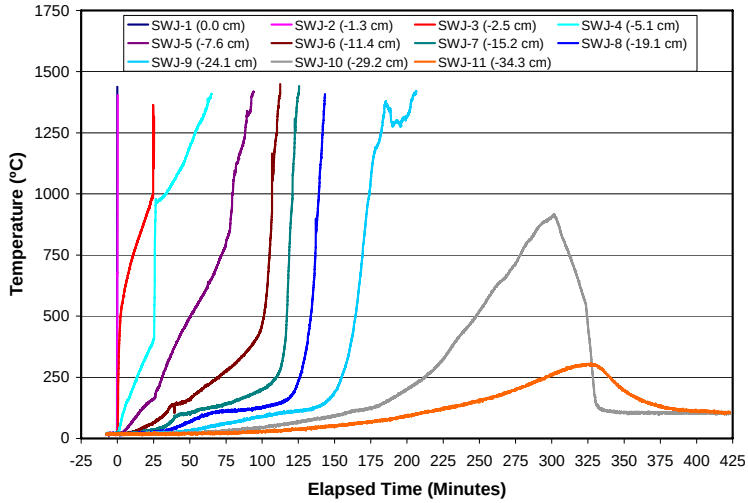

Figure 3-27. CCI-2 South Wall Heatup (+10 cm).

that over the first 30 minutes of the interaction, ablation proceeded very slowly in both the lateral and axial directions. During this time, the concrete surfaces were most likely protected by insulating crusts that formed following initial melt formation. After ~30 minutes of sustained heating, the data in Figure 3-35 indicates that these surface crusts either failed, or they thinned to the point where they no longer provided a significant heat transfer impediment. In either case, ablation then began in earnest, and the core-concrete interaction progressed steadily in both the lateral and axial directions until the point at which the cavity was flooded. Unlike Test CCI-1, no large spatial incoherence in the ablation progression was observed.

After 300 minutes of dry cavity operations, the criterion for flooding the cavity was reached on the basis of reaching the 30 cm ablation depth in the North concrete wall at the +10.0 cm elevation (see Figure 3-26). As shown in Table 3-7, the lance was inserted in an attempt to breach the crust prior to water addition, but this attempt was not successful, despite reaching the peak lance load capacity of ~4.8 kN. As discussed in the next section on posttest examinations, a large mantle of frozen material had formed on the sidewalls in the upper region of the test section over the previous 5 hours of dry cavity operations. The lance contacted, and was not able to dislodge, this sidewall material. However, this mantle did not prevent the water from contacting the underlying melt during the subsequent cavity flooding stage.

Following the attempt to breach the crust, the cavity was

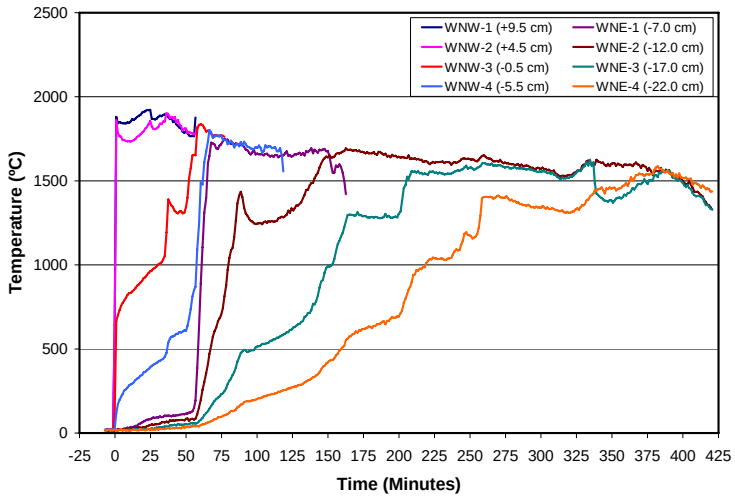

Figure 3-28. CCI-2 Melt Temperatures Near Centerline.

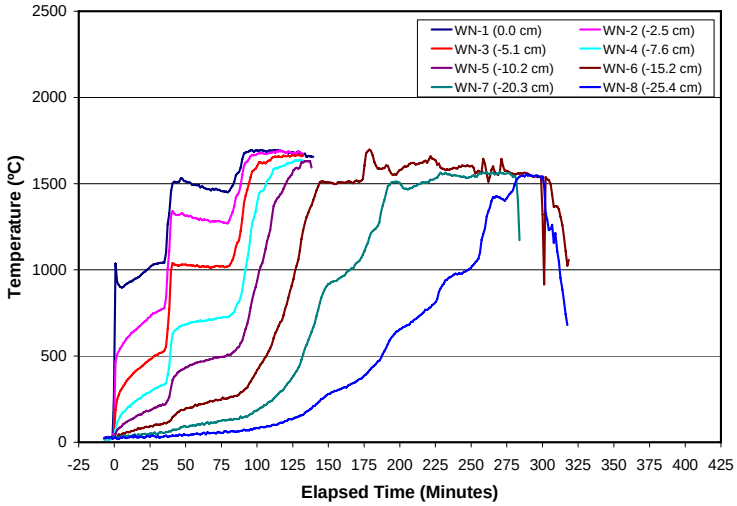

Figure 3-29. CCI-2 Melt Temperatures Near the North Wall (+5 cm Elevation).

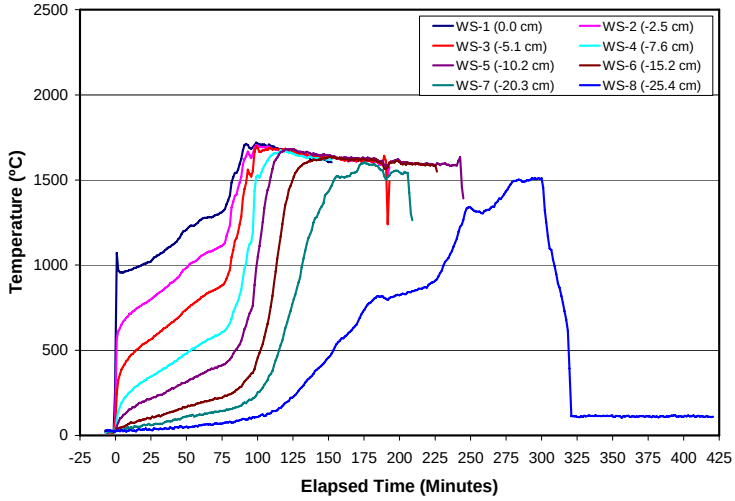

Figure 3-30. CCI-2 Melt Temperatures Near the South Wall (+5 cm Elevation).

flooded with ~ 125 liters of water to bring the water level over the melt to ~ 50 cm. After this time, liquid lost to evaporation was periodically replaced to maintain the water level over the melt roughly in the range of 50 ± 5 cm per the test procedure.

The debris-water heat flux, calculated on the basis of the steam formation rate normalized by the estimated crust planar surface area in contact with the coolant of 0.5 m^2 (see next section), is shown in Figure 3-36. The peak debris cooling rate reached ~ 2.8 MW/m^2 during the initial flooding stage. Following cavity flooding, power supply operation was switched from constant power to a constant voltage mode per the normal test operating procedure. As shown in Figure 3-24, the input power fell precipitously while operating at constant voltage, which is consistent with substantial heat removal and debris solidification. During this time interval, two significant melt eruptions occurred, as evidenced by luminescence observed through the overlying water layer. However, the extent of heat flux augmentation due to these eruptions could not be quantified since the quench system tanks had reached saturation as a result of the large overall debris cooling rate.[15] As is evident from Figure 3-36, the average heat flux remained well above 500 kW/m^2 for the first 30 minutes of the cooling transient.

As specified in the test procedure, the crust lance was inserted ~ 45 minutes after cavity flooding in an attempt to breach the crust and thereby obtain data on the transient crust breach cooling

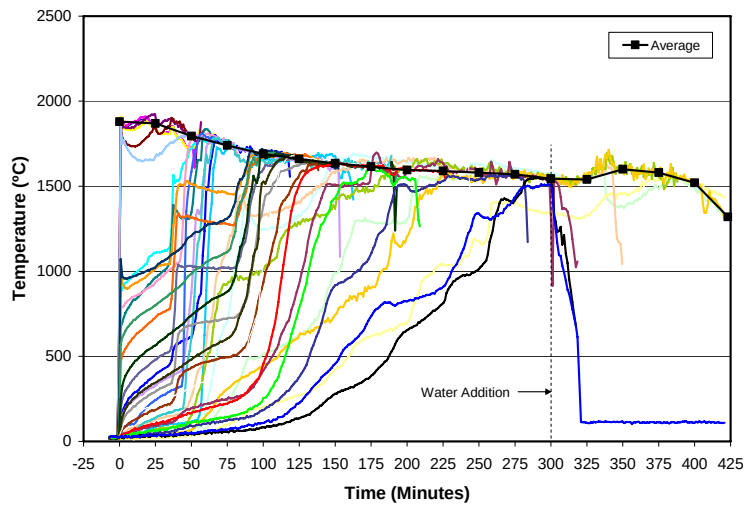

Figure 3-31. Collection of CCI-2 Melt Temperatures.

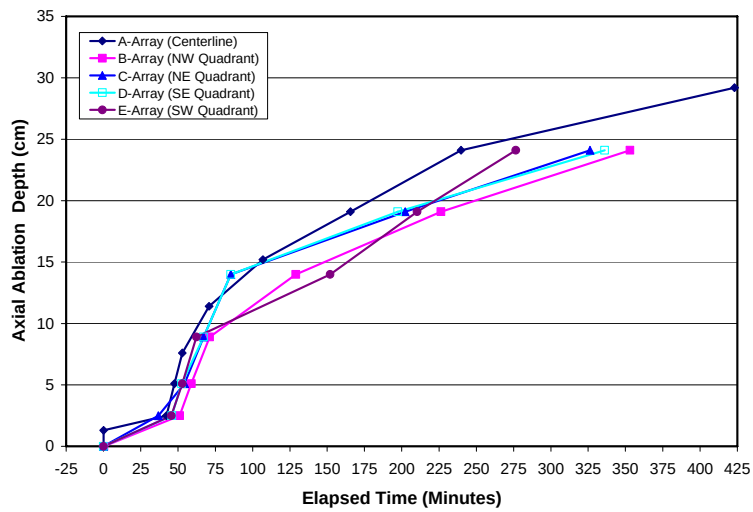

Figure 3-32. CCI-2 Axial Ablation.

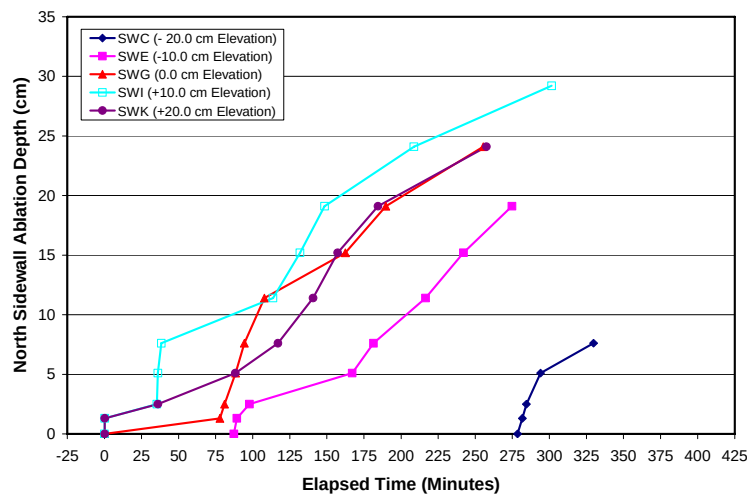

Figure 3-33. CCI-2 North Sidewall Ablation.

mechanism. However, this attempt was not successful, despite delivering a peak load of 3.35 kN. As noted above, a mantle of frozen material had formed on the sidewalls above the melt during dry cavity operations. The lance recontacted, and again was not able to dislodge, this sidewall material, thereby prohibiting contact with the underlying crust material formed at the melt/water interface. Thus, the objective of obtaining data on the transient crust breach cooling mechanism was not obtained as part of this experiment.

After the lance insertion sequence, the input power continued to fall while the heat removal rate from the debris remained significant. As shown in Figures 3-29 through 3-31, several surviving melt temperature thermocouples indicated local debris quench to the water saturation temperature. In addition, virtually all concrete thermocouples indicated that local concrete temperatures had stabilized, and at several locations, the concrete had been cooled to water saturation temperature (e.g., see Figure 3-27). On this basis, the test was terminated at 423 minutes, or ~ 2 hours after cavity flooding, on the basis that the input power had fallen below ~ 15 % of the initial value, and concrete erosion had essentially been terminated.

In general, this test exhibited a high rate of cooling in comparison to previous one-dimensional MACE tests conducted with LCS concrete.[1-2] One mechanism that was clearly active in CCI-2 was that water was able to penetrate the interface between the corium and concrete sidewalls, thereby augmenting the overall debris cooling rate. This same mechanism was also

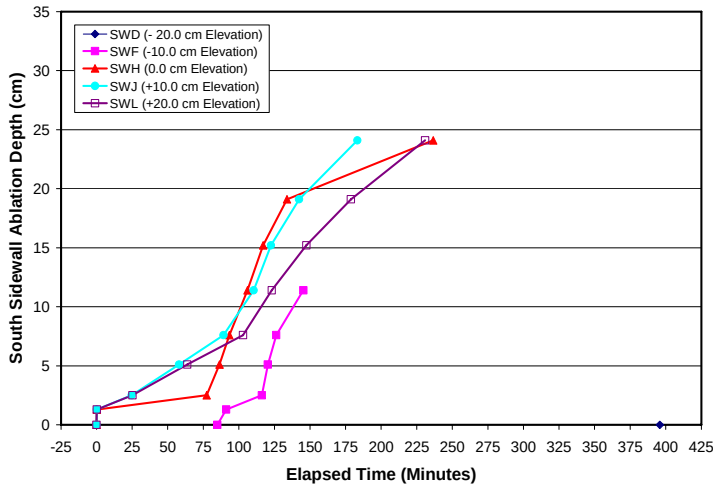

Figure 3-34. CCI-2 South Sidewall Ablation.

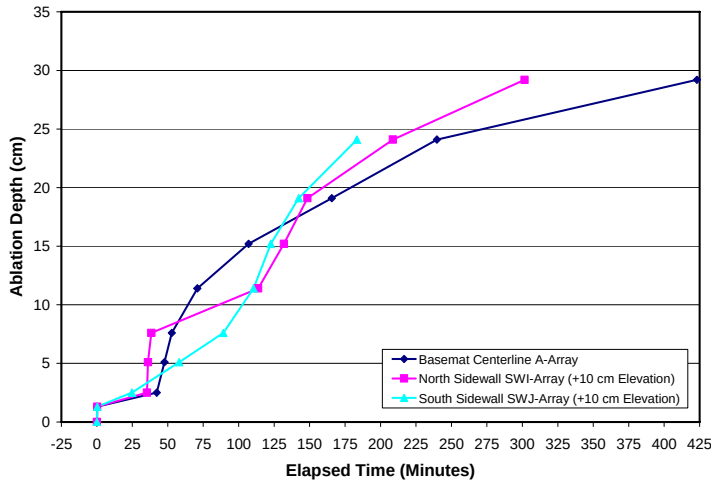

Figure 3-35. CCI-2 Peak Axial and Lateral Ablation Data.

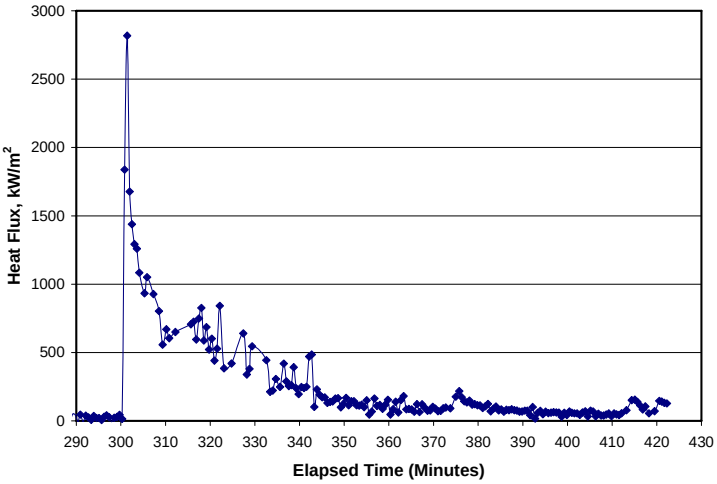

Figure 3-36. CCI-2 Melt-Water Heat Flux.

observed in the COTELS reactor material tests, which investigated 2-D core-concrete interaction and debris coolability, albeit at very high specific power density relative to CCI-2 (Nagasaka *et al.*[11]). However, this additional cooling mechanism was not observed in MACE test M1b, which was conducted with inert refractory (MgO) sidewalls (see Farmer *et al.*[1]).

Posttest Examination Results

As described in Section 2.11, the apparatus was carefully disassembled following the test in order to characterize the posttest debris configuration. Figure 3-37 provides a picture of the top surface of the large mantle crust that formed in the upper region of the test section after removal of the middle sidewall section, along with a sketch of the surface showing key elevations and features. A large opening through the bridge crust was apparent in the southeast corner of the test section. The characteristic dimensions of this opening were 6 cm by 9 cm. Visual examination through the opening revealed the presence of a large void region beneath the crust. The lid video camera view of the corium surface clearly indicated that this hole provided the pathway for water to flood the underlying melt during the test. The crust upper surface elevations measured with the lance probe both prior to and after cavity flooding[15] are consistent with the posttest surface elevations, indicating that the crust had not moved significantly during at least the last two hours of the experiment. In addition, video footage taken prior to cavity flooding indicated that the two-phase melt (voided) height periodically bridged this large gap, as evidenced by melt eruptions and lava flows occurring through this (and other) openings in the crust.

After key features of the bridge crust were documented, the crust was removed to gain access to the underlying void region. As shown in Figures 3-38 and 3-39, removal of this material revealed the presence of large mantles of crust protruding from both the east and west

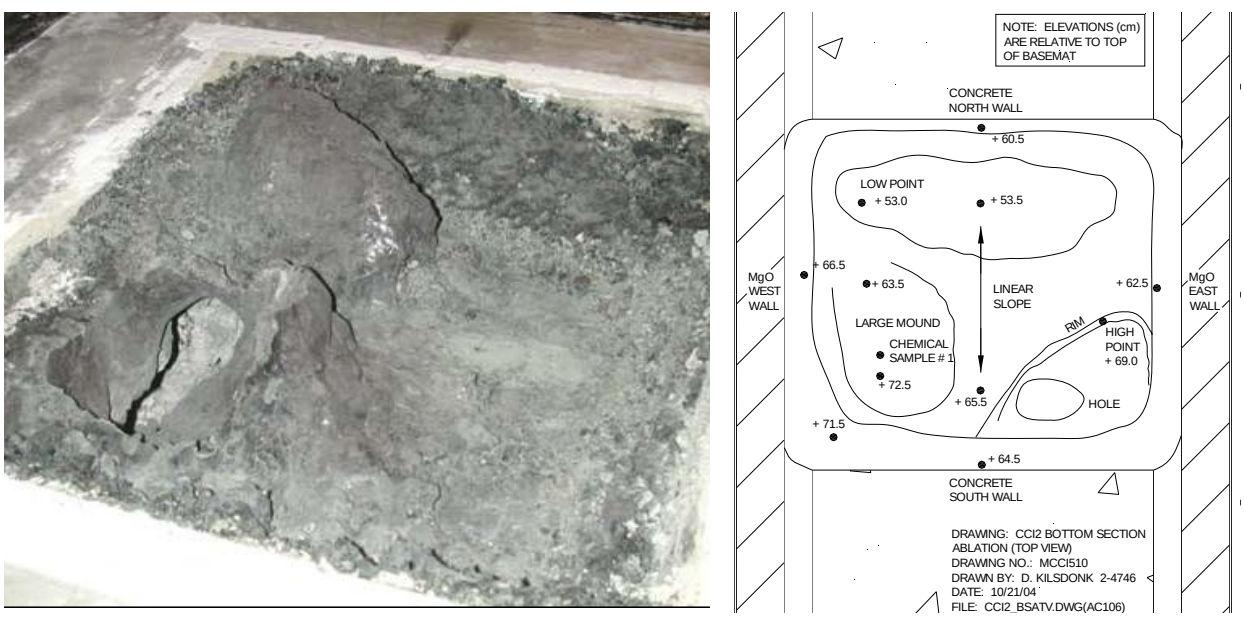

(a) **(b)**

Figure 3-37. (a) Top View of CCI-2 Bridge Crust, and (b) Schematic Detailing Key Features.

MgO sidewalls. Video data indicates that these mantles started forming as early as 42 minutes into the test sequence (see Table 3-7). For reference, the masses of various debris regions recovered during disassembly are provided in Table 3-8. As shown in the table, the total mass of this mantle material was quite large, amounting to 301.4 kg.

With these steps completed, the MgO sidewalls were removed to provide access for gaining additional information regarding the debris morphology and overall shape of the cavity erosion profile. A photograph showing the bank of tungsten electrodes after removal of the west sidewall of the test section is provided in Figure 3-40. As noted earlier, sintering of the crushed UO_2 pellets on the electrodes is indicative of melt contact with the front surface of the electrodes. On this basis, the distribution of the sintered pellets verified that the cavity erosion for CCI-2 was fairly symmetrical, as indicated by the thermocouple data that was described earlier in this section. During removal of the MgO sidewalls, the remnants of the UO_2 pellet liner were collected and weighed. As shown in Table 3-2, over 87 % of the pellets were recovered during this step, with the balance of the material retained as a sintered layer on the backs of the two electrode banks.

Figure 3-38. CCI-2 Crust Mantle Adhering to East Sidewall (after removal of bridge crust).

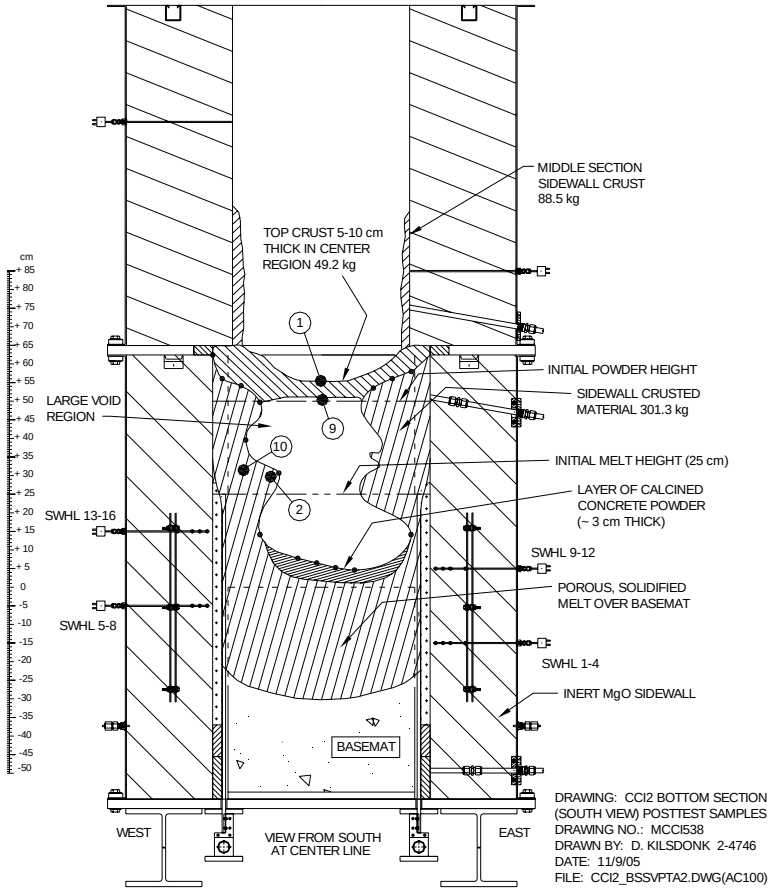

Figure 3-39. Rendering of CCI-2 Posttest Debris (Non-Electrode Sidewall View).

Table 3-8. Masses of Material Regions Measured During Disassembly for CCI-2.

Material Description	Mass (kg)	Notes(s)
Mass of Corium Recovered from Middle Section Sidewalls	88.5	-
Bridge Crust Mass in Central Region of Test Section	49.2	-
Sidewall Crust Mantles on East and West Walls	301.4	-
Recovered UO_2 pellets	295.4	A total of 338.6 kg pellets were loaded behind the electrodes. The balance of the material (43.2 kg) was left as a sintered layer on the back of the electrodes.

Two photographs that provide an overall perspective of the cavity erosion profile and the solidified debris upper surface characteristics are provided in Figure 3-41. As is evident from these pictures, cavity erosion above the solidified debris was extensive. This erosion was probably driven by radiation heat transfer from the melt surface during periods in which the melt pool was collapsed, and also by convective heat transfer directly from the melt pool when the pool was undergoing extensive voiding. One significant finding during this

Figure 3-40. CCI-2 View After Removal of West MgO Sidewall.

(a) **(b)**

Figure 3-41. CCI-2 Solidified Corium; Views from (a) Southeast, and (b) Northwest.

stage of the disassembly was the presence of a large mound of erupted material near the North concrete sidewall; see the view from the Southeast in Figure 3-41. This was most likely the material that was ejected during the melt eruptions that occurred after cavity flooding; see Table 3-7. The estimated volume of this material was 22 liters. A vent opening which was apparently the source of the eruptions was discovered approximately 10 cm from the eroded North concrete sidewall near the East-West centerline of the test section. The diameter of the vent hole was ~ 1 cm.

Figure 3-42. Photograph of Core Sample Opening Through CCI-2 Crust.

Prior to removal of the concrete sidewalls, an axial core sample was drilled into the corium over the basemat near the test section centerline. A photograph of the hole created in the corium by the drilling process is shown in Figure 3-42, while a photograph of the core sample that was recovered from this procedure is provided Figure 3-43. The core sample was used to collect specimens for chemical analysis; this data is provided later in the section. Limited examination of the corium through the core hole at this stage indicated the presence of significant porosity, but no continuous void region that would be expected if a second bridge crust had formed during the test.

Figure 3-43. CCI-2 Axial Core Sample.

After the core sample was collected, the concrete walls and basemat were lifted from between the two banks of tungsten electrodes and set on the test section platform for detailed examinations to better quantify the debris distribution. North and south (non-electrode sidewall) views of the basemat and overlying corium are provided in Figure 3-44. Conversely, face-on views of the two concrete sidewalls after removal are provided in Figure 3-45. Visual examinations during this stage indicated that the corium remaining over the basemat was very porous, with pore sizes of several cm clearly evident. In fact, the porosity was so significant that one could see completely through the debris in the North-South direction. This

(a) **(b)**

Figure 3-44. CCI-2 Debris Over Basemat: (a) View From North (b) View From South.

(a) **(b)**

Figure 3-45. CCI-2 Solidified Corium and Concrete Sidewalls; Views from (a) Southeast, and (b) Northwest.

level of porosity is consistent with the high rate of corium cooling observed when the cavity was flooded at 300 minutes during the test sequence (see Table 3-7). However, as for test CCI-1, no continuous void was discovered beneath the crust upper surface, which indicates that the crust had not anchored to the test section sidewalls, as typically occurred in MACE integral effect tests.[1-2]

An illustration that shows the key elements of the posttest debris configuration that were deduced from the above examinations is provided in Figure 3-46. As is evident from the figure, the examinations confirmed the fairly symmetrical lateral-axial ablation behavior for this particular experiment.

During disassembly, samples were collected from various regions of the debris for elemental analysis.[22] The sample locations are shown in Figures 3-39 and 3-46, while sample descriptions are provided in Table 3-9. As described previously, all samples were analyzed for the key elements present in the initial corium charge (U, Zr, Si, Ca, Mg, Al, Cr), as well as other trace elements or potential impurities. The elemental results were converted to assumed oxide forms for direct comparison with the initial corium composition. The corresponding mass balance provides a good indication of whether or not the assumed oxide forms are correct. For all samples the mass balances were reasonably good (100 ± 10 %), indicating that the sample stoichiometry is close to that assumed. Presence of trace elements/impurities was small (< 0.1 % per element), with the exception of tungsten, which was as high as 1.37 wt %. Tungsten originated from dissolution of the electrodes and thermowells during the test.

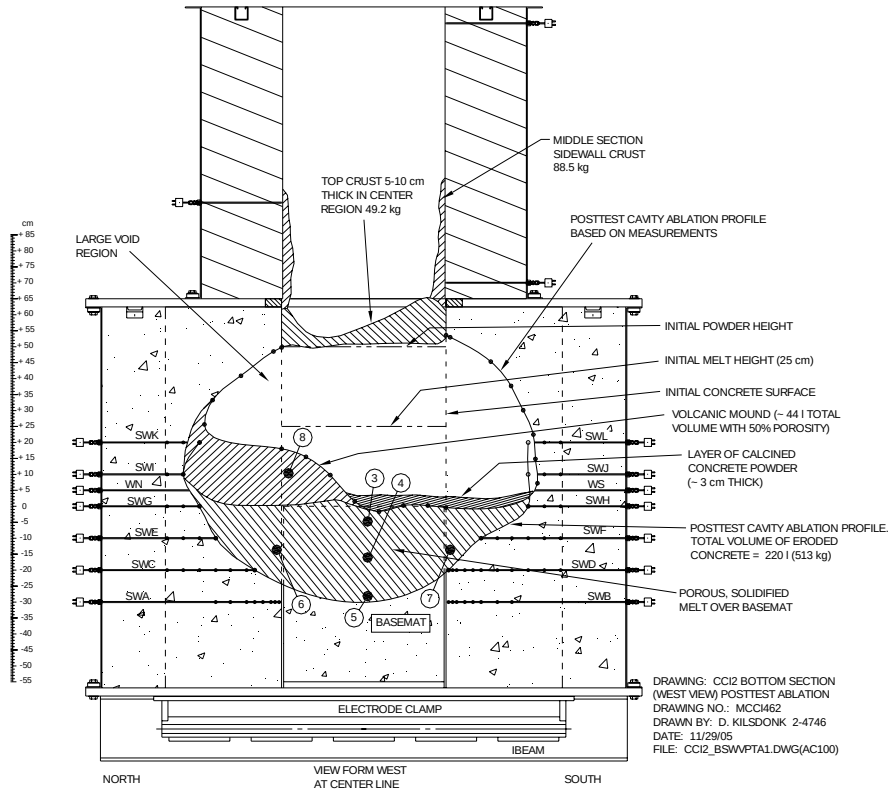

Figure 3-46. Rendering of CCI-2 Posttest Debris Configuration.

As is evident from Figure 3-46, the lateral composition variation across the full extent of the debris near the axial centerline of the material can be determined by comparing the analysis results for Samples 4, 6, and 7. This comparison is provided in Table 3-10. The reported measurement uncertainty in this data is ± 10% of the value shown for each constituent. For reference, the initial melt composition is provided in Table 3-10, as well as the estimated average debris composition at End of Test (EOT).[b] In general, the compositions of the three samples cluster around the EOT composition. The compositions of the two samples taken adjacent to the

[b]The EOT composition for CCI-2 was determined by reducing the initial 400 kg melt mass (see Table 2-4) by the sidewall crust mass of 88.5 kg measured during disassembly (see Table 3-8), and then adding in the estimated slag mass eroded into the melt over the course of the test. As shown in Figure 3-46, ~220 liters of concrete were eroded during the test, which amounts to 513 kg given the initial concrete density (Table 2-2). The slag mass of 338.1 kg was then deduced from the eroded concrete mass after removing the CO_2 and H_2O decompositions gases (34.1 wt % from Table 2-1) that were released during ablation. The slag was then proportioned into the principal oxide components (SiO_2, CaO, Al_2O_3, and MgO) according to relative ratios for this concrete type (see Table 2-2).

Table 3-9. Summary of CCI-2 Sample Locations.

Sample	Description/Location	Note(s)
1	Top crust near upper surface	This sample, along with No. 9, provides data on the formation time of the upper bridge crust.
2	Outer surface of mantle crust facing the interaction zone	-
3*	Upper 1/3 of solidified corium near test section centerline	These samples provide data on the axial composition variation near the centerline of the test section.
4*	Middle 1/3 of solidified corium near test section centerline	
5*	Bottom 1/3 of solidified corium near test section centerline	
6	North concrete sidewall near the axial centerline of the solidified corium	These two samples, along with No. 4, provide data on the lateral composition variation across the extent of the test section.
7	South concrete sidewall near the axial centerline of the solidified corium	
8	Near center of volcanic mound adjacent to North concrete sidewall	-
9	Top crust near bottom surface	-
10	Mantle crust ~ 5 cm from the surface facing the interaction zone.	This sample, along with No. 2, provides data on the formation time of the mantle crust.

*Taken from core sample recovered from core drilling at the test section centerline.

Table 3-10. CCI-2 Analysis Results for Samples Taken Across Lateral Extent of the Debris Near the Debris Axial Centerline.

Const.	Wt % Constituent at Sample Location			Initial* Comp. (Wt %)	EOT Comp. (Wt %)
	No. 6: Near North Wall	No. 4: Centerline	No. 7: Near South Wall		
UO_2	23.79	34.63	21.53	58.88	28.65
ZrO_2	8.82	12.63	8.34	24.18	11.78
SiO_2	22.06	15.11	23.48	3.29	19.68
CaO	27.20	20.74	27.94	3.04	23.08
MgO	12.71	9.82	13.10	1.11	10.14
Al_2O_3	2.86	2.16	2.89	0.40	2.25
Cr_2O_3	2.56	4.91	2.72	9.10	4.42

*Assumes Cr metal is fully oxidized for direct comparison with ICP/AES results.

North and South concrete walls were virtually indistinguishable. However, the sample taken near the center of the test section had ~ 50 % higher level of core oxides in comparison to the samples taken adjacent to the walls.

As is evident from Figure 3-46, data regarding the axial composition variation within the heavy oxide phase is provided by comparing Samples 3-5. This comparison is provided in Table 3-11. The compositions of these three samples also cluster around the EOT composition. The core oxide content in the samples from the middle and bottom third are quite similar. However, these samples contain ~ 60 % higher core oxide content in comparison to the sample located in the top third of the solidified corium.

Table 3-11. CCI-2 Analysis Results for Samples Taken At Three Axial Elevations Near the Test Section Centerline.

Const.	Wt % Constituent at Sample Location			Initial* Comp. (Wt %)	EOT Comp. (Wt %)
	No. 3: Upper 1/3 of Corium	No. 4: Middle 1/3 of Corium	No. 5: Bottom 1/3 of Corium		
UO_2	20.34	34.63	36.85	58.88	28.65
ZrO_2	8.09	12.63	13.06	24.18	11.78
SiO_2	23.83	15.11	13.76	3.29	19.68
CaO	28.98	20.74	20.99	3.04	23.08
MgO	13.52	9.82	9.54	1.11	10.14
Al_2O_3	3.05	2.16	1.87	0.40	2.25
Cr_2O_3	2.19	4.91	3.93	9.10	4.42

*Assumes Cr metal is fully oxidized for direct comparison with ICP/AES results.

Table 3-12. CCI-2 Analysis Results for Samples Taken at Other Debris Locations.

Const.	Wt % Constituent at Sample Location					Initial* Comp. (Wt %)	EOT Comp. (Wt%)
	No. 1: Top Crust upper surface	No. 9: Top Crust bottom surface	No. 2: Mantle outer surface	No. 10: Mantle 5 cm from surface	No. 8: Volcanic mound		
UO_2	19.94	19.11	22.24	21.58	20.37	58.88	28.65
ZrO_2	8.18	7.72	9.14	8.83	8.08	24.18	11.78
SiO_2	23.33	24.95	23.24	22.09	24.68	3.29	19.68
CaO	28.50	28.71	26.66	26.00	28.49	3.04	23.08
MgO	13.75	13.57	12.64	13.05	13.32	1.11	10.14
Al_2O_3	3.21	3.15	2.94	3.19	3.05	0.40	2.25
Cr_2O_3	3.09	2.79	3.14	5.26	2.01	9.10	4.42

*Assumes Cr metal is fully oxidized for direct comparison with ICP/AES results.

The analysis results for samples taken at other various debris locations are provided in Table 3-12. From this information, it is clear that the composition of the top crust and mantle regions were fairly homogeneous and composed predominately of concrete oxides (50-60%). This finding is consistent with the test interpretation; i.e., the melt pool was well-formed by the thermite reaction, and the top crust and mantle regions formed gradually as the test progressed due to high corium voiding (or 'foaming') during the later phases of the experimental sequence.

Finally, the composition of the material in the volcanic mound was quite similar to that in the top crust and mantle regions, and is further noted to be virtually identical to the composition of the top 1/3 of the solidified corium over the basemat (see Table 3-11). This data thus indicates that the source of the material driving the melt eruption and mantle growth processes was (logically) the top of the melt pool. Furthermore, the data suggests that the core oxide distributions inferred above from Tables 3-10 and 3-11 were present during the test, as opposed to developing after the test was terminated due to density-driven stratification.

3.3 Test CCI-3 Results

As shown in Table 1-1, Test CCI-3 investigated the interaction of a fully oxidized Pressurized Water Reactor (PWR) core melt, initially containing 15 wt % siliceous concrete, with a specially designed two-dimensional siliceous concrete test section (see Section 2.1 for a design description). The siliceous concrete for this test was of European origin (supplied by CEA); the composition is shown in Table 2-1. For reference, the initial melt composition is provided in Table 2-4. Target input power during dry cavity operation was specified as 120 kW. The planned test operating procedure was detailed in Section 2.11. The actual operating sequence is described below.

Thermalhydraulic Results

Test CCI-3 was performed on 22 September 2005. The event sequence is shown in Table 3-13. Test operations began by initiating the thermite reaction with the nichrome wire located at the top of the charge; the burn time was ~40 seconds. Following the reaction, DEH input to the melt was ramped up to the target power of 120 kW. The power trace for the test is shown in Figure 3-47. Time t=0 in the figures that follow again corresponds to the time at which the melt made initial contact with the basemat surface (i.e., at completion of the thermite burn). Target power level was reached at 1.6 minutes, where it was essentially maintained for the balance of the test involving dry cavity operations.

Onset of ablation was detected within the first minute of the interaction on the North and South sidewalls initially exposed corium. However, the peak concrete surface temperature at the basemat centerline was limited to ~ 1000°C. Although onset of basemat ablation was briefly detected in the southeastern quadrant at completion of the thermite burn, this localized ablation was not sustained. Rather, onset of ablation across the extent of the basemat was delayed until later in the experimental sequence. The thermal response of the basemat at the centerline is shown in Figure 3-48, while the north and south concrete wall thermal responses at the +10.0 cm elevation are shown in Figures 3-49 and 3-50, respectively (see Figures 2-6 and 2-20 for schematics showing the thermocouple array locations). The dimensions shown in the legends for these figures indicate the distance of the thermocouple junctions from the concrete inner surfaces. The sequential rise in the temperatures is indicative of the progression of the ablation front into the concrete. In general, onset of ablation at a given location corresponds to the local temperature reaching the siliceous concrete liquidus temperature of 1250 °C.[23]

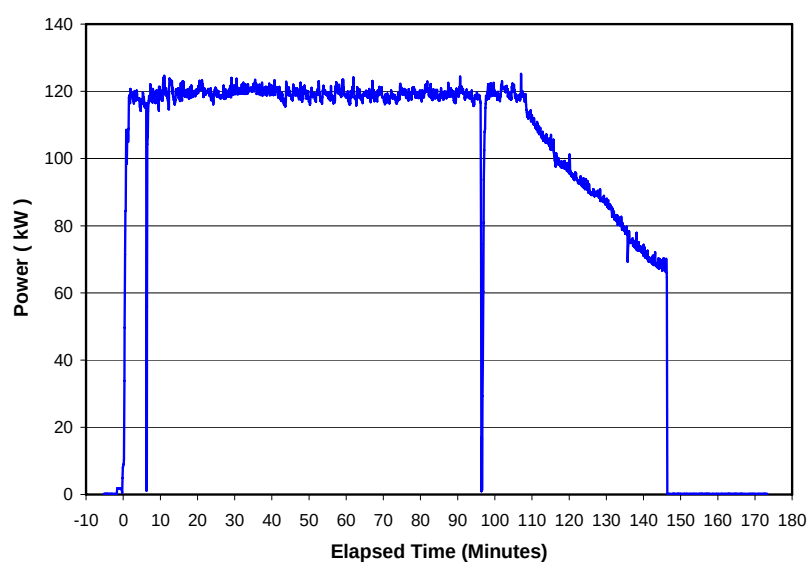

Figure 3-47. CCI-3 DEH Input Power.

Table 3-13. CCI-3 Event Sequence.

Time (Minutes)	Event
-0.7	Thermite burn initiated.
0.0	Melt generation completed; initial temperature ~1950 °C
0.0 - 0.8	Onset of basemat ablation detected in the SE basemat quadrant, and at 0.0, +10.0, +20.0, and +30.0 cm elevations on both concrete sidewalls.
1.6	Target input power of 120 kW reached.
11.0	Melt temperature falls to ~1800 °C; lateral ablation in both concrete walls ~ 7.5 cm; axial ablation < 1 cm.
6.7 - 17.7	Crust surface comes into view; melt eruptions occurring along both concrete walls and near the test section centerline.
45.6	Onset of basemat ablation detected in NW quadrant.
51.4	Onset of sustained basemat ablation detected at all instrument locations.
49.3 - 53.7	Eruptions begin nearly simultaneously near N and S walls. Both ejection and extrusion-type eruptions occur. Eruptions cease at 53.7 minutes.
59.0 - 90.3	Nearly continuous eruptions with predominately extrusion-type eruption processes occurring along both walls and less frequently near the center of the crust. Several eruptions lead to flows that cover 50+ % of the crust surface.
91.4 - 97.5	Major eruptions begin again near S wall. Flows cover ~ 60 % of crust surface. Molten material that flows to the N side apparently melts through crust, causing eruptions to initiate at that location also.
104.7	Crust breached with lance prior to water injection; eruptions through the opening ensue. Crust load force at breach: 1.66 kN; crust elevation: 25.2 cm.
107.6	Sidewall ablation reaches 29.2 cm in South wall at +10.0 cm elevation; water injection initiated; melt temperature ~1650 °C. Initial cooling rate ~ 900 kW/m^2.
140.3	Lance used to breach the crust. Two load peaks observed: the first peak was 0.34 kN at +22.2 cm elevation, while the second was 0.67 kN at +20.0 cm elevation. No noticeable increase in the debris cooling rate.
143.1	Ablation reaches the 34.3 cm limit at the +10.0 cm elevation in the S sidewall.
146.4	Power supply operation terminated.
173.3	Data logging terminated.

At ~ 7 minutes, aerosols within the test section plenum cleared to the point that the melt surface could be seen with the lid video camera. This view revealed that the surface of the melt pool was covered by crust segments that were not rigidly bonded to each other. Melt eruptions were evident along the north and south concrete sidewalls and also near the test section centerline. The crust was present the entire test. As the dry phase of test operations progressed, melt eruptions were periodically observed through this crust.

As described in Section 2.10, a total of seven multi-junction Type C thermocouple arrays were used to monitor melt temperatures at various axial and lateral locations. Data from the axially configured array located at the basemat centerline is shown in Figure 3-51, while data from the laterally configured arrays located in the North and South sidewalls at the +5.0 cm elevation are shown in Figures 3-52 and 3-53, respectively. Finally, data from all melt temperature thermocouples that made contact with melt during the test are shown collectively in Figure 3-54 for comparative purposes. The dimensions in the legends again refer to junction elevations with respect to the concrete surfaces. As is evident from Figure 3-54, the initial melt temperature in the bulk of the pool was ~ 1950 ºC. By 11 minutes into the interaction, the melt

temperature had gradually declined to ~1800 °C. Over the balance of dry cavity operations, the average melt temperature continued to decline, falling to ~ 1650 ˚C at the time the cavity was flooded. During the last 90 minutes of operation with DEH present, melt temperatures were fairly uniform across the extent of the interaction, generally clustering within a band of approximately ± 50˚C of the average melt temperature at any given time. However, in the time interval from 10 to 60 minutes, significant temperature gradients of up to 200 ˚C occurred.

The progression of the axial ablation front location during the course of the test is shown in Figure 3-55, while the analogous set of data for the north and south concrete sidewalls are provided in Figures 3-56 and 3-57, respectively. Finally, the maximum erosion rate measured on each concrete surface is shown in Figure 3-58. As is evident from Figure 3-58, ablation in the north and south walls progressed uniformly to a depth of ~ 7.5 cm over the first 11 minutes of the interaction, while the axial ablation had not yet commenced. This suggests that during the initial phase of the interaction, the basemat surface was protected by an insulating corium crust that formed upon initial melt contact with the cold concrete surface. The data further suggests that in the time interval from 40-55 minutes, the crust either remelted or mechanically failed, which allowed axial erosion to commence, albeit at a reduced rate relative to the lateral ablation. Based on the information provided in

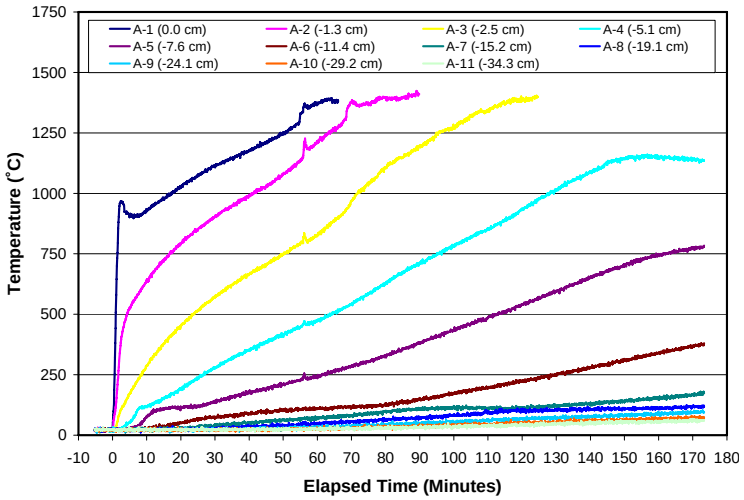

Figure 3-48. CCI-3 Basemat Heatup Near Centerline.

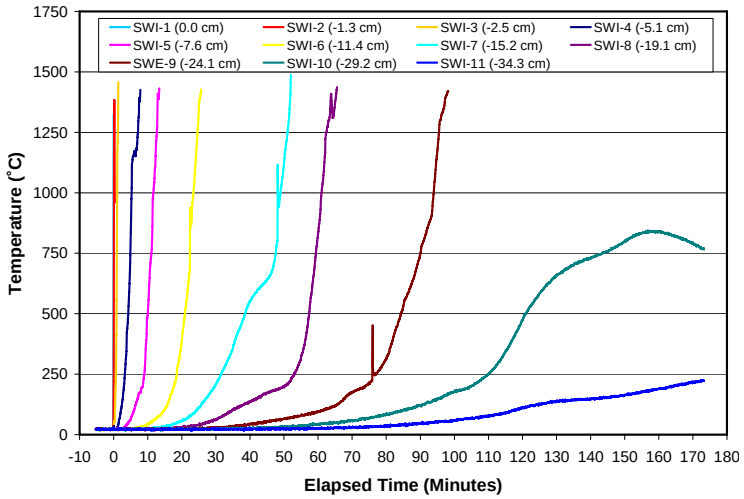

Figure 3-49. CCI-3 North Wall Heatup (+10 cm).

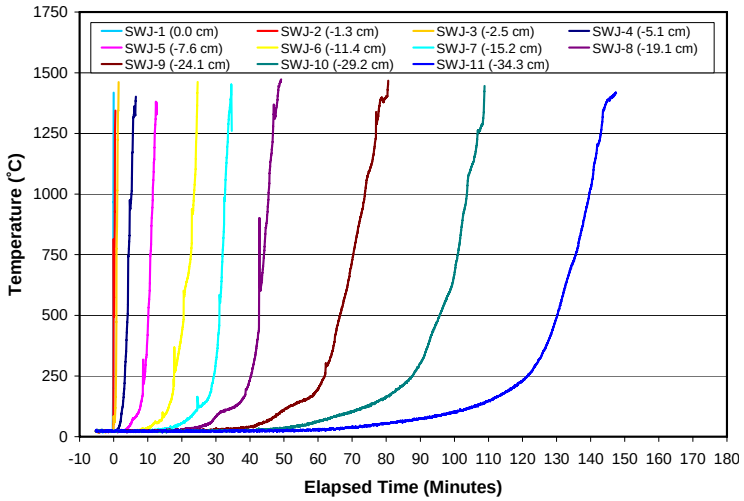

Figure 3-50. CCI-3 South Wall Heatup (+10 cm).

Figures 3-55 through 3-58, the following general observations regarding the ablation behavior for this test are made: i) there is no substantial incoherence between the lateral ablation rates on the North and South sidewalls, as occurred in Test CCI-1, and ii) lateral ablation is substantially greater than axial for this particular concrete type.

Over the time interval from 11 to 49 minutes, the melt pool was essentially quiescent, with only minor eruptions and melt splattering events occurring occasionally at various locations across the crust surface. At 49.3 minutes, major eruptions began almost simultaneously near the north and south walls. Both ejection and extrusion-type eruptions were observed. This phase terminated at 53.7 minutes, followed by another quiescent period until 59.0 minutes. At this time, significant eruptions began again and continued nearly unabated until 104.7 minutes into the test sequence. Many of the eruptions during this latter time interval were significant, with lava-type flows covering up to 60 % of the visible melt surface.

After 107.6 minutes of dry cavity operations, the criterion for flooding the cavity was reached on the basis of reaching the 30 cm ablation depth in the South concrete wall at the + 10.0 cm elevation (see Figure 3-57). As shown in Table 3-13, the lance was used to breach the crust at the melt upper surface prior to water addition, as specified in the test procedure. Immediately after crust breach, the cavity was flooded with ~ 125 liters of water to bring the water level over the melt to ~ 50

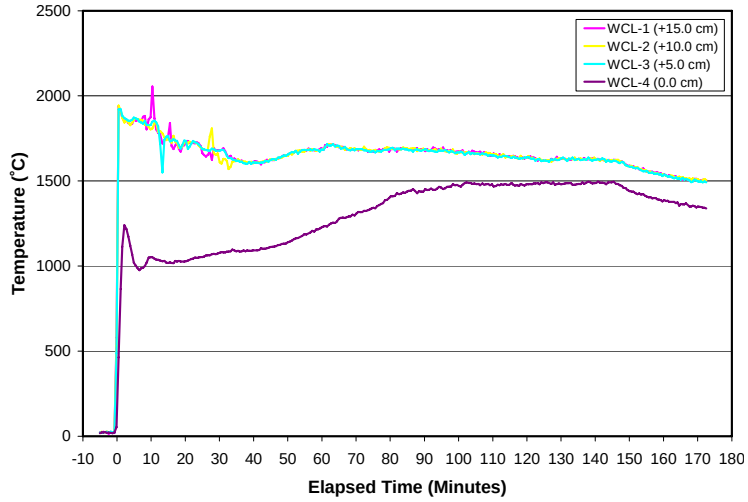

Figure 3-51. CCI-3 Melt Temperatures Near Centerline.

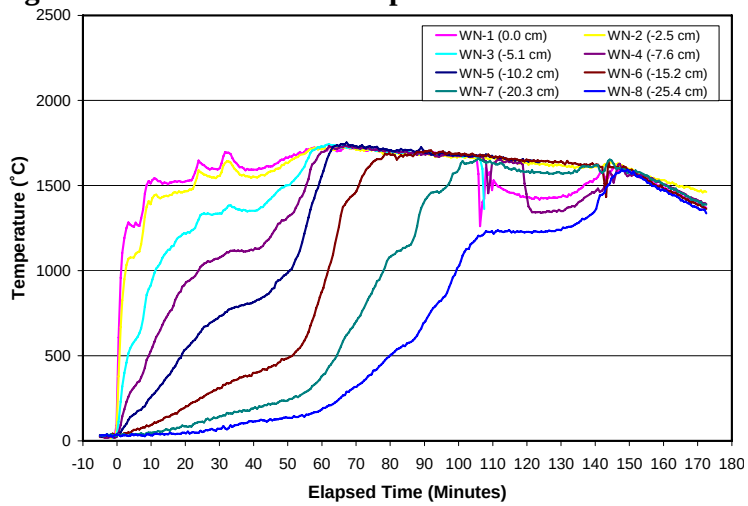

Figure 3-52. CCI-3 Melt Temperatures Near the North Wall (+5 cm Elevation).

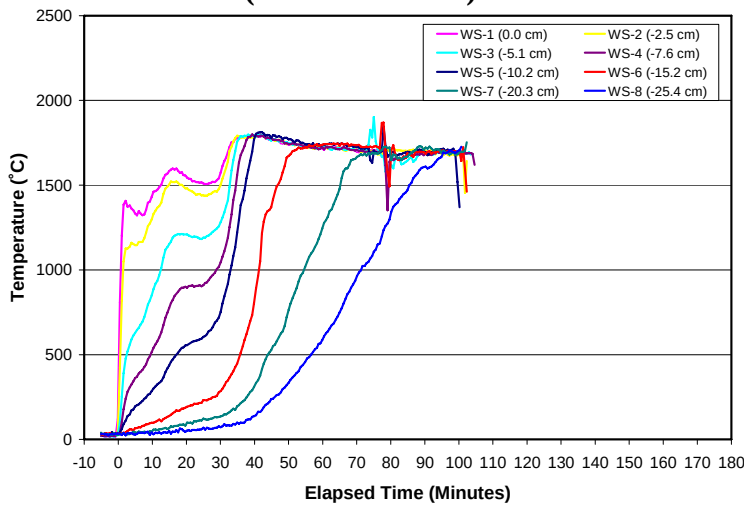

Figure 3-53. CCI-2 Melt Temperatures Near the South

cm. After this time, liquid lost to evaporation was periodically replaced to maintain the water level over the melt roughly in the range of 50 ± 5 cm per the test procedure.

The debris-water heat flux, calculated on the basis of the steam formation rate normalized by the test section planar area of 0.25 m^2, is shown in Fig. 3-59. As shown in the figure, the peak debris cooling rate upon initial flooding approached the critical heat flux limitation of 1 MW/m^2 under atmospheric boiling conditions. Over the next five minutes of the interaction, the debris cooling rate fell steadily to a level of ~ 500 kW/m^2 where it remained over the balance of the test. Examination of the melt temperature thermocouple data in Figures 3-51 through 3-54 indicates that water was not able to penetrate into the corium along the core-concrete interface to augment the overall debris cooling rate, as occurred in Test CCI-2.

After cavity flooding, power supply operation was switched from constant power to constant voltage mode per the normal test operating procedure. As is evident in Figure 3-47, the input power fell precipitously during this stage, which is consistent with substantial debris cooling. However, concrete ablation continued in both concrete sidewalls and the basemat, and at 140 minutes it became apparent that the test would soon be terminated on the basis of reaching the 35 cm ablation depth in the south wall. On this basis, the lance was inserted to breach the crust. Two load peaks were observed during this insertion sequence: the first peak occurred at

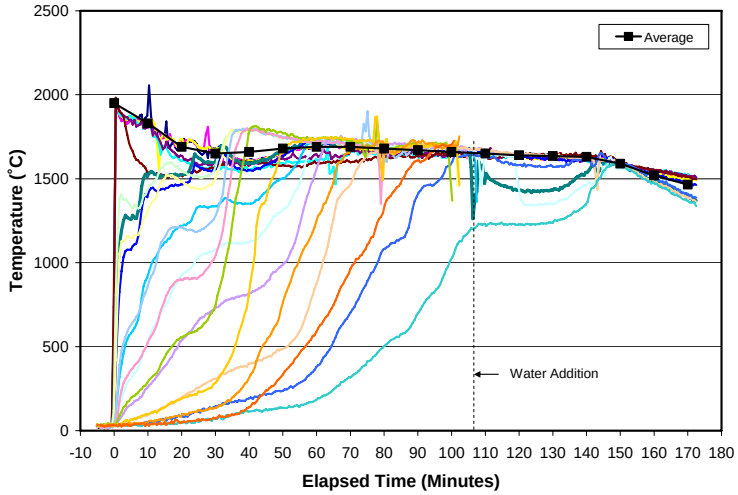

Figure 3-54. Collection of CCI-3 Melt Temperatures.

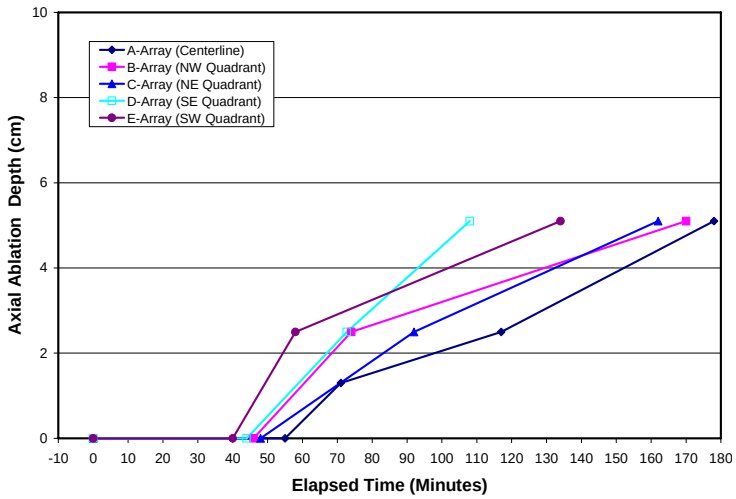

Figure 3-55. CCI-3 Axial Ablation.

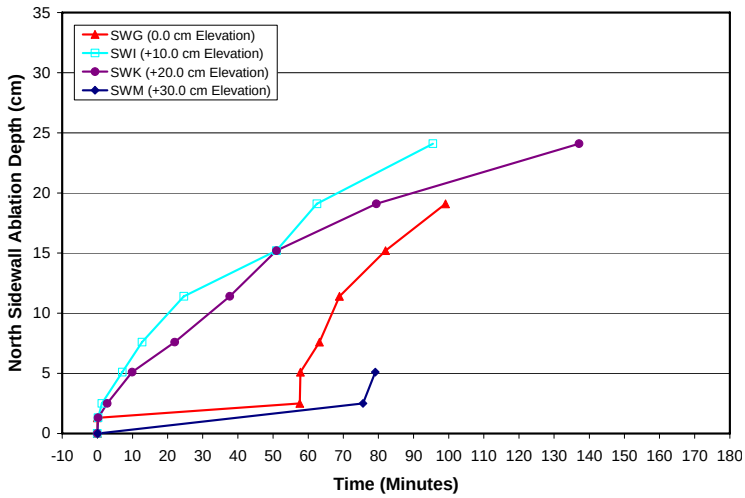

Figure 3-56. CCI-3 North Sidewall Ablation.

the +22.2 cm elevation, while the second was at the +20.0 cm elevation. As shown in Figure 3-59, breach did not noticeably increase the debris cooling rate for this test. As described in the next section, the posttest examinations indicated that the debris at the +20.0 cm elevation consisted of a porous, 5-10 cm thick crust layer that had already been quenched by the overlying water. Thus, the maximum insertion depth of +20.0 cm was not sufficient to fully penetrate this quenched debris layer to allow water to recontact the underlying melt. As a result, data on the transient crust breach cooling mechanism was not obtained for this test.

After the lance insertion sequence, the input power continued to fall while the heat removal rate from the debris remained significant. However, concrete ablation continued and the criterion for terminating the test was reached at 143.1 minutes, at which point the 35 cm ablation depth was reached in the South sidewall at the +10 cm elevation. On this basis, power input to the melt was terminated at 146 minutes. Data logging continued until 173 minutes to provide additional information on the debris cooling rate as the melt cooled.

In general, this test exhibited a high rate of cooling in comparison to previous one-dimensional MACE tests conducted with siliceous concrete.[2] However, unlike CCI-2, the increased cooling rate could not be attributed to water ingression at the molten core-concrete interface. Rather, the data and posttest examinations that are described

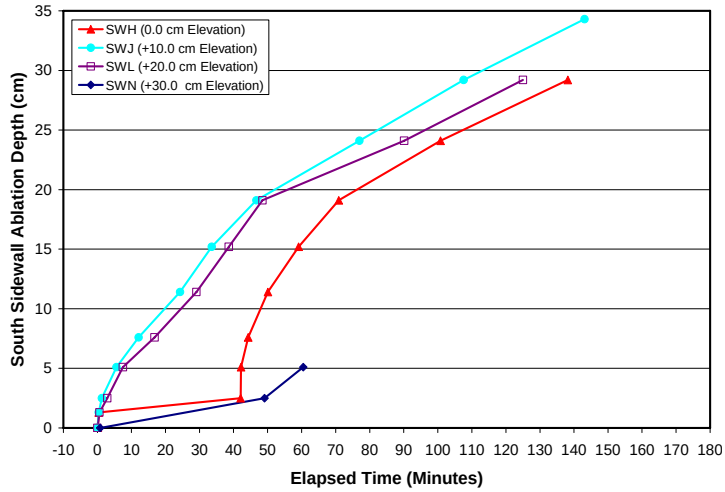

Figure 3-57. CCI-3 South Sidewall Ablation.

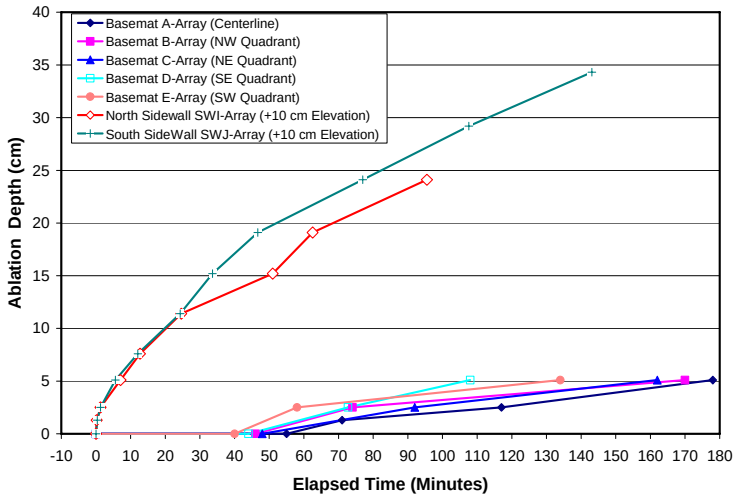

Figure 3-58. CCI-3 Axial and Lateral Ablation Data.

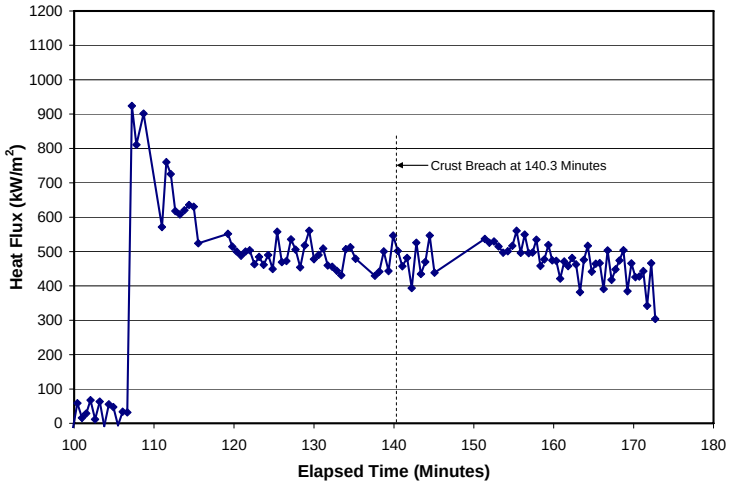

Figure 3-59. CCI-3 Melt-Water Heat Flux.

below indicate that the upper ~10 cm of the solidified material was porous. Since no melt eruptions were observed after cavity flooding, it thus appears that the increased cooling rate was attributable to water ingression directly into the solidifying core material.

As shown in Table 3-13, two load peaks were observed during the CCI-3 lance insertion sequence; the first was at 0.34 kN, while the second was at 0.67 kN. Moreover, posttest examinations (described later in this section) indicate that the first contact was with a partial bridge crust above the solidified debris that had a thickness in the range of 5 ± 2 cm. The second contact was with the porous, quenched crust layer over the solidified melt that was estimated to have a thickness of 7 ± 2 cm. With this data, evaluation of the crust strength (see Reference 5, Appendix A for the methodology) from well-known analytical solutions available in the literature[25] indicates that the failure stress of the partial bridge crust was ~ 0.24 MPa, with an uncertainty range of 0.12 to 0.89 MPa. Conversely, the failure stress of the quenched crust layer over the solidified melt was ~ 0.29 MPa, with an uncertainty range of 0.18 to 0.57 MPa. Thus, these measurements support the findings from the SSWICS test series, which indicated that crust material formed during quench is structurally quite weak. However, these measurements, as well as the CCI-1 strength measurement, are significant because they were carried out under prototypic temperature boundary conditions before the material had cooled to room temperature. This can be contrasted with the SSWICS measurements that were conducted at room temperature after the specimens had been removed from the test section.

Posttest Examination Results

As described in Section 2.11, the apparatus was carefully disassembled following the test in order to characterize the posttest debris configuration. A photograph of the top surface of the debris after disassembly down to the lower test section is provided in Figure 3-60. As for the other tests, sidewall crust material from the thermite burn had been deposited on the walls in the lower half of the middle section. The upper surface of the corium was covered with some loose debris, principally lava-type material plus particle bed, that originated from the melt eruptions that occurred during dry cavity operations. Based on large color differences seen between the materials, it appeared as though several different phases were present.

Figure 3-60. CCI-3 Debris Upper Surface in the As-Found Condition.

Once the surface characteristics were recorded, loose materials were removed to fully reveal the upper surface of the crust. For

reference, the masses of various debris regions recovered during disassembly are provided in Table 3-14. As shown in the table, a total of 14.6 kg of sidewall crust material was removed from the inner surfaces of the middle sidewall section. This was splatter material deposited during the thermite burn which did not participate in the core-concrete interaction. In addition, a total of 47.7 kg of sidewall crust and splatter material from melt eruptions prior to water addition was recovered from the lower section sidewalls above the surface of the solidified corium. Roughly half of this material was probably deposited during the thermite burn and did not participate in the interaction. Thus, in future analyses of CCI-3, a total of ~40 kg should be subtracted from the initial melt mass to obtain the actual mass that participated in the core-concrete interaction. Aside from the sidewall crust material, a total of 8.5 kg was present on the crust upper surface in the form of a discrete lava flow that had originated near the south concrete wall.

Removal of the loose materials fully revealed the remnants of the hole that had been produced in the upper crust during the crust breach sequence. The hole is visible in Figure 3-60, while a close-up photograph of the opening is provided in Figure 3-61. Probing through the hole at this point indicated that void pockets were present below the crust. Moreover,

Figure 3-61. Photograph of Hole Formed by Lance Through the CCI-3 Bridge Crust.

Table 3-14. Masses of Material Regions Measured During Disassembly for CCI-3.

Material Description	Mass (Kg)	Note(s)
Sidewall crust material from middle section sidewalls.	14.4	-
Sidewall crust material from lower section above corium crust.	47.7	Consisted of crust material deposited during thermite burn, and splattered material from melt eruption processes prior to water addition.
Partially anchored top crust	85.4	Void pockets were found between the crust and underlying solidified melt, but the void was not continuous as in previous MACEtests.[1-2]
Eruption mound near south wall.	8.5	-
Recovered UO_2 pellets.	316.1	A total of 369.4 kg were loaded behind the electrodes. The balance of the material was left as a sintered layer on the back of the electrodes.

the crust was fragile and it was clear that this material would not survive during removal of the test section sidewalls. As a result, the crust was removed by hand to reveal the underlying, solidified corium pool. The thickness of this crust was in the range of 5 ± 2 cm. This process revealed that a continuous, well-defined void region had not developed as in previous MACE integral effect tests.[1-2] Rather, void pockets were present (typical dimension of ~ 15 cm) with pillar-like formations of solidified melt that bridged the gap between the crust and underlying corium. As shown in Table 3-14, the total mass of this partially anchored upper crust amounted to 85.4 kg.

Figure 3-62. CCI-3 Photograph of Void Pocket Over Solidified Melt in South Wall.

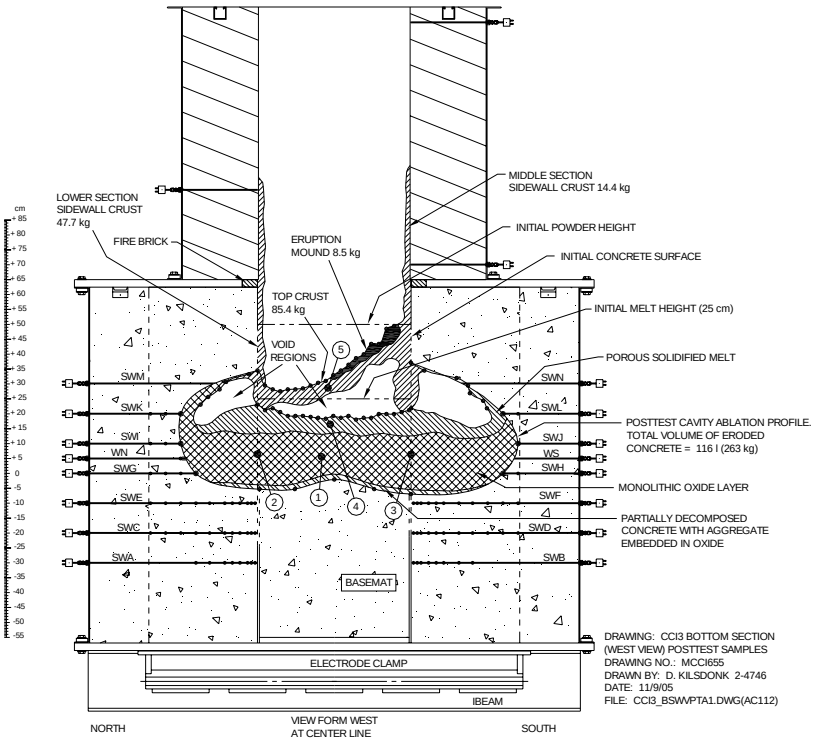

Figure 3-63. Rendering of CCI-3 Posttest Debris Configuration.

Removal of the bridge crust in the central region of the test section also revealed the presence of void pockets in the north and south concrete walls over the solidified melt pool that had penetrated into these structures. A photograph of the void in the south wall is provided in Figure 3-62, while a rendering of the overall debris configuration that was developed on the basis of the posttest examinations is provided in Figure 3-63. As shown in Figure 3-62, the solidified melt upper surface in the void pockets was smooth and devoid of cracks, which can be contrasted with the rough, cracked structure in the central region of the test section. This type of morphology is consistent with core material that has undergone a slow freezing process under dry conditions. This finding, along with the sidewall thermocouple measurements provided earlier in the section, indicates that water was not able to penetrate through the frozen material that isolated these pockets from the main body of the test section (see Figure 3-63) to cool the corium pool in direct contact with the sidewalls.

Prior to initiating removal of the test section sidewalls, a platform drill was used to obtain an axial core sample near the center of the test section. A photograph of the hole created in the corium by the drilling process is shown in Figure 3-64, while a photograph of the core sample that was recovered from this procedure is provided Figure 3-65. The core sample was used to collect specimens for chemical analysis; this data is provided later in the section. The initial view of the axial debris structure through the core hole indicated that the upper region of the debris was composed of a semi-porous layer, while the lower region consisted of a hard, dense oxide. As shown in Figure 3-63, this general debris structure was confirmed as the debris characterization continued.

With these steps completed, the MgO sidewalls were removed to provide access for gaining additional information regarding the overall cavity erosion profile and debris morphology. A photograph showing the bank of tungsten electrodes after removal of the west sidewall of the test section is provided in Figure 3-66. Sintering of the crushed UO_2 pellets on the electrodes is indicative of melt contact with the front surface of the electrodes. On this basis, the distribution of the sintered pellets seen in Figure 3-66 verified the trends of

Figure 3-64. Photograph of Core Sample Opening Through CCI-3 Crust.

Figure 3-65. CCI-3 Axial Core Sample.

Figure 3-66. CCI-3 View After Removal of West MgO Wall.

minimal axial basemat erosion and relatively symmetrical lateral sidewall erosion, as indicated by the thermocouple data provided earlier in this section. During removal of the MgO sidewalls, the remnants of the UO_2 pellet liner were collected and weighed. As shown in Table 3-14, over 85 % of the pellets were recovered during this step, with the balance of the material retained as a sintered layer on the back of the electrodes.

After the MgO sidewalls were removed, the concrete walls and basemat were lifted from between the two banks of tungsten electrodes and set on the test section platform for detailed examinations to better quantify the posttest debris distribution. North and south (non-electrode sidewall) views of the basemat and overlying corium debris are provided in Figure 3-67, while East and West (electrode sidewall) views are shown in Figure 3-68. Conversely, face-on views of the two concrete sidewalls after removal are provided in Figure 3-69.

As indicated in Figure 3-63, the ablation front for this test appeared to consist of a region where the core oxide had locally displaced the cement that bonded the aggregate. As discussed

(a) **(b)**

Figure 3-67. CCI-3 Debris Over Basemat: (a) View From North (b) View From South.

(a) **(b)**

Figure 3-68. CCI-3 Debris Over Basemat: (a) View From East (b) View From West.

(a) **(b)**

Figure 3-69. CCI-3 Concrete Walls: (a) North, and (b) South.

earlier in this section, this same type of morphology was discovered during posttest examinations for Test CCI-1. This region is evident in Figures 3-67 and 3-69 as a 2-3 cm thick layer that separates the fresh concrete from the overlying oxide. As shown in Figure 3-63, the core material in contact with this ablation boundary consisted of a 10-15 cm thick layer of hard, dense, monolithic oxide that had solidified with very little porosity.

Above the heavy oxide phase was a porous layer that appeared to be the crust material that formed when the cavity was flooded. The average crust thickness was nominally 5 cm, with a variation range of ± 2 cm across the extent of the basemat. This is consistent with crust thicknesses observed in MACE tests.[1-2] It is noteworthy that this crust had not separated from the underlying melt to form an intervening void. As shown in Figures 3-67 and 3-68, the boundary between the crust and the underlying heavy oxide phase appeared to consist of a seam that may have constituted the liquid/solid phase boundary at the time the test was terminated. As is evident in the photographs, the crust layer also contained pieces of partially melted aggregate that were present in the melt zone that formed the crust when the material was quenched. The aggregate was probably displaced at the ablation interface and then floated up through the heavy oxide where it went into solution in this melt zone.

In general, the overall debris morphology for test CCI-3 was very similar to that described earlier for test CCI-1, which was also conducted with siliceous concrete.

During disassembly, samples were collected from various regions of the debris for elemental analysis.[22] The sample locations are shown in Figure 3-63, while sample descriptions are provided in Table 3-15. As described previously, all samples were analyzed for the key elements present in the initial corium charge (U, Zr, Si, Ca, Mg, Al, Cr), as well as other trace elements or potential impurities. The elemental results were converted to assumed oxide forms for direct comparison with the initial corium composition. The corresponding mass balance provides a good indication of whether or not the assumed oxide forms are correct. For all samples the mass balances were reasonably good (100 ± 3 %), indicating that the sample stoichiometry is close to that assumed. Presence of trace elements/impurities was small (< 0.1 % per element), with the exception of tungsten, which was as high as 1.65 wt %. Tungsten originated from dissolution of the electrodes and thermowells during the test.

As is evident from Figure 3-63, the lateral composition variation across the full extent of the debris near the axial centerline of the material can be determined by comparing the analysis results for Samples 1-3. This comparison is provided in Table 3-16. The reported measurement uncertainty in this data is ± 10% of the value shown for each constituent. For reference, the initial melt composition is provided in Table 3-16, as well as the estimated average debris

Table 3-15. Summary of CCI-3 Sample Locations.

Sample	Description/Location	Note(s)
1*	Near axial centerline of heavy oxide layer at the test section center.	These samples provide data on the lateral composition variation of the heavy oxide layer.
2	North concrete sidewall near the axial centerline of the solidified corium	
3	South concrete sidewall near the axial centerline of the solidified corium	
4*	Near axial centerline of porous crust layer at test section center.	This sample, along with No. 1, provides data on axial composition variation.
5	Partially anchored bridge crust near the test section center.	Provides data on the timing of bridge crust formation.

*Taken from core sample recovered from core drilling at the test section centerline.

Table 3-16. CCI-3 Analysis Results for Samples Taken Across Lateral Extent of the Debris Near the Debris Axial Centerline.

Const.	Wt % Constituent at Sample Location			Initial* Comp. (Wt %)	EOT Comp. (Wt %)
	No. 2: Heavy Oxide Near North Wall	No. 1: Heavy Oxide Near Centerline	No. 3: Heavy Oxide Near South Wall		
UO_2	33.37	34.81	33.82	54.70	33.09
ZrO_2	14.05	15.76	14.08	22.46	13.59
SiO_2	37.76	36.07	37.48	10.85	35.76
MgO	0.54	0.52	0.54	0.12	0.49
Al_2O_3	2.08	1.83	2.02	0.62	2.09
CaO	11.69	10.49	11.50	2.15	9.48
Cr_2O_3	0.51	0.52	0.56	9.10	5.50

*Assumes Cr metal is fully oxidized for direct comparison with ICP/AES results.

composition at End of Test (EOT).[c] In general, the compositions of these three samples also cluster around the EOT composition. The composition of the two samples taken adjacent to the North and South concrete walls are virtually identical. The sample taken near the center of the test section is very slightly elevated (~ 3%) in core oxide content in comparison to the samples taken adjacent to the walls.

As is evident from Figure 3-63, data regarding the axial composition variation is provided by comparing Samples 1, 4, and 5. This comparison is provided in Table 3-17. The compositions of these three samples also cluster around the EOT composition. The bridge crust is slightly elevated in core oxide content in comparison to the underlying porous and dense oxide layers, which indicates that this was probably the crust surface that was evident on the melt surface at the time of cavity flooding. The underlying porous crust layer is slightly elevated (~ 2%) in concrete oxides relative to the underlying dense oxide layer. Moreover, this crust is believed to have formed soon after water was added to the test section. Thus, this phase was probably present at the melt upper surface at the time the cavity was flooded.

In general, the posttest chemical distribution of the solidified debris is qualitatively similar to that described earlier for test CCI-1, which was also conducted with siliceous concrete.

3.4 Discussion

The CCI test series investigated the effects of concrete type and input power on two-dimensional core-concrete interaction under both wet and dry cavity conditions. The purpose of this section is to compare the results from the three experiments conducted as part of the test

Table 3-17. CCI-3 Analysis Results for Samples Taken At Three Axial Elevations Near the Test Section Centerline.

Const.	Wt % Constituent at Sample Location			Initial* Comp. (Wt %)	EOT Comp. (Wt %)
	No. 5: Bridge Crust Near Centerline	No. 4: Porous Crust Over Heavy Oxide	No. 1: Heavy Oxide Near Centerline		
UO_2	35.50	32.59	34.81	54.70	33.09
ZrO_2	15.64	14.13	15.76	22.46	13.59
SiO_2	35.31	37.29	36.07	10.85	35.76
MgO	0.50	0.53	0.52	0.12	0.49
Al_2O_3	1.78	2.01	1.83	0.62	2.09
CaO	10.20	11.32	10.49	2.15	9.48
Cr_2O_3	1.07	2.13	0.52	9.10	5.50

*Assumes Cr metal is fully oxidized for direct comparison with ICP/AES results.

[c]The EOT composition for CCI-3 was determined by reducing the initial 375 kg melt mass (see Table 2-4) by the estimated sidewall crust mass of 38.3 kg deduced during disassembly (see Table 3-14), and then adding in the estimated slag mass eroded into the melt over the course of the test. As shown in Figure 3-63, ~ 216 liters of concrete were eroded during the test, which amounts to 263 kg given the initial concrete density (Table 2-2). The slag mass of 227.5 kg was then deduced from the eroded concrete mass after removing the CO_2 and H_2O decompositions gases (13.5 wt % from Table 2-1) that were released during ablation. The slag was then proportioned into the principal oxide components (SiO_2, CaO, Al_2O_3, and MgO) according to relative ratios for this concrete type (see Table 2-2).

series to identify key parametric effects. Principal variables measured during the experiments included melt temperature, local concrete ablation rates, and debris/water heat flux after cavity flooding. A comparison of the these key measurements is provided in Figures 3-70 through 3-73, which provide the estimated average melt temperature, maximum lateral and axial concrete ablation rates, and debris/water heat flux plotted for each of the tests.

As shown in Figure 3-70, the initial melt temperature for the tests was in the range of range of 1880-1950 ºC. The differences were due to uncertainty/variability in the thermite reaction temperatures for the three different chemical mixtures used to generate the initial melt compositions. During dry cavity operations, all tests showed the overall trend of decreasing melt temperature as ablation progressed, which was due to a heat sink effect as relatively cool concrete slag was introduced into the melt, as well as the increasing heat transfer surface area as the melts expanded into the concrete crucibles. The decline in melt temperature may further reflect the evolution of the pool boundary freezing temperature that decreased as additional concrete was eroded into the melt over the course of the tests.

Somewhat different behavior was noted for CCI-1, in which the melt temperature was relatively constant over the first ~40 minutes of the interaction. One possible contributor to this trend was the fact that this test was run at a 25 % higher power level in comparison to CCI-2 and CCI-3 (i.e. 150 kW vs. 120 kW; see Table 1-1). However, the lack of a temperature decline may have also been caused by crust formation at the core-concrete interfaces that acted to

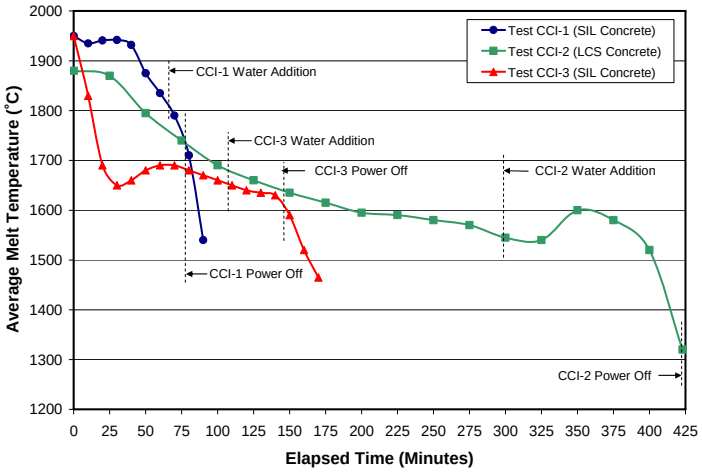

Figure 3-70. Average Melt Temperatures for CCI Tests.

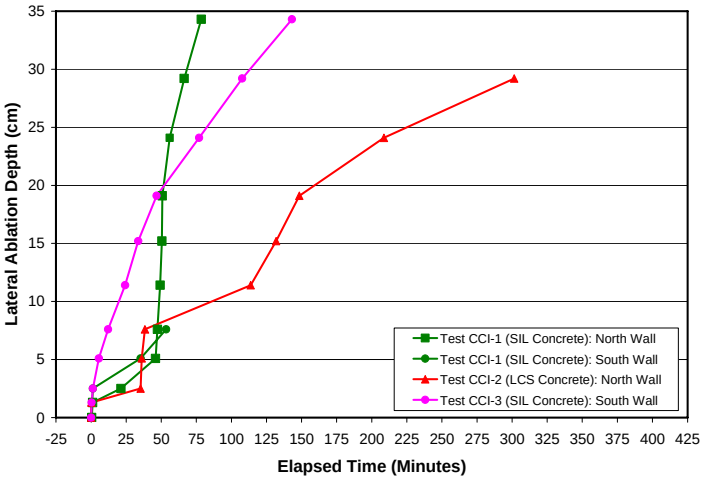

Figure 3-71. Lateral Ablation for CCI Tests.

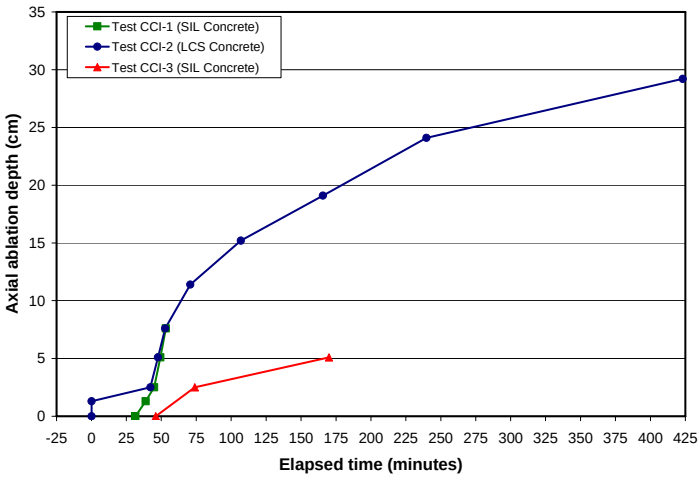

Figure 3-72. Axial Ablation for CCI Tests.

insulate the melt. Relatively low heat transfer rates to the concrete boundaries were evidenced by the low ablation rates exhibited over the first 40 minutes. However, once the surface crusts failed, ablation proceeded rapidly, and the CCI-1 melt temperature fell rapidly in comparison to the other tests. This initial stable crust behavior may have been linked to the exceptionally low gas content for this concrete type in comparison to others used in the test series (see Table 3-18). In particular, gas sparging at the core-concrete interface may provide the mechanical force required to dislodge the crust material from the interface, thereby allowing ablation to proceed. If this interpretation is correct, then the absence of significant gas sparging allowed the insulating crusts to remain stable over an extended period of time in Test CCI-1, which in turn caused the melt temperature to increase.

Aside from Test CCI-1, examination of Figures 3-70 through 3-72 indicates that Tests CCI-2 and CCI-3 also showed evidence of early crust formation phases that influenced the overall ablation behavior. For CCI-2, both axial and lateral ablation rates were quite low and the melt temperature relatively constant until ~ 30 minutes, after which time a period of rapid erosion occurred. However, unlike CCI-1, these erosion bursts were not sustained. Rather, after ~ 5 cm of ablation, both the axial and lateral ablation rates slowed significantly and approached a quasi-steady state. The reduced period of crust stability for CCI-2 is consistent with the idea that gas sparging can disrupt surface crusts, since the gas content of the CCI-2 concrete was significantly greater compared to CCI-1 (see Table 3-18).

Unlike tests CCI-1 and CCI-2, sidewall erosion in test CCI-3 commenced immediately upon contact with melt, and progressed steadily throughout the balance of the test. Conversely, the data suggests that the concrete basemat was

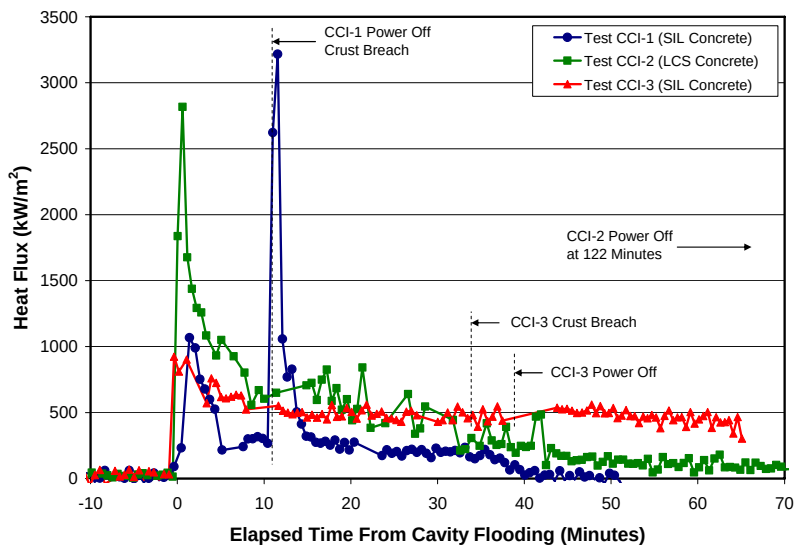

Figure 3-73. Debris/Water Heat Flux for CCI Tests.

Table 3-18. Properties of Concretes Used in CCI Test Series.

Concrete Property	Property for Test:		
	CCI-1	**CCI-2**	**CCI-3**
Type	SIL (US)	LCS	SIL (EU)
Liquidus Temperature[23] (ºC)	1250	1295	1250
Gas Content (wt %)	4.6	34.1	13.5
Decomposition Enthalpy (MJ/kg)[a]	1.60	2.27	1.72
Density (kg/m^3)	2300	2330	2270

[a]Evaluated at concrete liquidus temperature

protected by an insulating crust until ~ 50 minutes, at which point the crust failed and erosion commenced, albeit at a reduced rate relative to lateral ablation.

Aside from the initial cavity erosion behavior, examination of Figures 3-71 and 3-72 indicates that the long-term ablation process is influenced by concrete type. Estimates of average lateral and axial ablation rates for the three tests are provided in Table 3-19. To the extent possible, data points for these estimates were selected near the end of the dry cavity erosion phase for each test so that the erosion rate estimates are indicative of the long-term behavior. Assuming a quasi-steady erosion process, then the heat flux at the core-concrete interface is related to the ablation rate through the expression:

$$q_c'' = \rho_c h_{dc} \dot{\delta} c, \tag{3-1}$$

where ρ_c is the concrete density, h_{dc} is the concrete decomposition enthalpy, and $\dot{\delta}_c$ is the ablation rate. The assumed property data required to evaluate the above expression is provided in Table 3-18; the corresponding heat flux estimates are provided in Table 3-19. As shown in the table, lateral and axial ablation rates for Test CCI-2, which was conducted with LCS concrete, were virtually indistinguishable; the concrete erosion rate averaged 4 cm/hr over several hours of interaction before gradually decreasing; the corresponding surface heat flux was ~ 60 kW/m^2. Thus, the lateral/axial heat flux ratio for this test was approximately unity.

The relatively uniform power split for CCI-2 can be contrasted with the results of the two tests conducted with siliceous concrete. For test CCI-1, the ablation was highly non-uniform, with most of the ablation concentrated in the North sidewall of the test apparatus. As described above, this test was conducted at a higher power density in comparison to CCI-2 and CCI-3. Moreover, the concrete for this test had exceptionally low gas content (see Table 3-18). Based on the discussion provided above, it thus appears that crust stability played a major role in determining the ablation progression for this experiment. In particular, the data suggests that

Table 3-19. Lateral/Axial Ablation Rate and Power Split Estimates for CCI Tests.

Test	Concr. Type	Lateral Ablation		Axial Ablation		Lateral-Axial Heat Flux Ratio	Data Points Utilized for Ablation Rate Estimates
		Ablation Rate (cm/hr)	Heat Flux (kW/m^2)	Ablation Rate (cm/hr)	Heat Flux (kW/m^2)		
CCI-1	SIL (US)	N: 39.1	395	26.1[b]	265	–[a]	N Lateral: (19.1 cm, 51 min) (29.2 cm, 66 min) S Lateral: (7.6 cm, 54 min) (5.1 cm, 35 min) Axial: (7.6 cm, 53 min) (1.3 cm, 39 min)
		S: 8.4	86				
CCI-2	LCS	4.0	58	4.0	59	1.0	Lateral: (19.1 cm, 148 min) (29.2 cm, 302 min) Axial: (15.2 cm, 107 min) (24.1 cm, 240 min)
CCI-3	SIL (EU)	10.0	97	2.5	25	4.0	Lateral: (19.1 cm, 47 min) (29.2 cm, 107 min) Axial: (2.5 cm, 117 min) (5.1 cm, 178 min)

[a]Heat flux ratio not evaluated for this test due to large asymmetry in lateral cavity erosion.
[b]Ablation burst; rate appeared to slow significantly after this time interval; see Figure 3-2.

after the insulating crust failed on the North concrete sidewall, the input power was dissipated predominately through ablation of this sidewall, while crusts continued to protect the basemat and south sidewall surfaces. As shown in Table 3-19, the ablation rate averaged 39 cm/hr in the North wall over the last 30 minutes of dry cavity operations; the average concrete surface heat flux was ~ 395 kW/m^2. Conversely, brief ablation bursts that reached 8.4 cm/hr in the South wall and 26 cm/hr axially occurred early in the experimental sequence, but the data suggests that crusts subsequently reformed on these surfaces, resulting in very little ablation over the balance of test operations. Based on these transient effects, a power split estimate was not formulated for this test, since the estimate would be highly speculative.

In contrast to Test CCI-1, the second test conducted with siliceous concrete (CCI-3) exhibited fairly symmetrical ablation insofar as the progression of the ablation fronts into the two opposing sidewalls of the apparatus is concerned. However, unlike Test CCI-2, the lateral ablation was highly pronounced in comparison to axial for this particular test. In this regard, the results of tests CCI-1 and CCI-3 are consistent. As shown in Table 3-19, lateral ablation averaged 10 cm/hr over the last hour of the experiment, while the axial ablation rate was limited to 2.5 cm/hr over the same timeframe. The corresponding heat fluxes in the lateral and axial directions were 97 and 25 kW/m^2, respectively. On this basis, the lateral/axial surface heat flux ratio for test CCI-3 was estimated as ~ 4, which is significantly higher than the near-unity ratio deduced for test CCI-2 with LCS concrete. Thus, this data suggests that there is a strong effect of concrete type on the spatial heat flux distribution at the core-concrete interface during dry core-concrete interaction. Between these two concrete types, possible explanations for differences in the erosion behavior are chemical composition (LCS concrete has a high CaO/SiO_2 ratio in comparison to siliceous; see Table 2-1), and concrete gas content (LCS has ~ 2.5 times as much gas as siliceous; see Tables 2-1 and 3-18). A third possible explanation was revealed during posttest examinations. In particular, the nature of the core-concrete interface was noticeably different for Test CCI-2 in comparison to Tests CCI-1 and CCI-3. As shown in Figure 3-74, the ablation front for the two tests conducted with siliceous concrete consisted of a region where the core oxide had locally displaced the cement that bonded the aggregate. Conversely, the ablation front for Test CCI-2 consisted of a powdery interface in which the core and concrete oxides were clearly separated. The interface characteristics may have influenced the heat transfer rate across the boundaries, thereby resulting in different ablation behavior for the two concrete types.

Aside from the overall cavity erosion behavior, video footage from the tests indicated that a crust was present over the melt upper surface during most of the dry cavity ablation phase for all three tests. The crusts contained vent openings which allowed melt eruptions to occur as the tests progressed. The frequency and intensity of the eruptions were directly correlated to the gas content of the concrete for any given test.

In terms of the chemical analyses conducted as part of the test series, samples were collected to characterize the lateral and axial composition variations of the solidified debris, and also to characterize the composition of corium regions that played key roles in the coolability aspects of the tests (e.g., porous crust zones formed at the melt/water interface, and the material erupted after cavity flooding in CCI-2). Analysis of samples taken to characterize the lateral composition variation indicate that for all tests, the corium in the central region of the test section had a higher concentration of core oxides in comparison to samples collected near the two ablating concrete sidewalls. Conversely, samples taken to characterize the axial composition variation over the vertical extent of the solidified corium remaining over the basemat indicate the

general trend of slightly increasing core oxide concentration as the concrete surface is approached. For both tests conducted with siliceous concrete, two zones appeared to be present: a heavy monolithic oxide phase (10-15 cm deep) immediately over the basemat that was enriched in core oxides, with a second overlying porous, light oxide phase (5-10 cm deep) that was enriched in concrete oxides. This axial phase distribution is clearly evident in Figure 3-74. The overlying oxide phase was porous and appeared to have been quenched after the cavity was flooded. This well-defined phase distribution can be contrasted with the debris morphology for CCI-2. As shown in Figure 3-74, the debris for this test was highly porous and fragmented over the entire axial extent of the material remaining over the basemat. This open structure is consistent with the high degree of debris cooling that occurred during this test.

Aside from examining the thermalhydraulic aspects of molten core-concrete interaction under dry cavity conditions, a second and equally important aspect of the test series was to investigate debris coolability under late-phase flooding conditions. In terms of phenomenology, four cooling mechanisms were targeted for investigation at the onset of the MCCI program:[19] i) bulk cooling, ii) water ingression through cracks/fissures in the solidifying material, iii) melt eruptions, and iv) transient crust breach. As a whole, the test series provided data on all four of these mechanisms. In addition, Test CCI-2 provided data on water ingress at the interface between the core material and concrete sidewalls. In this experiment, thermocouple measurements clearly indicated that water was able to penetrate at this interface and effectively cool the concrete sidewalls to saturation, thereby terminating the lateral cavity erosion process. This mechanism had been previously identified in the COTELS reactor material test series,[11] even though these tests were conducted at a relatively high power density in comparison to the tests reported herein.

As shown in Figure 3-73, the heat flux during the first 5 minutes following cavity flooding was high for all tests. For the two tests conducted

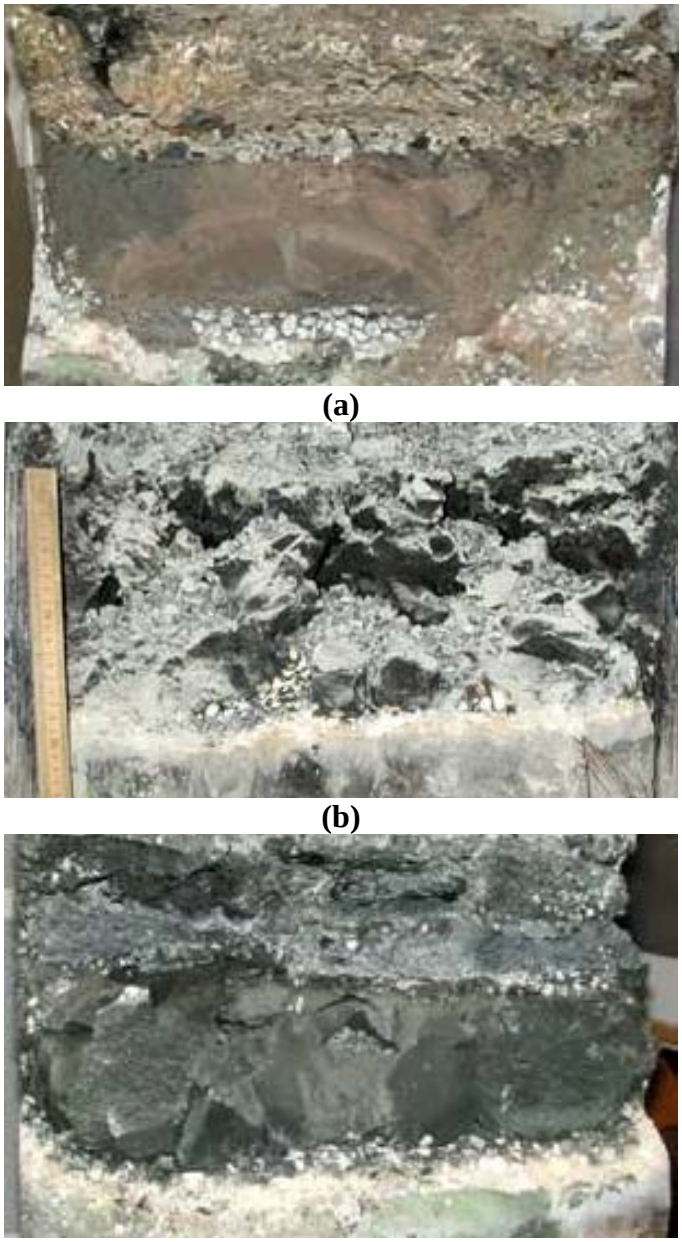

(a)

(b)

(c)

Figure 3-74. Axial Debris Morphology for Test: (a) CCI-1, (b) CCI-2, and (c) CCI-3.

with siliceous concrete, the initial heat fluxes approached the Critical Heat Flux (CHF) limitation of ~ 1 MW/m^2 under saturated boiling conditions. Thus, the heat fluxes were indicative of quenching of the upper surface crust that was present as an initial condition for both tests. Although the lance was used to puncture the crust for these tests before the cavity was flooded, the crusts were floating and the openings were generally small compared to the remaining crust surface area over the melt. However, for test CCI-2, the upper surface was essentially devoid of a surface crust at the time of cavity flooding due to the insulating effect of the overlying crust mantles that had formed over the previous five hours of dry cavity operations. Thus, water was able to directly contact the melt, resulting in a bulk cooling transient in which the initial cooling rate approached 3 MW/m^2. As is evident from Figure 3-73, the heat flux eventually fell below 1 MW/m^2 after ~ 5 minutes. At this time, a stable crust most likely formed at the melt-water interface, thereby terminating the bulk cooling transient.

As is evident from Figure 3-70, the tests did not generally exhibit a pronounced decrease in overall melt temperature after cavity flooding. This is despite the fact that the heat flux and power supply responses both indicated substantial debris cooling. This type of behavior can be rationalized by a latent heat transfer process in which a quench front develops at the melt/water interface, as opposed to a sensible heat transfer process in which the entire melt mass is cooled by convective heat transfer with the heat dissipated to the overlying water by conduction across a thin crust at the melt/water interface. Indeed, the bulk melt temperature response, power supply response in constant voltage operating mode,[d] and posttest debris morphology are consistent with development of quenched debris zones as opposed to bulk cooldown of the entire melt mass by conduction-limited cooling across a thin crust at the interface. In fact, as shown in Figure 3-70, the average melt temperature in test CCI-2 actually increased for a period after water addition, while the debris was undergoing extensive cooling.

In order to compare the general cooling behavior, characteristic heat flux estimates were developed for each of the three tests by averaging the heat flux data over the time interval from 15-25 minutes after cavity flooding. This particular interval was selected since structure source/sink effects had effectively died away at this point, and also the onset of the melt eruption phase had not yet been initiated in Test CCI-2 (see Table 3-7). Thus, the debris cooling rates should be indicative of the crust-limited heat transfer phase of the experiments. The heat flux estimates derived from the data shown in Figure 3-73 are provided in Table 3-20. Also shown in the table is the gas content of the concrete used for each test (taken from Table 3-18), as well as the concrete content of the upper crust/debris region that was in contact with the water during the time interval under consideration. As is evident from the table, the debris/water heat fluxes ranged from 250 to 650 kW/m^2. The cooling rates for both siliceous concrete tests were lower than CCI-2, which was conducted with LCS concrete. Further examination of the data indicates that the heat flux increased with concrete gas content. For reference, the SSWICS water ingression heat transfer correlation[3] predicts an ingression-limited heat flux in the range of 40-90 kW/m^2 for the concrete types and crust concrete contents shown in Table 3-20. The heat fluxes realized in the tests are as much as an order of magnitude higher than that predicted by the correlation. However, note that the SSWICS correlation was developed on the basis of core melts quenched in the absence of gas sparging.[3] Thus, if water ingression did contribute to the overall debris quenching rate in the CCI tests, then this comparison suggests that the degree of

[d]After water addition, the power supply was run in constant voltage mode to maintain the specific power density in the remaining melt zone approximately constant should a solidification (quench) front develop during the interaction. This was done since the DEH technique does not appreciably heat solidified corium.

Table 3-20. Debris-Water Heat Fluxes for CCI Tests Averaged Over the Time Interval 15-25 Minutes after Cavity Flooding.

Test	Concrete Type	Heat Flux (kW/m^2)	Concrete Gas Content (Wt %)	Crust[a] Concrete Content (Wt %)	Note(s)
CCI-1	SIL (US)	250	4.6	22.3	Assumed heat transfer surface area: 0.25 m^2 (PTE indicates that water did not penetrate sidewall crusts to cool the top surface of the corium interacting with the sidewalls).
CCI-2	LCS	650	34.1	69.4	Assumed surface heat transfer area: 0.50 m^2 (PTE indicates that water was able to contact the entire melt upper surface area). Water ingress at the interface between the corium and concrete walls also contributed to cooling, but this effect has not been separated from the overall heat flux estimate.
CCI-3	SIL (EU)	500	13.5	51.2	See Note for Test CCI-1.

[a]Chemical samples used to characterize crust composition: CCI-1: No. 7; CCI-2: No. 3; and CCI-3: No. 4.

interconnected cracks/fissures/porosity that form the pathway for water to ingress into solidifying core material is increased by the presence of gas sparging, particularly for the case in which the melt contains a high concrete fraction.

As noted above, the power supply response and melt temperature evolution after cavity flooding in the tests was indicative of a latent heat transfer (i.e., quenching) process, as opposed to convective cooling of the entire melt mass. The heat flux estimates shown in Table 3-20, in conjunction with the findings from the posttest examinations, provide the necessary information to check this hypothesis using an alternative approach. In particular, under the condition in which the crust at the melt/water interface is impervious to water ingression, then the quasi-steady crust thickness can be evaluated from the well-known expression:

$$q''_{cr} = \frac{k_{cr}(T_{frz} - T_{sat})}{\delta_{cr}} \quad \Rightarrow \quad \delta_{cr} = \frac{k_{cr}(T_{frz} - T_{sat})}{q''_{cr}} \tag{3-2}$$

where q''_{cr} is the conduction-limited heat flux to the overlying water, k_{cr} is the crust thermal conductivity, T_{frz} is the crust freezing temperature, T_{sat} is water saturation temperature (100 ºC), and δ_{cr} is the crust thickness. Assuming a representative crust freezing temperature near the concrete liquidus of 1250 ºC (see Table 3-18) and a crust thermal conductivity of ~ 1.5 W/m-ºC,[26] then Eq. 3-2 predicts a crust thickness range of 3-7 mm over the range of heat fluxes shown in Table 3-20. As discussed earlier in this section, the thickness of the porous crusts formed at the melt water interface was in the range of 5-10 cm. These thicknesses are approximately an order of magnitude greater than the range predicted on the assumption of conduction-limited heat transfer. Thus, this simple analysis indicates that: i) water ingression contributed to the overall debris cooling rate realized in the experiments, and ii) the degree of interconnected porosity that forms the pathway for water ingression is increased by the presence of gas sparging during the quench process.

Aside from the water ingression mechanism, the tests also provided data on the nature and extent of the melt eruption cooling mechanism after cavity flooding. As shown in Table 3-7, significant eruptions were observed for Test CCI-2 that was conducted with LCS concrete. However, no spontaneous eruptions were observed after cavity flooding for the two tests conducted with siliceous concrete. The absence of eruptions for this concrete type is consistent with the results of the one-dimensional MACE Test M4 that was also conducted with siliceous concrete.[2] As discussed by Bonnet and Seiler,[27] the gas sparging rate during core-concrete interaction is the key parameter influencing the melt entrainment process during eruptions. Thus, the reduced gas content for this concrete type may have been a key contributor to the lack of eruptions for these two tests. Test occurrences may have also contributed to the lack of eruptions. In particular, in Test CCI-1 input power was terminated 10 minutes after cavity flooding (see Table 3-1), and this short operational period could have adversely affected the eruption process. For Test CCI-3, a partially anchored bridge crust formed during the test sequence that could have precluded eruptions from occurring (see Figure 3-63).

Aside from these findings, sufficient information was gathered during Test CCI-2 to evaluate the melt entrainment coefficient, which is the key parameter required for modeling of this process.[27] This analysis[4] indicates that the average entrainment coefficient, defined as the ratio of the melt volumetric entrainment rate to the hot gas volumetric flowrate, was ~ 0.11 % for CCI-2. This entrainment rate is consistent with that observed in previous MACE integral effect tests,[4] and is well within the range of that required to stabilize a core-concrete interaction over a fairly significant range of melt depths.[27-28]

In addition, the entrainment coefficient data for CCI-2 is significant since the eruptions occurred under a floating crust boundary condition (as evidenced by the posttest examinations that indicated the absence of a continuous void region below the crust upper surface), and while the input power was decreasing, so that the melt zone was not over-powered during the eruption process. Thus, data upon which the entrainment coefficient is based are deemed to be prototypic. On this basis, the entrainment coefficient may be used to evaluate the effects of the melt eruption cooling mechanism on mitigating the core-concrete interaction under plant accident conditions for the case of LCS concrete.

In terms of the crust breach cooling mechanism, both tests conducted with siliceous concrete provided data on *in-situ* crust strength, while Test CCI-1 also provided data on the extent of debris cooling after the crust was breached. Unfortunately, neither crust strength nor crust breach cooling data was obtained for the test conducted with LCS concrete, since the mantle crusts that formed in the upper region of the test section over the five hour period preceding water addition precluded the lance from contacting the crust material that formed when the cavity was flooded. The *in-situ* crust strength data obtained from the two tests conducted with siliceous concrete are provided in Table 3-21. As is evident from the table, the crusts were very weak, with failure strengths nearly two orders of magnitude below that expected for fully dense, monolithic crust material.[5] Thus, these measurements support the findings from the SSWICS test series, [5] which indicated that crust material formed during quench is structurally quite weak. However, the CCI strength measurements are significant because they were carried out under prototypic temperature boundary conditions before the material had cooled to room temperature. This can be contrasted with the SSWICS measurements that were carried out at room temperature after the specimens had been removed from the test section.[5]

Aside from the crust strength measurements, examination of Figure 3-73 indicates that the crust breach event for CCI-1 caused a significant transient increase in the debris cooling rate. In

particular, a large melt eruption occurred, resulting in a transient cooling event in which the peak heat flux exceeded 3 MW/m^2. After the breach, the heat flux from the debris upper surface steadily declined over the next five minutes to a plateau in the range of 250-300 kW/m^2, which is similar to the plateau observed prior to the breach event. In general, the data obtained from this procedure indicates that these breach events may lead to significant transient increases in the debris cooling rate under plant accident conditions.

In terms of the findings from the chemical analyses that relate to debris coolability, the compositions of the top crust regions (5-10 cm thick) formed in all tests were found to be elevated in concrete oxides relative to the core material immediately over the basemat. This finding is consistent with formation of these crusts late in the experimental sequence when the cavities were flooded. In addition, the analysis of the sample collected from the material that was erupted in test CCI-2 after cavity flooding was very close to the composition of samples collected from the top crust. This indicates that the concrete-rich oxide phase that fed the eruptions was present at the top of the melt under test conditions, as opposed to forming by gravity-driven stratification after the test was terminated.

Table 3-21. Results of *In-Situ* Crust Strength Measurements for CCI Tests.

Test	Concr. Type	Region Description	Wt % Concrete in Crust	Strength (MPa)	Uncertainty Range (MPa)
CCI-1	SIL (US)	Porous crust layer over solidified melt	22.3	1.2	0.5 – 3.7
CCI-3	SIL (EU)	Porous crust layer over solidified melt	51.2	0.2	0.1 – 0.9
		Partially anchored bridge crust over porous crust	47.8	0.3	0.2 – 0.6

4.0 APPLICATION OF RESULTS TO PLANT SCALE

In terms of the applicability to plant conditions, these tests have provided information that will contribute to the database for reducing modeling uncertainties related to two-dimensional molten core-concrete interaction under both wet and dry cavity conditions. Furthermore, the tests have provided additional confirmatory evidence and test data for coolability mechanisms identified in earlier integral effect tests. Data from this and other test series thus forms the technical basis for developing and validating models of the various cavity erosion and debris cooling mechanisms. These models can then be deployed in integral codes that are able to link the interrelated phenomenological effects, thereby forming the technical basis for extrapolating the results to plant conditions.

In terms of the dry cavity erosion process, the principal result of the test series relates to the lateral/axial heat flux ratio during core-concrete interaction. For the case of LCS concrete, the results indicate that this ratio is ~ 1. Conversely, this ratio was found to be ~ 4 for the case of siliceous concrete. This overall trend in the ablation front progression cannot be explained on the basis of our current understanding of these types of processes. Thus, extrapolation of the results to plant conditions is currently uncertain due to the lack of a phenomenological model that can rationalize the differences in the observed cavity erosion behavior.

In terms of debris coolability, there are several findings from the test series that are directly applicable to evaluating plant accident sequences. In terms of the water ingression mechanism, the test results indicate that the SSWICS heat transfer correlation[3] is extremely conservative insofar as calculation ingression-limited crust growth behavior. In particular, the correlation was found to under-predict the heat flux to overlying water by as much as an order of magnitude during time intervals when water ingression was occurring. Thus, coolability sequences calculated with this correlation would be highly conservative.

In terms of the melt eruption mechanism, significant eruptions were observed for the test conducted with LCS concrete, but no spontaneous eruptions were observed after cavity flooding for the two tests conducted with siliceous concrete. For the case of LCS, the melt entrainment coefficient was evaluated as ~ 0.11 % based on the test data. Moreover, these eruptions apparently occurred under a floating crust boundary condition, which is the expected condition at plant scale. Thus, the entrainment coefficient estimate can be used directly in existing models[27-28] for evaluating the effectiveness of melt eruptions on mitigating the accident sequence at plant scale for the case of LCS concrete. Conversely, the test results indicate the melt eruption cooling mechanism may be neglected for cases involving siliceous concrete. However, this assumption may be overly conservative because it is not clear whether test occurrences may have precluded eruptions from occurring for the two tests with this concrete type. In any case, the existing models[27-28] predict reduced cooling by the melt eruption process for the case of siliceous concrete simply due to the fact that these concretes contain less gas relative to LCS concrete. In this regard, the lack of eruptions is consistent with the models[27] that predict reduced melt eruptions as the gas content of the concrete is reduced.

Finally, the crust breach data from the tests indicate that the crusts that form at the melt/water interface after cavity flooding are extremely weak, and will not be mechanically stable at plant scale. Rather, the crust is expected to fail and, thereby, maintain a floating crust boundary condition that will allow the melt eruption and water ingression cooling mechanisms to proceed. Moreover, this finding simplifies the analysis of debris coolability since it removes the complicated requirement of modeling this process under an anchored crust boundary condition.[28]

Finally, the tests carried out as part of this program have examined core-concrete interaction and debris coolability for the case of fully oxidized core melts. In real plant accident sequences, a significant melt metal fraction may be present that may result in a stratified pool configuration. This type of pool structure was not evaluated in the program. Thus, additional analysis and testing may be required with melts containing a significant metal fraction to further reduce phenomenological uncertainties related to core-concrete interaction and debris coolability.

4.0 SUMMARY AND CONCLUSIONS

The purpose of the OECD/MCCI Program was to carry out reactor materials experiments and associated analysis to achieve the following two technical objectives: 1) resolve the ex-vessel debris coolability issue by providing both confirmatory evidence and test data for coolability mechanisms identified in previous integral effect tests, and 2) address remaining uncertainties related to long-term 2-D core-concrete interaction under both wet and dry cavity conditions. This report has summarized the results of three large scale Core-Concrete Interaction (CCI) experiments that were conducted to address the second program objective. The overall purpose of these tests was to provide information in several areas, including: i) lateral vs. axial power split during dry core-concrete interaction, ii) integral debris coolability data following late phase flooding, and iii) data regarding the nature and extent of the cooling transient following breach of the crust formed at the melt-water interface.

The experimental approach was to investigate the interaction of fully oxidized PWR core melts with specially-designed two-dimensional concrete test sections. The initial phase of the tests was conducted under dry cavity conditions. After a predetermined ablation depth was reached, the cavities were flooded with water to obtain data on the coolability of core melts after core-concrete interaction had progressed for some time. Two tests were conducted with siliceous concrete (CCI-1 and CCI-3), and a third test with Limestone/Common Sand (LCS) concrete (CCI-2). Test CCI-1 was conducted with a U.S.-specific siliceous concrete that had very low gas content, while CCI-3 was conducted with a European-specific siliceous concrete with gas content intermediate to that used in CCI-1 and CCI-2. The input power for the tests was selected so that the initial heat flux to the concrete surfaces and overlying structure was in the range of that expected during the early stages of an ex-vessel plant accident; i.e., 150-200 kW/m^2. On this basis, total input power for CCI-1 was selected to yield a heat flux at the upper end of this range (viz., 150 kW), while the other two tests were conducted with an input power that yielded a flux at the lower end of the range (viz., 120 kW). Principal findings from these tests related to two-dimensional cavity erosion behavior are summarized as follows:

1. All tests showed the overall trend of decreasing melt temperature as ablation progressed, which was due to a heat sink effect as relatively cool concrete slag was introduced into the melt, as well as the increasing heat transfer surface area as the melts expanded into the concrete crucibles. The reduction in melt temperature may have further reflected the evolution of the pool boundary freezing temperature that decreased as additional concrete was eroded into the melt over the course of the tests.

2. Tests CCI-1 and CCI-2 showed evidence of initial crust formation on the concrete basemat and sidewalls that resulted in an incubation period in which the ablation rates were very low and the melt temperature was relatively stable. Test CCI-3 also showed evidence of initial crust formation on the concrete basemat, but there was no evidence of initial sidewall crust formation for this test. In all cases, the surface crusts eventually failed, thereby allowing ablation to proceed. The duration of the incubation period for CCI-1 and CCI-2 appeared to be inversely proportional to concrete gas content, which suggests that crust failure may be driven in part by the mechanical forces that arise from the production of concrete decomposition gases at the core-concrete interface.

3. Long-term ablation behavior was found to be closely linked to concrete type. Lateral and axial ablation rates for the LCS concrete test were virtually indistinguishable; the concrete erosion rate averaged 4 cm/hr over several hours of interaction before gradually decreasing. The corresponding surface heat flux was ~ 60 kW/m^2. Thus, the lateral/axial heat flux ratio for this concrete type was ~ 1.

4. The relatively uniform power split for CCI-2 can be contrasted with the results of the two tests conducted with siliceous concrete. For test CCI-1, the ablation was highly non-uniform, with most of the ablation concentrated in the North sidewall of the test apparatus. Crust stability may have played a major role in determining the ablation progression for this experiment; i.e., the data suggests that after the crust failed on the North concrete sidewall, the input power was predominately dissipated through ablation of this sidewall, while crusts continued to protect the basemat and south sidewall surfaces during the balance of the interaction.

5. In contrast to Test CCI-1, Test CCI-3 exhibited fairly symmetrical behavior insofar as the progression of lateral ablation is concerned. However, unlike Test CCI-2, the lateral ablation was highly pronounced in comparison to axial ablation. In this regard, the results of tests CCI-1 and CCI-3 are consistent. Lateral ablation in CCI-3 averaged 10 cm/hr over the last hour of the experiment, while the axial ablation rate was limited to 2.5 cm/hr over the same time interval. The corresponding heat fluxes in the lateral and axial directions were 97 and 25 kW/m^2, respectively. On this basis, the lateral/axial surface heat flux ratio for test CCI-3 was estimated as ~ 4, which is significantly higher than the near-unity ratio deduced for test CCI-2 with LCS concrete.

6. Between the two concrete types, possible explanations for differences in the erosion behavior are chemical composition and concrete gas content. A third possible explanation was revealed during posttest examinations. In particular, the core-concrete interface for the siliceous concrete tests consisted of a region where the core oxide had locally displaced the cement that bonded the aggregate. Conversely, the ablation front for the LCS test consisted of a powdery interface in which the core and concrete oxides were clearly separated. Variations in the interface characteristics may have influenced the ablation behavior for the two concrete types.

7. In terms of the chemical analysis results obtained as part of the test series, the corium in the central region of the test section was found to have a higher concentration of core oxides in comparison to that adjacent to the two ablating concrete sidewalls for all tests. Conversely, core oxides were found to be slightly concentrated near the concrete basemat in comparison to that found in the bulk of the corium. For both siliceous concrete tests, two zones appeared to be present: a heavy monolithic oxide phase immediately over the basemat that was enriched in core oxides, with a second overlying porous, light oxide phase that was enriched in concrete oxides. The overlying oxide phase was porous and appeared to have been quenched after the cavity was flooded. This well-defined phase distribution can be contrasted with the debris morphology for CCI-2. In this test, the debris was highly porous and fragmented over the entire axial extent of the material

remaining over the basemat. This open structure is consistent with the high degree of debris cooling that occurred after cavity flooding.

The second and equally important aspect of the test series was to investigate debris coolability under late-phase flooding conditions. In terms of phenomenology, the tests provided data on the bulk cooling, water ingression, melt eruption, and transient crust breach cooling mechanisms. In addition, Test CCI-2 provided data on the water ingress process at the interface between the core material and concrete sidewalls. This mechanism had been previously identified in the COTELS reactor material test series.[11] Principal findings from the tests related to debris coolability are summarized as follows:

1. The heat flux during the first 5 minutes following cavity flooding was high for all tests. For the two tests conducted with siliceous concrete, the initial heat fluxes were close to the Critical Heat Flux (CHF) limitation of ~ 1 MW/m^2 under saturated boiling conditions. Thus, the heat fluxes were indicative of quenching of the upper surface crust that was present as an initial condition for both tests. However, for test CCI-2, the upper surface was essentially devoid of a surface crust at the time of cavity flooding. Thus, water was able to directly contact the melt, resulting in a bulk cooling transient in which the initial cooling rate approached 3 MW/m^2. The heat flux eventually fell below 1 MW/m^2 after ~ 5 minutes. At this time, a stable crust most likely formed at the melt-water interface, thereby terminating the bulk cooling transient.

2. The tests did not generally exhibit a pronounced decrease in overall melt temperature after cavity flooding. This is despite the fact that the heat flux and power supply responses both indicated substantial debris cooling. This type of behavior can be rationalized by a latent heat transfer process in which a quench front develops at the melt/water interface, as opposed to a sensible heat transfer process in which the entire melt mass is cooled by convective heat transfer with the heat dissipated to the overlying water by conduction across a thin crust at the melt/water interface. The posttest debris morphologies were also consistent with development of quenched debris zones, as opposed to bulk cooldown of the entire melt mass by conduction-limited cooling across a thin crust at the melt/water interface.

3. After the initial transient, the debris/water heat fluxes ranged from 250 to 650 kW/m^2. Heat fluxes for both siliceous concrete tests were lower than the test conducted with LCS concrete. In general, the data indicates that the heat flux increases with concrete gas content. The heat fluxes realized in the tests were up to an order of magnitude higher than that predicted by the SSWICS water ingression correlation. Thus, the data suggests that the degree of interconnected cracks/fissures/porosity that form the pathway for water to ingress into solidifying core material is increased by the presence of gas sparging, particularly for the case in which the melt contains a high concrete fraction.

4. Aside from the water ingression mechanism, the tests also provided data on the melt eruption cooling mechanism. Significant eruptions were observed for Test CCI-2. However, no spontaneous eruptions were observed after cavity flooding for the two tests

conducted with siliceous concrete. The reduced gas content for this concrete type may have contributed to the lack of eruptions for these two tests. Test occurrences may have also played a role in the lack of eruptions (i.e., input power for Test CCI-1 was terminated 10 minutes after cavity flooding, and for Test CCI-3, a partially anchored bridge crust formed during the test sequence that could have adversely affected the eruption process). The melt entrainment coefficient for CCI-2 was ~ 0.11 %, which is in the range of that required to stabilize a core-concrete interaction over a fairly significant range of melt depths.

5. In terms of the crust breach cooling mechanism, both siliceous concrete tests provided data on *in-situ* crust strength, while Test CCI-1 also provided data on the extent of cooling after crust breach. The crust strength data indicates that crust material formed during quench is very weak. This finding is consistent with the SSWICS test series crust strength measurements. However, the CCI strength measurements are significant because they were carried out under prototypic temperature boundary conditions before the material had cooled to room temperature.

6. Aside from the crust strength measurements, the crust breach event in CCI-1 caused a significant transient increase in the debris cooling rate. In particular, a large melt eruption occurred, resulting in a transient cooling event in which the peak heat flux exceeded 3 MW/m^2. After the breach, the heat flux from the debris upper surface steadily declined over the next five minutes to a plateau in the range of 250-300 kW/m^2, which is similar to the plateau observed prior to the breach event. In general, the data obtained from this procedure indicates that breach events may lead to significant transient increases in the debris cooling at plant scale.

In terms of the applicability to plant conditions, these tests have provided information that will contribute to the database for reducing modeling uncertainties related to two-dimensional molten core-concrete interaction under both wet and dry cavity conditions. Furthermore, the tests have provided additional confirmatory evidence and test data for coolability mechanisms identified in earlier integral effect tests. Data from this and other test series thus forms the technical basis for developing and validating models of the various cavity erosion and debris cooling mechanisms. These models can then be deployed in integral codes that are able to link the interrelated phenomenological effects, thereby forming the technical basis for extrapolating the results to plant conditions.

Note that the tests carried out as part of this particular program have examined core-concrete interaction and debris coolability for the case of fully oxidized core melts. As a whole, the results of the two-dimensional CCI tests have indicated trends in the ablation front progression that cannot be explained on the basis of our current understanding of the phenomenology involved with this type of physical process. These trends need to be understood before the results can be extrapolated to plant scale. Furthermore, in real plant accident sequences, a significant melt metal fraction may be present that may result in a stratified pool configuration. This type of pool structure was not evaluated in the program. Thus, additional analysis and testing may be required with melts containing a significant metal fraction to further reduce phenomenological uncertainties related to core-concrete interaction, and to evaluate the effects of melt metal content on debris coolability.

6.0 REFERENCES

1. M. T. Farmer, B. W. Spencer, D. J. Kilsdonk, and R. W. Aeschlimann, "Results of MACE Corium Coolability Experiments M0 and M1b," Proc. 8th Int. Conf. on Nucl. Eng., ICONE-8175, April 2-6, 2000.

2. M. T. Farmer, B. W. Spencer, J. L. Binder, and D. J. Hill, "Status and Future Direction of the Melt Attack and Coolability Experiments (MACE) Program at Argonne National Laboratory," Proc. 9th Int. Conf. on Nucl. Eng., ICONE-9697, April 8-12, 2001.

3. S. Lomperski, M. T. Farmer, D.J. Kilsdonk, and R. W. Aeschlimann, "Small-Scale Water Ingression and Crust Strength Tests (SSWICS) SSWICS Final Report: Thermal Hydraulic Results," OECD/MCCI-2005-TR03, June 2005.

4. M. T. Farmer, S. Lomperski, D. J. Kilsdonk, and R. W. Aeschlimann, "OECD MCCI Project Final Report," OECD/MCCI-2005-TR06, January 2, 2006

5. S. Lomperski, M. T. Farmer, D. J. Kilsdonk, and R. W. Aeschlimann, "Project Small-Scale Water Ingression and Crust Strength Tests (SSWICS) SSWICS Final Report: Crust Strength Measurements," OECD/MCCI-2005-TR02, June 2005.

6. J. J. Foit, "Modeling of Oxidic Molten Core-Concrete Interaction in WECHSL," Nucl. Eng. and Design, Vol. 170, p. 73-79, 1999.

7. E. R. Copus et al, "Core-Concrete Interactions Using Molten UO_2 with Zirconium on a Basaltic Basemat : the SURC-2 Experiment," NUREG/CR-5564, 1990.

8. D. H. Thompson, et al., "Thermal-hydraulic Aspects of the Large-Scale Integral MCCI Tests in the ACE program," Proc. 2nd OECD (NEA) CSNI Specialist Meeting on Molten Core Debris-Concrete Interaction, Karlsruhe, Germany, April 1992.

9. D. H. Thompson, M. T. Farmer, J. K. Fink, D. R. Armstrong, and B. W. Spencer, "ACE Phase C Final Report: Volume I – MCCI Thermalhydraulic Results," ACE-TR-C42 Volume I, September, 1997.

10. J. K. Fink et al., "Aerosol and Melt Chemistry in the ACE Molten Core-Concrete Interaction Experiments," High Temperature and Materials Science, Vol. 33, p. 51-75, 1995.

11. H. Nagasaka, "COTELS Project (3): Ex-Vessel Debris Cooling Tests," Proc. OECD Workshop on Ex-Vessel Debris Coolability, Karlsruhe, Germany, November 15-18, 1999.

12. H. Alsmeyer, "BETA Experiments on Zirconium Oxidation and Aerosol Release During Molten Corium/Concrete Interaction," Proc. 2nd OECD (NEA) CSNI Specialist Meeting on Molten Core Debris-Concrete Interaction, Karlsruhe, Germany, April, 1992.

13. M. T. Farmer, S. Lomperski, D. J. Kilsdonk, and R. W. Aeschlimann, "Long-Term 2-D Molten Core Concrete Interaction Test Design Report," Rev. 0, OECD/MCCI-2002-TR05, September 30, 2002

14. M. T. Farmer, S. Lomperski, D. J. Kilsdonk, and R. W. Aeschlimann, "2-D Core Concrete Interaction (CCI) Tests: CCI-1 Test Data Report-Thermalhydraulic Results," OECD/MCCI-2004-01, January 31, 2004.

15. M. T. Farmer, S. Lomperski, D. J. Kilsdonk, and R. W. Aeschlimann, "2-D Core Concrete Interaction (CCI) Tests: CCI-2 Test Data Report-Thermalhydraulic Results," OECD/MCCI-2004-05, October 15, 2005.

16. M. T. Farmer, S. Lomperski, D. J. Kilsdonk, R. W. Aeschlimann, "2-D Core Concrete Interaction (CCI) Tests: CCI-3 Test Data Report-Thermalhydraulic Results," Rev. 0, OECD/MCCI-2005-TR04, October 15, 2005.

17. M. T. Farmer, S. Lomperski, and S. Basu, "Results of Reactor Materials Experiments Investigating 2-D Core-Concrete Interaction and Debris Coolability," Proc. ICAPP '04, Pittsburgh, PA, June 13-17, 2004.

18. M. T. Farmer, S. Lomperski, and S. Basu, "The Results of the CCI-2 Reactor Material Experiment Investigating 2-D Core-Concrete Interaction and Debris Coolability," 11th International Topical Meeting on Nuclear Reactor Thermal-Hydraulics (NURETH-11), Avignon, France, October 2-6, 2005.

19. M. T. Farmer, S. Lomperski, and S. Basu, "Status of the Melt Coolability and Concrete Interaction (MCCI) Program at Argonne National Laboratory," Proc. ICAPP '05, Seoul, Korea, May 15-19, 2005.

20. M. T. Farmer, S. Lomperski, and S. Basu, "The Results of the CCI-3 Reactor Material Experiment Investigating 2-D Core-Concrete Interaction and Debris Coolability," Proc. ICAPP '06, Reno, Nevada, June 6-8, 2006.

21. B. W. Spencer, et al., "MACE Scoping Test Data Report," EPRI Report ACE-TR-D03, June, 1991.

22. D. G. Graczyk, "Chemical Analysis of Concrete Samples, CCI-1, CCI-2, and CCI-3," Intra-Laboratory memo to M. T. Farmer, Argonne National Laboratory, October 14, 2005.

23. M. F. Roche, et al., "Solidus and Liquidus Temperatures of Core-Concrete Mixtures," U.S. Nuclear Regulatory Commission Report NUREG/CR-6032, 1993.

24. J. J. Sienicki and B. W. Spencer, "The Jet Impingement Stage of Molten Core-Concrete Interactions," OECD CSNI Specialist Meeting on Core Debris/Concrete Interactions, Electric Power Research Institute, Palo Alto, CA, September 3-5, 1986.

25. R. J. Roark and W. C. Young, Formulas for Stress and Strain, 5th Ed., McGraw-Hill Book Company, New York, NY, 1975.

26. M. T. Farmer, D. J. Kilsdonk, R. W. Aeschlimann, and B. W. Spencer, "Results of MACE Test M1b Posttest Debris Property Measurements," EPRI/ACEX-TR-C23, February, 1998.

27. M. Bonnet and J. M. Seiler, "Coolability of Corium Spread onto Concrete Under Water, the PERCOLA Model," Proc. 2nd OECD (NEA) CSNI Specialist Meeting on Molten Core Debris-Concrete Interaction, Karlsruhe, Germany, April, 1992..

28. M. T. Farmer, "Modeling of Ex-Vessel Corium Coolability with the CORQUENCH Code," Proc. 9th Int. Conf. on Nucl. Eng., ICONE-9696, April 8-12, 2001.